

MSc Thesis

Masilo Ramafemo

Lead and Yttrium co-doped Bismuth Oxide Electrolytes for Low Temperature Solid Oxide Fuel Cells

Supervisor: Prof Caren Billing
Co-supervisor: Prof Dave Billing
Submitted on: 07 December 2021

Abstract

A co-dopant bismuth oxide system with Pb^{2+} and Y^{3+} was developed. When Pb^{2+} was doped as a single dopant, a mixture of cubic and tetragonal phases was obtained, indicating that Pb^{2+} on its own does not stabilise $\delta\text{-Bi}_2\text{O}_3$. On the other hand, using 5 mol% Pb^{2+} and 10 mol% Y^{3+} double dopants (5Pb10YSB, where SB represents stabilized Bi_2O_3), we were able to stabilize a high temperature cubic phase with a total dopant concentration as low as 15 mol%. Its total conductivity at 500°C was 0.1185 S cm^{-1} , comparable to 0.0984 S cm^{-1} obtained from the double doped system with 8 mol% Dy^{3+} and 4 mol% W^{6+} stabilizing $\delta\text{-Bi}_2\text{O}_3$ (8D4WSB) and 100 times more conductive than 10 mol% Y^{3+} stabilized zirconia (10YSZ) at the same temperature.

Arrhenius plots of the total conductivity for the 1.5Pb25YSB (1.5 mol% Pb^{2+} and 25 mol% Y^{3+} doped Bi_2O_3) and 5Pb10YSB systems exhibited discontinuities between 500-550°C characteristic of phase changes. Differential thermal analysis, variable temperature Raman spectroscopy and variable temperature powder X-ray diffraction revealed that these discontinuities in conductivity occurs in the same temperature range as the phase transitions (cubic to tetragonal phase) observed in these materials. On the other hand, the high total dopant concentration, 1.5Pb25YSB (i.e. 26.5 mol%) showed a single phase from ambient temperature to higher temperatures (800°C), suggesting phase stability of material but displayed lower conductivities compared to 5Pb10YSB. This decrease in conductivity could be explained by an increase in dopant concentration resulting with stronger association of O^{2-} with the dopant ions (stronger bonds) reducing mobility.

Acknowledgement

First and foremost, I would like to express my sincere gratitude to my supervisor, Professor Caren Billing, for her outstanding help, exceptional support, invaluable discussions and guidance during the course of my studies. I would also like to thank Professor Dave Billing for his experimental support and guidance. Recognition must also go to my friends and colleagues in material science for their help and friendship, and to my family for their utmost support and encouragement. Finally, I would like to thank National Research Foundation and the University of Witwatersrand for funding my MSc project.

Declaration

I declare that this dissertation is my own, unaided work. It is being submitted for the Degree of Master of Science at the University of the Witwatersrand, Johannesburg. It has not been submitted before for any degree or examination at any other University.



(Signature of candidate)

___7th___ day of ___December___ 2021 ___at___ 12:00 pm ___

Table of contents

1.1. Fuel Cells	1
1.2. Types of Fuel Cells	3
1.3. Electrolytes for Intermediate Temperature-SOFCs	4
1.3.1. Phases and conductivity of pure Bi ₂ O ₃	6
1.3.2. Structure of pure δ -Bi ₂ O ₃	9
1.3.4. Doping with lead and yttrium	19
1.4. Aims and Objectives	21
1.5. References	23
2.1. Synthesis of co-doped Bi₂O₃	28
2.2. Materials characterization	31
2.2.1. Powder X-ray Diffraction (PXRD).....	31
2.2.2. Differential Thermal Analysis/Thermal Gravimetry Analysis (DTA/TGA).....	33
2.2.3. Raman Spectroscopy (RS)	34
2.2.4. Rapid acquisition pair distribution function (RA-PDF) technique	34
2.2.5. Electrochemical Impedance Spectroscopy (EIS)	36
2.3. X-ray diffraction technique	37
2.3.1. Introduction to diffraction	37
2.3.2. Powder X-ray diffraction (PXRD)	44
2.3.2.1. Laboratory X-ray sources	46
2.3.2.2. Filters.....	50
2.3.2.3. Monochromator.....	50
2.3.3. Synchrotron X-ray powder diffraction	51
2.3.3.1. Synchrotron X-ray sources	51
2.3.3.2. Filters.....	55
2.3.3.3. Monochromators	55
2.3.4. The Rietveld method.....	56
2.4. Thermal Analysis	57

2.5.	Raman Spectroscopy	60
2.6.	Pair distribution function and total scattering	62
2.6.1.	Termination Errors	66
2.6.1.1.	Q_{\max}	66
2.6.1.2.	Q_{\min}	67
2.6.2.	Modelling of PDF	68
2.7.	Electrochemical Impedance Spectroscopy (EIS)	69
2.7.1.	Equivalent Circuit Modelling (ECM).....	74
2.7.1.1.	Resistors	75
2.7.1.2.	Capacitors.....	76
2.7.1.3.	Series R-C circuit.....	77
2.7.1.4.	Parallel R-C circuit.....	77
2.7.1.5.	Constant Phase Element (CPE)	80
2.7.1.6.	Warburg Element	82
2.7.1.7.	Circuit Obscurity and Fitting Algorithms.....	84
2.8.	References	85
3.1.	X-ray diffraction analysis	89
3.1.1.	Higher total dopant concentration	90
3.1.2.	Lower total dopant concentration.....	98
3.2.	Variable temperature-PXRD studies	103
3.3.	DTA/TG analysis	112
3.4.	Raman Spectroscopy analysis	116
3.5.	Analysing PDFs	118
3.5.1.	Peak fitting	118
3.1.1.	PDFgui	120
3.2.	References	125
4.1.	Variable Temperature EIS.....	127
4.2.	Analysis of impedance spectra measured in low temperature range	127
4.3.	Analysis of impedance spectra measured in IT- and HT- range.....	131
4.4.	Ionic conductivities and activation energies.....	137
4.5.	References	147

List of Figures

Fig. 1.1 The flow of electrons and oxygen anions through the outer circuit of a functional SOFC system. ³	3
Fig. 1.2 Conductivity as log σ versus temperature for Bi_2O_3 . ²⁶	8
Fig. 1.3 Decrease in relative conductivity of $\delta\text{-Bi}_2\text{O}_3$ doped with different dopants (25 mol% dopant composition). Different dopants have different decay rate. σt refers to conductivity at time t while σ_0 is the initial conductivity. ³³	10
Fig. 1.4 The ionic radii and polarizabilities of lanthanide dopants typically added to $\delta\text{-Bi}_2\text{O}_3$ are considerably less than those of Bi^{3+} . ⁴⁵	12
Fig. 1.5 Sillen model ⁵⁰ , where the light blue spheres represent O_2 and the red spheres represent Bi^{3+} ion.....	13
Fig. 1.6 The Gattow and Schröder model ⁵² , where the blue spheres represent O_2 and the red spheres represent Bi^{3+} ion.	13
Fig. 1.7 Segment of $\delta\text{-Bi}_2\text{O}_3$ ⁵⁴ unit cell displaying oxygen positions.....	14
Fig. 1.8 $\delta\text{-Bi}_2\text{O}_3$ formation spectrum of the fcc and rhombohedral phases in the ionic radius of Ln^{3+} versus composition diagram. ⁵⁸	15
Fig. 1.9 x_{\min} , the minimum value of x needed to stabilize the δ -phase in $(\text{Bi}_2\text{O}_3)_{1-x}(\text{Ln}_2\text{O}_3)_x$ in relation to the ionic radius (R_{ion}) of the Ln^{3+} . ⁵⁹	17
Fig. 1.10 Log σ , where σ represents the ionic conductivity of $(\text{Bi}_2\text{O}_3)_{1-x}(\text{Ln}_2\text{O}_3)_x$ and x is in the range of x_{\min} as shown in Fig. 1.9 (in relation to the ionic radius of the substituted Ln^{3+}). ⁵⁹	17
Fig. 1.11 Schematic representation of $(\text{Bi}_2\text{O}_3)_{0.75}(\text{Ln}_2\text{O}_3)_{0.25}$ ordered unit model, with a unit cell dimension of, $a = 5.529\text{\AA}$. ⁶⁷	18
Fig. 2.1 Schematic representation of synthetic route for lead yttrium stabilized bismuth oxide (PbYSB) in a powder form obtained by calcining at 450°C , followed by annealing at 700°C in a furnace.....	29

Fig. 2.2 Schematic representation of transmission geometry used on most typical RA-PDF beamlines. ¹⁰	35
Fig. 2.3 crystal lattice (left) and unit cell (right) in three-dimensional space. ¹²	37
Fig. 2.4 X-ray tube depicting the production X-ray spectra. ¹³	39
Fig. 2.5 The continuous X-ray spectrum emitted from tungsten target for four different values of <i>eV</i> , the incident electron energy. ¹³	40
Fig. 2.6 An electron shell showing the production of $K\alpha$ and $K\beta$ when an electron is dislodged. ¹³	41
Fig. 2.7 Constructive (a) and destructive (b) interferences of X-ray monochromatic beam. ¹³	41
Fig. 2.8 Diffraction phenomena used to derive Bragg's law. ¹⁷	42
Fig. 2.9 Single-crystal diffraction pattern of an enzyme. The white rod protruding from the top is the beamstop (a). Powder X-ray diffraction spectrum of silicon (b). ¹⁶	44
Fig. 2.10 Schematic representation of x-ray powder diffractometer. ¹⁶	45
Fig. 2.11 Diffractogram of X-ray intensity plotted against the angle 2θ . ¹⁶	45
Fig. 2.12 A schematic diagram of a sealed X-ray laboratory tube with indicated main components (a) and a tube photograph (b). ¹⁸	46
Fig. 2.13 X-ray spectrum generated from a Cu anode by different accelerating voltages. Until the voltage level reaches a critical value (about 8.5 kV for Cu), no radiation features are produced. The average operating voltage is approximately 4 times the critical voltage: higher voltage levels simply contribute to an increase in the "white" high-energy X-ray radiation intensity with a relatively small increase in the characteristic line intensity. ¹⁸	47
Fig. 2.14 Diagram of energy level for a neutral Cu atom. The features of the peaks shown in Fig. 2.6 emerge from the shown electronic transitions. ²⁰	48
Fig. 2.15 Schematic of a synchrotron storage ring. Machines of the third generation have several straight segments and are optimized as X-ray sources by employing undulator and wiggler insertion systems. ²⁶	52
Fig. 2.16 Representations of (a) a bending magnet emitting a tangential radiation fan, (b) a fan of wiggler-emitted radiation and (c) an undulator emitted collimated beam. ²⁷	54
Fig. 2.17 Schematic representation of synchrotron radiation (a) and laboratory sources (b). ²⁷ ...	54

Fig. 2.18 Representation of a double-bounce monochromator used in synchrotrons. From the polychromatic source, the first crystal chooses a wavelength, which the second crystal reflects in the initial direction. For efficient transmission of the beam, the lattice planes of the latter have to be precisely aligned with the first crystal. ²⁷	55
Fig. 2.19 Measurement principles of DTA. ³⁶	59
Fig. 2.20 Ni X-ray PDF gathered in a capillary generated using varying Q_{\max} values. ⁵⁶	66
Fig. 2.21 Comparison of X-ray PDF patterns for BaTiO ₃ using various Q_{\max} values. ⁵⁶	67
Fig. 2.22 Calculated G(r) values of liquid Te using various integration limits. ⁵⁸	68
Fig. 2.23 Sinusoidal excitation signal (applied) and linear response signal (measured). ⁶¹	71
Fig. 2.24 A diagram during EIS experiments, the observed pseudo linear spectrum was depicted by a polarization curve. The origin of Lissajous diagrams is also visible in the observed field. ⁶¹	72
Fig. 2.25 Impedance vector Nyquist plot. ⁶¹	73
Fig. 2.26 With a single time constant, a simple equivalent circuit is created. ⁶¹	74
Fig. 2.27 (a) Representation of a perfect resistor in a circuit diagram, (b) Nyquist plot for a resistor ⁶²	75
Fig. 2.28 (a) An ideal capacitor representation, (b) Nyquist plot for a capacitor ⁶⁵	76
Fig. 2.29 (a) R-C circuit connected in series, (b) Nyquist plot for an ideal polarizable electrode. ⁶⁴	77
Fig. 2.30 (a) Representation of an R-C circuit connected in parallel, (b) Nyquist plot of a polarizable electrode in real life. ⁶⁶	78
Fig. 2.31 Bode plot for a parallel RC circuit. ⁶⁷	79
Fig. 2.32 (a) Parallel R-C circuit with a series ohmic resistance, (b) the corresponding Nyquist plot for a real-world polarizable electrode. ⁶⁷	80
Fig. 2.33 Nyquist plot for a CPE element, on its own (a), and in the form of a depressed semi-circle (b). ⁶⁵	81
Fig. 2.34 (a) Warburg element representation, (b) representative Nyquist plot for a Warburg element showing mass diffusion behaviour. ⁶⁵	82
Fig. 2.35 Nyquist plot for finite Warburg elements. ⁶⁵	83

Fig. 3.1 XRD pattern of 25PbSB showing a mixture of phases annealed at 700°C. Inset shows a magnified region at the range of 2θ angle from 30 to 60 degrees.	91
Fig. 3.2 Laboratory XRD patterns for 1.5Pb25YSB, 6Pb25YSB, 9Pb25YSB and 15Pb25YSB and a magnified inset showing data between 30° to 40° (2θ) (a); Synchrotron diffractograms for 1.5Pb25YSB, 3.75Pb25YSB and 15Pb25YSB (b). All samples were annealed at 700°C for 12 hours.....	92
Fig. 3.3 X-ray diffraction patterns for 3.75Pb25YSB and 7.5Pb25YSB annealed at 800°C for 20 hours. Blue circles and (+) on the magnified inset between 30° to 40° (2θ) indicate shoulders on the side of peaks and some of the additional peaks that were observed, respectively.....	93
Fig. 3.4 The structure of 1.5Pb25YSB viewed along [100], where the red spheres represent O and the violet spheres represent Bi/Pb/Y. With oxygen atoms located at 8c (¼, ¼, ¼) and 32f (x, x, x) interstitial sites.....	94
Fig. 3.5 Observed and calculated laboratory (a) and synchrotron(b) diffraction patterns for 1.5Pb25YSB composition. The blue circles in the figure indicate the experimental data while the red solid line is the Rietveld fit. The orange lines represent the positions of the predicted peaks. The lower plot (represented by a black line) is the difference curve between the observed and calculated diffraction profiles. The fitted background has been subtracted from both the observed and calculated intensities for clarity.	95
Fig. 3.6 Compositional modification of the (BiO _{1.5}) _{0.75-x} (PbO) _x (YO _{1.5}) _{0.25} cubic unit cell parameter at room temperature with Y ³⁺ composition (25 mol%) kept constant.	97
Fig. 3.7 The XRD patterns of samples of lower total dopant concentration, displaying a mixture of phases.....	98
Fig. 3.8 Laboratory XRD diffractograms for 3Pb9YSB, 5Pb10YSB and 5Pb15YSB (a), synchrotron diffractograms for 5Pb10YSB and 5Pb15YSB (b), we could not measure the synchrotron data for 3Pb9YSB. All samples were annealed at 750°C for 16 hours.	100
Fig. 3.9 Diffractograms showing (a) laboratory XRD patterns annealed (at 750 °C) for 3Pb9YSB, 5Pb10YSB and 5Pb15YSB material and (b) synchrotron XRD data all measured at 25 °C.	101
Fig. 3.10 Rietveld refinement plots for 5Pb10YSB at room temperature for laboratory (a) and synchrotron XRD (b) diffraction profiles. The observed (blue dots) and calculated (red solid line) data is given as well as the difference plots. The orange symbol shows the positions of the allowed Bragg reflections in space group <i>Fm3m</i>	103
Fig. 3.11 Stacked diffraction patterns for VT-PXRD measurements of 1.5Pb25YSB during the heating cycle, with the top perspective focusing on the higher angle data.	104

Fig. 3.12 Zoomed-in, <i>In situ</i> diffractograms collected for 1.5Pb25YSB material annealed at 750 °C over the temperature range of 30-780 °C.	104
Fig. 3.13 Stacked diffraction patterns for VT-SCXRD diffractograms collected for the 5Pb10YSB material during the heating cycle in the temperature range of 25-683°C.....	105
Fig. 3.14 Zoomed-in stacked diffractograms collected for annealed (at 750 °C) 5Pb10YSB material over the temperature range of 25-683 °C. The top perspective, again focusing on the higher angle data, clearly shows that there is some phase transformation occurring.	106
Fig. 3.15 Rietveld refinements of the diffraction patterns for 5Pb10YSB where the dots represent observed data, the red line shows the fit and black line is the difference curve. This was done by including (a) the δ -phase only at 468°C, (b) the mixture of δ - and β -phase at 468°C and (c) the single δ -phase at 683°C. (d) An enlarged view depicting how the shoulders transform to become the main peaks.....	107
Fig. 3.16 Stacked diffraction patterns for VT-SCXRD measurements of 5Pb10YSB showing anisotropic peak broadening from about 468 °C during the cooling cycle. Indexing only applies to the pure δ -phase above 548 °C.	108
Fig. 3.17 Zoomed-in, <i>In situ</i> diffractograms collected for an annealed (at 750 °C) 5Pb10YSB material over the temperature range of 683-25 °C.....	109
Fig. 3.18 Thermal variation of the cubic lattice parameter, a , from Rietveld analysis of (a) SCXRD for 5Pb10YSB and (b) laboratory XRD data for 1.5Pb25YSB on heating (blue line) and cooling (orange line).	110
Fig. 3.19 DTA scans for an empty crucible and 1.5Pb25YSB material (annealed at 750°C) over the temperature 30-800°C.....	113
Fig. 3.20 DTA (a) and TGA (b) plots for 1.5Pb25YSB. Blue and orange solid lines show heating and cooling runs, respectively.....	114
Fig. 3.21 Results for 5Pb10YSB showing the DTA thermogram (with enlarged detail of the profiles in the inset) (a) and TGA curves (b). Blue and orange solid lines show heating and cooling runs, respectively. The two arrows represent the two endothermic events, one at ~480 °C and ~60°C.....	115
Fig. 3.22 Stacked Raman spectra of the 1.5Pb25YSB sample taken during the heating cycle..	117
Fig. 3.23 VT-Raman spectra of 5Pb10YSB. The inset (related to cooling back to room temperature) shows an enlarged view depicting how the band at 305 cm ⁻¹ disappears at 600°C and reappears at room temperature.	118

Fig. 3.24 (a) PDF construction of spherical shells of thickness dr at a distance r away from the origin. (b) A face centred cubic (fcc) structure, used in this example, contains 12 nearest neighbours and 6 next-nearest neighbours (not visible due to the viewing angle). ²²	119
Fig. 3.25 The PDF, $G(r)$ vs r , of 5Pb10YSB (a) and 1.5Pb25YSB (b) data.	120
Fig. 3.26 PDFgui phase configuration screen.....	121
Fig. 3. 27 A calculated fit for the experimental PDFs at room temperature of 5Pb10YSB (a) and 1.5Pb25YSB (b) using PDFgui. The red line represents the theoretical PDF, the experimental data is represented by the blue circles, and the green line at the bottom of the plot represents the difference between the two.	124
Fig. 4.1 Typical impedance spectra of 5Pb10YSB (a), (b) 3.75Pb25YSB and 6Pb25YSB compositions in air at 300 °C.....	128
Fig. 4.2 EIS analysis of 5Pb10YSB measured at 300 °C with (a) Nyquist plots of experimental (symbols) and fitted results (lines) and (b) the equivalent circuit model used.	129
Fig. 4.3 Typical impedance spectra of (a) 5Pb10YSB, (b) 3.75Pb25YSB and 6Pb25YSB compositions in air at 500 °C.....	132
Fig. 4.4 EIS analysis of 5Pb10YSB measured at 500 °C with (a) Nyquist plots of experimental (symbols) and fitted results (lines) and (b) the equivalent circuit model used.	133
Fig. 4.5 Impedance spectra for (a) 5Pb10YSB, (b) 3.75Pb25YSB and 6Pb25YSB compositions in air at 700 °C.	134
Fig. 4.6 Impedance spectrum of 5Pb10YSB measured at 700 °C with a) Nyquist plots of experimental (symbols) and fitted results (lines) and (b) the equivalent circuit model used.	135
Fig. 4.7 Arrhenius plots of the bulk conductivity for 5Pb10YSB (a), 3.75Pb25YSB (b) and 6Pb25YSB (c) showing results from both the heating (blue/green lines) and the cooling cycles (red lines). Data for the first cycle is plotted in (a) and the second cycle in (b) and (c). A comparison of the cooling cycles of the three results is shown in (d).	139
Fig. 4.8 Arrhenius plot of conductivities both cooling cycles for 5Pb10YSB, 10YSB (a) and 3.75Pb10YSB, 27.5YSB (b).	145

List of Tables

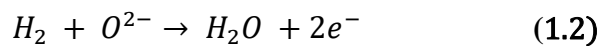
Table 1.1 Conditions, compositions and properties for five kinds of fuel cells. ²	4
Table 1.2 Structural data for Bi ₂ O ₃ phases ²⁰	7
Table 2.1 Approximate theoretical emission lines for different anode targets. ²²	49
Table 3.1 Input values used during a Rietveld refinement analysis Bi _{0.75(1-x)} Pb _{0.75x} Y _{0.25} O _{1.5-0.375x}	95
Table 3.2 Refined structural parameters for the (BiO _{1.5}) _{0.75-x} (PbO) _x (YO _{1.5}) _{0.25} system at room temperature using the cubic model with space group <i>Fm-3m</i> . R _{wp} is the weighted pattern residual and R _{exp} is the minimum achievable pattern residual, both of which are satisfactory values. Unfortunately, we could not measure the synchrotron data for 7.5Pb25YSB and 9Pb25YSB....	96
Table 3.3 Structural parameters for 5Pb10YSB obtained from Rietveld refinement of powder X-ray diffraction data at room temperature. Atomic positions (refer to table 3.1) space group <i>Fm-3m</i> of the cubic system.....	102
Table 3.4 Thermal expansion behavior of the annealed (at 750 °C) 5Pb10YSB and 1.5Pb25YSB materials over the temperature range of 27-706-27 °C. Values below indicate a steeper slope.	112
Table 4.1 Values of the resistance (<i>R_b</i>), frequency exponent (<i>a</i>), constant phase element (<i>Q_b</i>) and pseudo capacitance (<i>C_b</i>) for the bulk contribution of all the samples at different temperatures.	131
Table 4.2 Chi-square values obtained while fitting real data and the simulated data at several temperatures.....	137
Table 4.3 Bulk conductivity and resistance values obtained using different equivalent circuits at different temperatures, 300-450°C values were obtained using Fig. 4.2b, Fig. 4.4b for 500-600°C and Fig. 4.6b for 650-750°C.	138
Table 4.4 Derived electrical parameters for PbYSB compositions. 5Pb10YSB sample applies to the first cycle and the rest to the second cycle data.	143

1.1. Fuel Cells

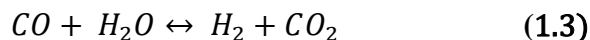
Fuel cells are electrochemical energy conversion devices that convert the chemical energy of fuels, directly into usable electrical energy that can be utilised to power devices and systems. A fuel cell single unit is subjected to a fuel oxidation reaction, normally a hydrogen reaction, and a reduction reaction which is normally oxygen from the air. Oxidation occurs at the fuel electrode known as the anode, and reduction occurs at the air electrode known as the cathode. While solid oxide fuel cell (SOFC) electrolytes are being investigated as possible proton conductive materials¹ oxygen ions migrate from the cathode to the anode in the 'typical' SOFC. At the cathode, oxygen ions are formed, according to the following overall reaction:¹



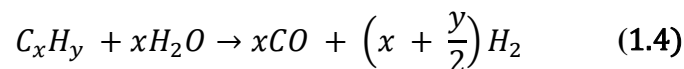
The electrolyte exhibits very high electrical resistivity and ionic conductivity at the operating temperature, so only ions can migrate to the anode. The following overall anode reaction occurs if hydrogen is regarded as fuel:



The water-gas shift reaction occurs if carbon monoxide is present:



Since CO has no poisoning effect on the anode materials, the additional fuel for the fuel cell is carbon monoxide. Hydrocarbons can also be reformed internally in accordance with the following reaction:



The reaction (Eqn. 1.4) typically does not occur in the anode at chemical equilibrium, so the shift reaction (Eqn. 1.3) occurs and provides additional hydrogen. The total reaction of fuel cells is²⁻⁴



Carbon monoxide and hydrocarbons can be oxidized directly at the anode, but the shift reaction (Eqn. 1.3) and the reforming process (Eqn. 1.4) are much faster, depending on the catalysts. When no current flows, the Nernst equation gives the voltage difference between the two electrodes,

$$E = E^0 + \frac{RT}{4F} \ln P_{O_2} + \frac{RT}{2F} \ln \frac{P_{H_2}}{P_{H_2O}} \quad (1.6)$$

where the reversible voltage is represented by E^0 at standard pressure, R is the universal gas constant, T represents the temperature, F being the Faraday constant and P representing the partial pressure of the species. However, the value provided by the Nernst equation generally shows a small deviation from the open circuit experimental values.²

To understand the electrochemistry taking place in the whole process, a physical description of a typical fuel cell device is required (Fig. 1.1). An electrolyte (non-porous material) is produced and directly sandwiched between the porous anode and cathode electrode. The two porous electrodes are either or both electronically and ionically conducting and are in contact with the electrolyte and constitute an external wire between the electrodes. Energy will be continuously produced from the device as long as the fuel and oxidant supply at the respective electrodes is constant. This makes fuel cells which are self-contained systems different and desirable alternatives to battery technologies in this respect.³

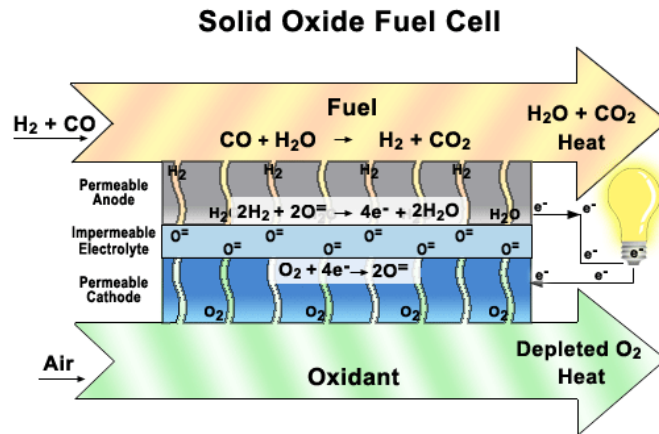


Fig. 1.1 The flow of electrons and oxygen anions through the outer circuit of a functional SOFC system.³

1.2. Types of Fuel Cells

Fuel cells are classified into five main kinds. The principal distinguishing factor is the form and nature of the electrolyte. The working temperature and the type of fuel utilised (liquid or gaseous) are also important variations. Molten Carbonate (MCFC), Alkaline (AFC), Solid Oxide (SOFC), Polymer Electrolyte Membrane (PEMFC) and Phosphoric Acid (PAFC) fuel cells are the main forms. Table 1.1² summarizes the various types of fuel cells with their inherent properties and composition of the components.

Table 1.1 Conditions, compositions and properties for five kinds of fuel cells.²

	Solid Fuel Cell (SOFC)	Oxide cell	Molten Carbonate Fuel Cell (MCFC)	Phosphoric Acid Fuel Cell (PAFC)	Alkaline Fuel Cell (AFC)	Polymer Electrolyte Fuel Cell (PEFC)
Typical Electrolyte	Solid YSZ [#]		Molten Li ₂ CO ₃ -K ₂ CO ₃	H ₃ PO ₄	KOH solution	PFS* acid membrane
Electrolyte Support	None		LiAlO ₂	SiC	Asbestos	None
Cathode	LSM (Sr-doped LaMnO ₃)		Li-doped NiO	PTFE**-bonded Pt on C	Pt-Au	PTFE-bonded Pt on C
Anode	Ni/YSZ		Ni	PTFE-bonded Pt on C	Pt-Pd	PTFE-bonded Pt on C
Interconnecting Material	Doped LaCrO ₃		Stainless steel with Ni	Glassy carbon	Ni	Graphite
Operating Temperature	1000°C		650°C	200°C	100°C	80°C
Operating Pressure	1 atm		1-3 atm	1-8 atm	1-10 atm	1-5 atm
Fuel (most common)	H ₂ , CO		H ₂ , CO	H ₂	H ₂	H ₂
Oxidant	O ₂		O ₂ and CO ₂	O ₂	O ₂	O ₂
Contaminant Tolerance	< -10-100 ppm S		<ppm range S	<1-2 % CO < 50 ppm S	No CO ₂ , CO No S	< 50 ppm CO No S

[#]YSZ = Yttria stabilized zirconia

*PFS = Perfluorosulfonic

**PTFE = Polytetrafluoroethylene

1.3. Electrolytes for Intermediate Temperature-SOFCs

As with all fuel cells, SOFCs comprise two electrodes and an electrolyte. All these components are made of ceramic materials, hence the alternative name 'ceramic fuel cell'. Both electrodes are porous while the electrolyte needs to be gas-tight. The use of stabilized zirconia-based materials as the electrolyte follows from experiments by Nernst in 1899. Bauer and Preis (1937)⁵ showed that at high temperatures (600-1000 °C) the solid solution comprising a 17:3 ratio of zirconia:yttria produced materials with sufficient ionic conduction for SOFCs. These days the most

common SOFC is made up of an yttria-stabilized zirconia (YSZ) electrolyte, with a nickel-YSZ cermet anode and a doped LaMnO₃ (LSM) cathode.

YSZ needs to work at a reasonably high temperature, usually greater than 700°C, in order to achieve reasonable ionic conductivity (around 15 S/m).⁶ In Initial design the electrolyte provided the mechanical strength to the cell, thus it was fairly thick causing a large ohmic drop and temperatures up to 1000 °C were required to give proper conductivity.⁶ The Westinghouse tubular cell used external (porous) supports but did not provide all operational requirements either and it was more complicated to manufacture.⁷ More recently either anode or cathode supported cells are being used.⁸ This allows for the reduction in the electrolyte thickness (down to microns). This biggest benefit from this is that the cells can operate at lower temperatures (~800 °C and lower) and still provide adequate conductivity. These kinds of SOFC are often referred to as intermediate temperature solid oxide fuel cells (ITSOFC). The benefits of running these cells at a lower temperature are: (i) the prospect of using stainless steel rather than costly ceramic interconnects as the current collectors, (ii) reduced system complexity and costs, (iii) improved chemical stability of the materials individually, (iv) reduced mismatching of single component thermal expansions and, and (v) shorter start-up and shutdown times.⁹

The contemporary SOFC with thick YSZ electrolyte and LSM cathode operating lower than 800 °C, does not provide sufficient power output.^{10,11} It is widely agreed today that to accelerate the widespread use of SOFCs would require lower operating temperatures, around 400-800 °C. At these low temperatures it is not only the electrolyte that has to be considered, as it has been shown that LSM does not catalyze the oxygen reduction reaction well at those temperatures either. Thus, research into improving the cathode material's activity is also being investigated.¹²⁻
¹⁴ Several review papers are more recently available on this topic, however there is less focus on the electrolytes at the moment.¹⁵⁻¹⁷ In this thesis, we specifically focus on advances in the development of new electrolytes for IT-SOFCs.

1.3.1. Phases and conductivity of pure Bi_2O_3

At present, fluorite-type oxides, which have a face-centered cubic arrangement of cations with anions occupying all the tetrahedral sites, are the most commonly used oxygen ion-conducting electrolyte materials for IT-SOFCs. Certain electrolytes, such as ZrO_2 and CeO_2 , require doping with cations of lower valence to introduce oxide ion vacancies thus creating conducting pathways for the oxygen ions. Stabilized Bi_2O_3 inherently has oxide ion vacancies but requires doping to stabilize the wanted phase. These defect fluorite structured materials can be used as electrolytes for IT-SOFCs.¹⁸

Bi_2O_3 -based oxides electrolytes have superior conductivity at lower temperatures compared to the doped ceria materials and are thus the focus of attention here. There are four distinct crystal structures in the pristine Bi_2O_3 : The low temperature α phase is monoclinic. It transforms into the face-centered cubic δ phase at 729 °C, which is stable up to the melting point at 824 K. Large thermal hysteresis occurs on cooling and it is possible to obtain the metastable tetragonal β or body-centered cubic γ form.¹⁹

The transition to the β -phase at 650 °C or to the γ -phase at 639 °C depends on the cooling conditions. The β -phase transforms to the alpha-phase at 303 °C and the γ -phase at 500 °C when cooled, although the γ -phase may persist to room temperature with slow cooling rates. The structural data for these phases of Bi_2O_3 are summarized in Table 1.2. The α -monoclinic and γ -bcc phases are semiconductors while the β -tetragonal and δ -fcc forms are oxide ion conductors, with the δ -phase exhibiting the highest conductivity, making it the primary focus of our study.²⁰

Table 1.2 Structural data for Bi₂O₃ phases²⁰

Phase	δ	α	γ	β
Phase stability temperature range (°C)	729-824	<729	500-639*	330-650
Temperature(°C)	774	25	25	643
Structure	fcc	monoclinic	bcc	tetragonal
Space group	Fm $\bar{3}$ m	P2 ₁ /c	I23	P4 ₂ c
Space group number	225	14	197	114
a (Å)	5.6595	5.8496	10.268	7.738
b (Å)		8.1648		
c (Å)		7.5101		5.731
β (°)		112.977		

* May persist to room temperature.

δ -Bi₂O₃ with a defective fluorite structure is stable between 730 and 804 °C. Oxide ions occupy the tetrahedral sites and two of these remain unoccupied.²¹ The cubic structure of δ -Bi₂O₃ can be stabilized at room temperature by certain dopants, such as Y³⁺, Pr³⁺ and Er³⁺. Therefore, certain stabilized δ -Bi₂O₃ oxides display higher oxide conductivity than doped CeO₂, and excellent kinetics of oxygen surface exchange which facilitates migration and diffusion of oxygen at the interface between the cathode and the electrolyte.²²⁻²⁵

Harwig²⁶ systematically measured the conductivity of the β , δ , γ and α -phases. Typical findings obtained during repeated heating and cooling runs are shown in Fig. 1.2. At the $\alpha \rightarrow \delta$ transition at 723 °C, electrical conductivity of Bi₂O₃ increases by four orders of magnitude. There is a hysteresis on cooling and a transition to the intermediate γ - and β - phases is found to be 80-90 °C lower than 723 °C. The transition from the intermediate metastable phases to the stable α -phase is not reproducible and does not take place at a finite temperature.²⁶

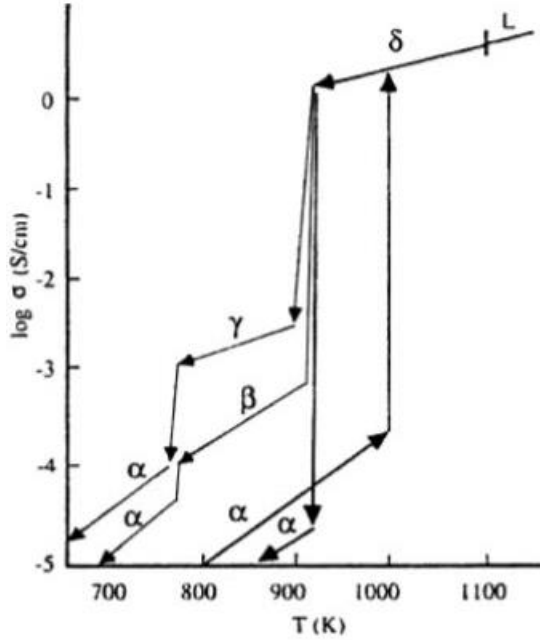


Fig. 1.2 Conductivity as $\log \sigma$ versus temperature for Bi_2O_3 .²⁶

Electronic conduction (transference number $t_{ion} < 0.002$ ²⁷) dominates the overall conductivity of the α - Bi_2O_3 phase; holes are the mobile charge carriers. The extent of electronic defects is determined by impurities. Through the whole temperature range up to the $\alpha \rightarrow \delta$ transition, these properties are found. With formation of the δ -phase the concentration of oxygen vacancies increases in the 650-729 K temperature range and contributes to an increase in ionic (oxide) conductivity.²⁶ The activation enthalpies as calculated from the temperature dependence of the ionic conductivity are 132, 95 and 38.5 kJ/mol for the β -, γ - and δ -phases, respectively.²⁶ Conduction in the metastable β - and γ -phases, is mainly poorly ionic.^{26,27}

Mobile oxide ions are the major charge carriers in δ - Bi_2O_3 .^{28,29} Interestingly, the δ -phase conductivity does not depend on the partial pressure of oxygen all the way down to 10^{-3} Pa.²⁶ It emphasizes the role of the high intrinsic disorder (and hence entropy) within δ - Bi_2O_3 leading to the high oxide mobility. Neutron diffraction studies at high temperatures confirmed that the oxygen sublattice is disordered and is even described as more "liquid-like".²⁶ The reasons for the high oxide ion conductivity of δ - Bi_2O_3 have recently been summarized by Mairesse³⁰: (i) In a

fluorite-type structure, one out of every four oxygen sites is empty; (ii) Bi^{3+} ion's electronic structure is distinguished by the presence of $6s^2$ lone pair electrons, contributing to the very high polarizability of the cation network that favors the mobility of oxide ions; (iii) Bi^{3+} ion's ability to tolerate highly disordered oxygen surroundings. Another benefit of electrochemical application is the ability of Bi^{3+} to facilitate oxygen molecule dissociation. While the highest oxide ion conductivity of the $\delta\text{-Bi}_2\text{O}_3$ is known to date, its use is limited because it is only stable in the narrow temperature range of 729-824 °C.

1.3.2. Structure of pure $\delta\text{-Bi}_2\text{O}_3$

The fluorite-based material, cubic bismuth oxide ($\delta\text{-Bi}_2\text{O}_3$), has one of the highest known oxygen conductivities, suggesting it would be a good contender as an electrolyte material in SOFCs. Unfortunately, this phase is only stable over the limited temperature range as it melts at 825 °C³¹ and transforms at 730 °C^{31,32} into the monoclinic phase which is an electronic conductor. Melting is less likely to be an issue if applied in IT-SOFCs (below 650 °C) than the formation of the monoclinic phase. Thus, the $\delta\text{-Bi}_2\text{O}_3$ is stabilized by doping with a range of metal ions, including the trivalent lanthanides, in order to expand the stability range to lower temperatures. Unfortunately, the introduction of dopants also leads to ordering of the oxygen sublattice³³, resulting in declined conductivity (Fig. 1.3). Electrolyte materials with lower conductivity, including yttria-stabilized zirconia (YSZ) and doped ceria, also exhibit similar decays in conductivity.³⁴

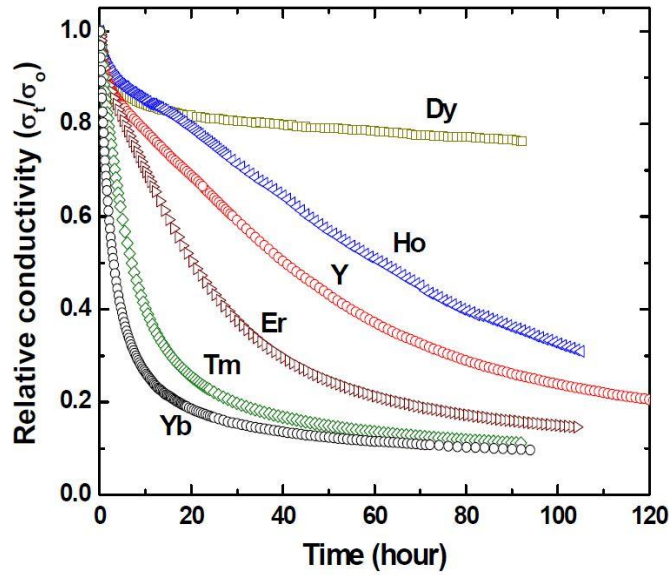


Fig. 1.3 Decrease in relative conductivity of δ -Bi₂O₃ doped with different dopants (25 mol% dopant composition). Different dopants have different decay rate. σ_t refers to conductivity at time t while σ_0 is the initial conductivity.³³

The ordering of the oxygen sublattice occurs when the initial randomly distributed oxygen vacancies arrange in an ordered fashion. Using computational methods, it was demonstrated that this reorganization leads to ordering in the $\langle 110 \rangle$ and $\langle 111 \rangle$ directions.³⁵ In neutron-diffraction experiments³⁶ performed on rare-earth-doped δ -Bi₂O₃, identical vacancy ordering was also observed. In order to identify the lowest energy vacancy-ordered structure of δ -Bi₂O₃, comprehensive research has been carried out and $\langle 100 \rangle$ ³⁷⁻⁴⁰, $\langle 110 \rangle$ $\langle 11 \rangle$ or $\langle 111 \rangle$ ⁴¹ vacancy-ordering models have also been suggested. From first-principle calculations, Dilpuneet *et. al.*⁴² shown that $\langle 110 \rangle$ - $\langle 111 \rangle$ is the lowest energy model of either $\langle 100 \rangle$, $\langle 110 \rangle$, or $\langle 111 \rangle$.

Another factor playing a role in the high conductivity of pure δ -Bi₂O₃ can also partly be ascribed to high polarizability of its lone electron pair of $6s^2$. Considering some of the lanthanide dopants (such as trivalent Yb, Er, Ho, Dy) used to stabilize the δ -Bi₂O₃-phase, it is not surprising that a decreased conductivity is noted since they have smaller ionic radii as well as lower polarizability compared to the host Bi³⁺ ions.^{33,43} It has been shown that the relative decay rate of doped-Bi₂O₃

conductivity actually has a linear dependency on both the dopant size and the polarizability, according to experimental studies.^{33,43} The radii⁴⁴ and polarizability⁴⁵ of the multiple dopants and Bi^{3+} are shown in Fig. 1.4.

Since there is a linear relationship between the ionic polarizability and radius, it is near impossible to distinguish a clear causal relationship. However, based on dielectric impedance results, Wachsman et al.⁴³ proposed that the dominant factor was polarizability. Dysprosium, which has the largest radius and highest polarizability of all dopants, showed the lowest conductivity decay (Fig. 1.3).³³ These experiments have led to the production of electrolytes based on Bi_2O_3 doped with Dy, with significantly improved performance.⁴⁶ Notwithstanding this achievement, further production of high-performance Bi_2O_3 -based electrolytes would be greatly encouraged if the individual contributions of the ionic radius and polarizability to the decay of conductivity can be isolated, which is impossible by experiment.

Computer simulations, however, prove optimal for such impacts to be isolated. Wachsman et al.⁴³ demonstrated that cation polarizability appears to be the main factor in enhancing ionic conductivity when using shell-model molecular-dynamics (MD) simulations. This allows the ionic polarizability and ionic radius to be altered independently. $\delta\text{-Bi}_2\text{O}_3$ has a defective fluorite structure in which 25% of the oxygen sub-lattice sites are empty. The high concentration of intrinsic defects gives this material great ionic conductivity. The $\delta\text{-Bi}_2\text{O}_3$ unit cell comprise of six anions in the eight tetrahedral positions (8c) and four cations in the fcc positions.

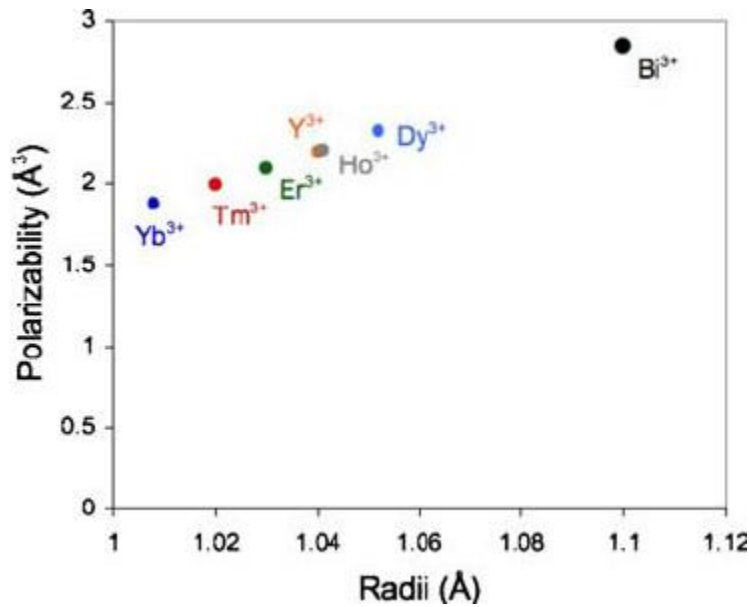


Fig. 1.4 The ionic radii and polarizabilities of lanthanide dopants typically added to δ -Bi₂O₃ are considerably less than those of Bi³⁺.⁴⁵

The identity of the positioning between the two anion vacancies and the six anions has been a controversial subject. Few different models were suggested to describe the cubic high-temperature phase of pure δ -Bi₂O₃⁴⁷⁻⁴⁹. While quenching Bi₂O₃, Sillen⁵⁰ obtained a primitive cubic phase, space group *Pn3m*. This cubic structure is associated to the structure of fluorite but has ordered defects in the direction of the O₂ sublattice $\langle 111 \rangle$ (Fig. 1.5). Each Bi³⁺ ion has six O₂ neighbours organised at six cube corners; there is a lack of two O₂ at diagonally opposite cube corners.

According to high-temperature X-ray powder diffraction, the analysis by Gattow and Schröder⁵¹ into the δ -Bi₂O₃ system revealed that the δ -phase of Bi₂O₃ is FCC. They dismissed the model proposed by Sillen⁵⁰ of an ordered defect O₂ sublattice with defects in the $\langle 111 \rangle$ direction and alternatively indicated that the structure was built on the δ -CaF₂ structure with the *Fm* $\bar{3}$ *m* space group, shown in Fig. 1.6. The *4a* site was occupied by the cations and the *8c* site was occupied by oxygen atoms with a standard occupancy of 3/4 and a random placement of vacancies. The high conductivity of O²⁻ ions shown by δ -Bi₂O₃ is consistent with a structural model in which the statistically occupied oxide ion sites are 3/4^{51,52}.

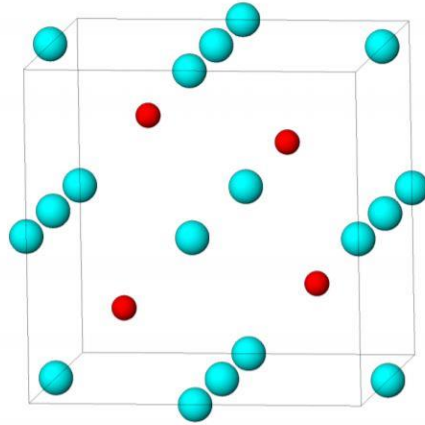


Fig. 1.5 Sillen model⁵⁰, where the light blue spheres represent O₂ and the red spheres represent Bi³⁺ ion.

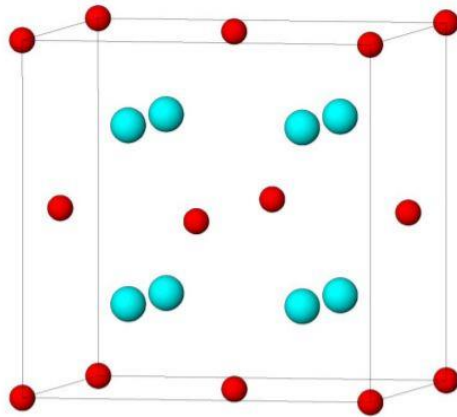


Fig. 1.6 The Gattow and Schröder model⁵², where the blue spheres represent O₂ and the red spheres represent Bi³⁺ ion.

A model where the six O₂ atoms are randomly dispersed along four of the $\langle 111 \rangle$ directions from the normal tetrahedral sites, $8c$, to the central octahedral unoccupied site, $32f$, of the $Fm\bar{3}m$ space group was also proposed by Willis⁵³. However, these models do not support the observed experimental results. Studies conducted by Battle et al.⁵⁴ show that oxide sublattice is a mixture of the Gattow and Willis models (i.e. the occupancy of both $32f$ and $8c$ sites) and indicate that vacant oxygen sites appear to be arranged around the Bi atoms in a $\langle 111 \rangle$ configuration, a

recognized component of fluorite materials deficient in anions. The fundamental structure of δ -phase⁵⁴ (Fig. 1.7) contains two partly occupied oxygen sites: $32f(x,x,x)$ with $x \approx 0.3$ and $8c(1/4,1/4,1/4)$.

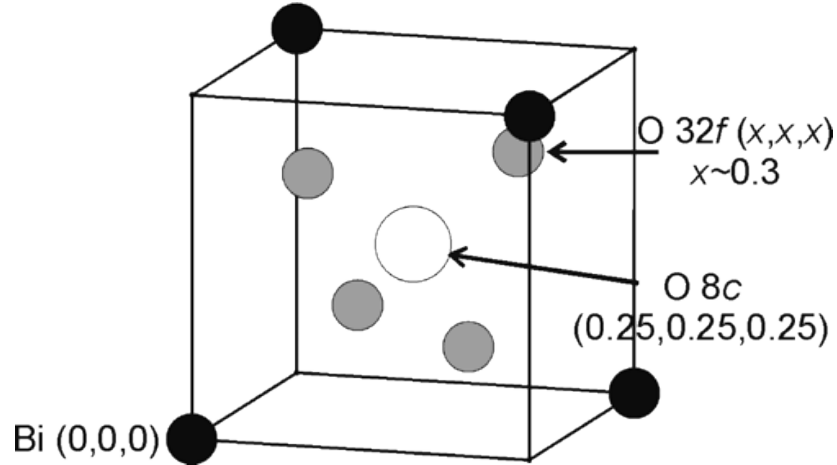


Fig. 1.7 Segment of δ - Bi_2O_3 ⁵⁴ unit cell displaying oxygen positions.

Doping of Bi_2O_3 does not always produce the δ -phase with the fcc structure. A rhombohedral structure similar to the Bi_2O_3 -SrO rhombohedral structure analysed by Sillen et al.⁵⁵ or the LaOF-rhombohedral structure⁵⁶ has been established. The structure type that forms is contingent on both the ion radius and concentration of the dopant cations. Fig. 1.8 indicates the fcc and rhombohedral phase regions that are stable at room temperature as a function of the Ln^{3+} ion radius and content.⁵⁷ Due to the calculation of concentration at relatively low and high Ln_2O_3 , the thin lines indicate the limits of accuracy. Generally, in systems doped with Ln_2O_3 , ($\text{Ln} = \text{La}, \text{Nd}, \text{Sm}, \text{Gd}$), with relatively large ion radii and relatively low x in $(\text{Bi}_2\text{O}_3)_{1-x}(\text{Ln}_2\text{O}_3)_x$ results with the formation of rhombohedral phase.

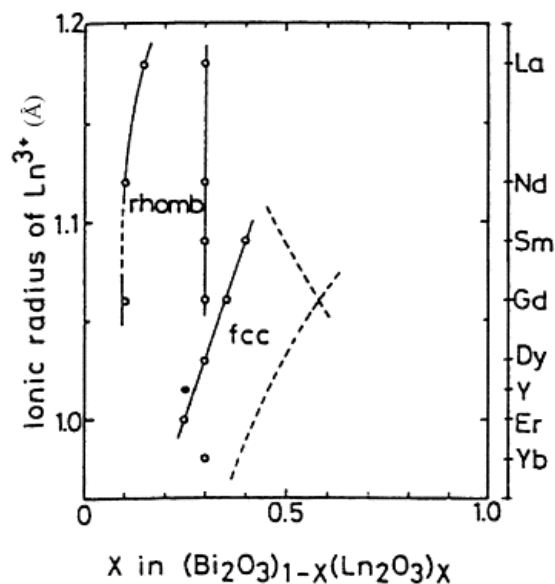


Fig. 1.8 δ - Bi_2O_3 formation spectrum of the fcc and rhombohedral phases in the ionic radius of Ln^{3+} versus composition diagram.⁵⁸

Dopants with smaller cationic radii than that for Bi^{3+} which are present at comparatively high concentrations stabilize the fcc phase of Bi_2O_3 . Verkerk et al.^{59,60} believed that, due to the substituent, stabilization of the relatively loose high temperature δ -phase takes place through a contraction of the structure. If there is a significant difference between the ionic radius of Bi^{3+} and the substituted ionic radius of Ln^{3+} , a large distortion of the host lattice would result, and only a small amount of substituent is needed to provide the energy required to stabilize the Bi_2O_3 fcc phase. In comparison, a small difference between Bi^{3+} and Ln^{3+} ionic radii require a significant amount of substituent to stabilize the fcc phase, as is the case for Gd^{3+} , for example (Fig. 1.8). The fcc phase is unstable because the gap between the ionic radii of the ions Ln^{3+} and Bi^{3+} is too large.⁵⁹

A large number of oxides based on ternary and quaternary Bi_2O_3 were synthesized and characterized.^{61,62} Instead of only one, the substitution of two different metal oxides favoured the stabilization of the δ -phase down to room temperature at a distinctly lower oxide concentration.⁶² Its cooperative effect was due to the rise in entropy. Battle et al.⁶² demonstrated that the ordering of oxide ions occurs along the $\langle 111 \rangle$ and $\langle 110 \rangle$ directions in $(\text{Bi}_2\text{O}_3)_{1-x}(\text{Y}_2\text{O}_3)_x$.

Both neutron dispersion and X-ray diffraction studies on solid solutions of the fluorite type $(\text{Bi}_2\text{O}_3)_{1-x} (\text{Ln}_2\text{O}_3)_x$ ($\text{Ln} = \text{Er}, \text{Yb}, \text{Y}$) confirmed important short-range ordering and it was clear that this ordering increased upon increasing the Ln concentration.⁶³ Other phases have also been found, such as the layered structure of $\text{Bi}_{0.765} \text{Sr}_{0.235} \text{O}_{1.383}$ displaying hexagonal symmetry in the bismuth-rich region.

1.3.3. Process of Ionic conduction

Verkerk et al.^{59,60} investigated the link between the ionic radius of the dopant ion, particularly concentrating on the lanthanide ions, Ln^{3+} , and the smallest amount of Ln_2O_3 (called x_{min}) needed to stabilize the Bi_2O_3 fcc phase, and further, the effect on conductivity of these factors. Fig. 1.9 shows the correlation between the ionic radius and x_{min} . It turns out that these two factors have contrasting effects in the way the conductivity is influenced.⁵⁹ First, as the ionic radius increases, the ionic conductivity increases (Fig. 1.10). Second, as the ionic radius increases it was seen that x_{min} also increases (Fig. 1.9), but the higher the x_{min} value means the oxide ion conductivity decreases. Of the two factors, the ionic radius appears to play the lesser role and thus it is rather sought to reduce the x_{min} value. Fig. 1.10 shows that stabilizing the Bi_2O_3 fcc phase using Er_2O_3 produced the material with the highest oxide conductivity when the lowest x_{min} was needed.⁵⁹

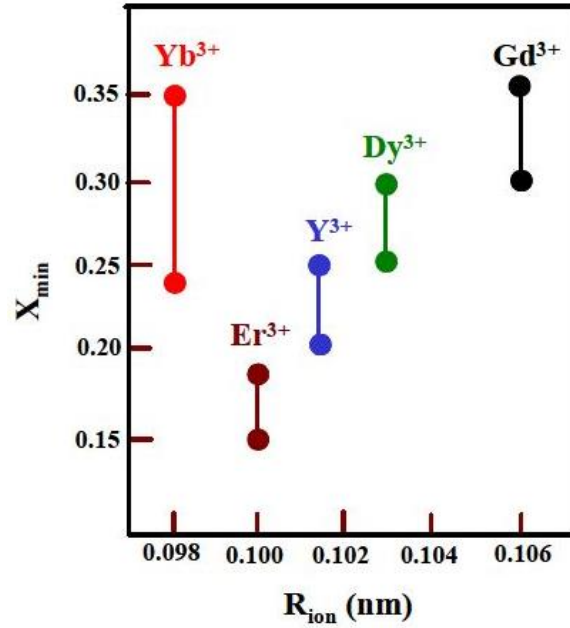


Fig. 1.9 x_{\min} , the minimum value of x needed to stabilize the δ -phase in $(\text{Bi}_2\text{O}_3)_{1-x}(\text{Ln}_2\text{O}_3)_x$ in relation to the ionic radius (R_{ion}) of the Ln^{3+} .⁵⁹

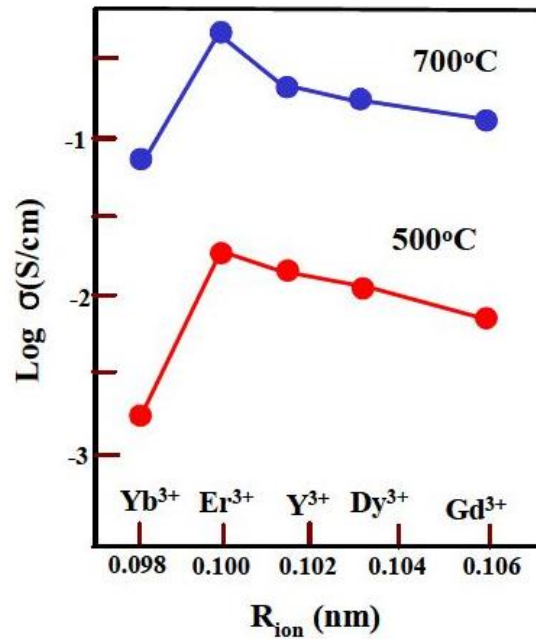


Fig. 1.10 $\text{Log } \sigma$, where σ represents the ionic conductivity of $(\text{Bi}_2\text{O}_3)_{1-x}(\text{Ln}_2\text{O}_3)_x$ and x is in the range of x_{\min} as shown in Fig. 1.9 (in relation to the ionic radius of the substituted Ln^{3+}).⁵⁹

As fully random arrangement of oxygen vacancies in a highly defective system unfortunately does not readily occur over the entire structure, instead it only happens over short ranges. A model suggested by Verkerk et al.⁶⁷ looking the short-range order, or order across micro-domains for $(\text{Bi}_2\text{O}_3)_{0.75} (\text{Y}_2\text{O}_3)_{0.25}$ is presented in Fig. 1.11. Each tetrahedron consists of three Bi^{3+} ions for this composition and one Ln^{3+} ion, signifying a (Bi_3Ln) tetrahedron. From the figure it is evident that two distinct O-O distances exist and that the oxide ions are located towards the Ln^{3+} ions. Diffuse neutron scattering studies of oxygen done at lower temperatures ($<597^\circ\text{C}$) have clearly observed these two O-O distances as 0.268 nm and 0.290 nm.⁶⁷

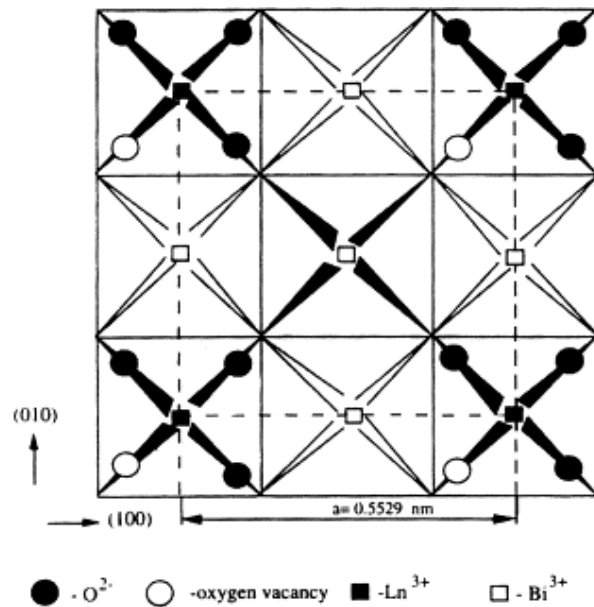


Fig. 1.11 Schematic representation of $(\text{Bi}_2\text{O}_3)_{0.75} (\text{Ln}_2\text{O}_3)_{0.25}$ ordered unit model, with a unit cell dimension of, $a = 5.529\text{\AA}$.⁶⁷

When the conductivity of solid solutions of Bi_2O_3 , stabilized with Dy_2O_3 ⁵⁹, Gd_2O_3 ⁶¹, Y_2O_3 ⁶² or Er_2O_3 ⁶³ was determined at about the same temperature (870 K), a knee in the Arrhenius plot was noted. A change in the defect structure was ascribed to this anomaly. The conductivity activation energy is determined by the Ln-O bond strength and by the energy needed for O^{2-} ions to migrate through the tetrahedral planes. The effect of Ln-O bond strength is more pronounced in the low-temperature region. For the oxide ion to migrate from one (Bi_3Ln) -tetrahedron to an adjacent empty site, the Ln-O bond must be broken, and the oxide ion must move through a tetrahedral

plane which can consist of $(\text{Ln}_2\text{Bi})^-$, $(\text{Bi}_2\text{Ln})^-$ or (Bi_3) , depending on the arrangement of the cations. The lattice disorders around 870 K result in an increase in the Ln-O distance implying greater mobility of the oxide ion.

At high temperatures all oxide ions are mobile and participate in the conductivity process and there are no preferential diffusion routes. The question remains as to which factor plays the dominant role at high temperatures, the strength of the Ln-O bond or energy required to move oxide ions through a tetrahedral plane. Detailed calculations are necessary to answer this.⁶⁷

1.3.4. Doping with lead and yttrium

In the last three decades, the sol-gel technique has grown in popularity as a research topic. This technique is scientifically and technologically interesting due to its reaction in the liquid phase, room temperature, and the type of precursors that are used to create new materials. Bi_2O_3 -based materials with high oxygen ionic conductivity have been actively investigated for their possible application as solid electrolytes in fuel cells over the last several decades.⁶⁸ At high temperatures, the delta face centered cubic (fcc) phase of pure Bi_2O_3 possesses high oxide ion conduction, although it is only stable between 730 and 825 °C (melting point). Large volume changes are associated by phase conversion from the delta phase to the monoclinic alpha phase, which possesses low electrical conductivity, after cooling from a high temperature. The addition of a sufficient amount of Ytria (Y^{3+}) or rare earth oxides to the FCC phase stabilizes it at lower temperatures.^{69,70}

In our research, we developed co-doped Bi_2O_3 with Pb^{2+} and Y^{3+} ($\text{Bi}_2\text{O}_3\text{-PbO-Y}_2\text{O}_3$ system). Besides the benefits of double substitution of Bi^{3+} (resulting in increased contribution of configuration entropy to the free energy³³), replacing Bi^{3+} with Pb^{2+} creates the possibility of higher concentrations of vacancies than in Bi_2O_3 , with potential benefits in electrical behaviour.

Studies conducted on Y_2O_3 doped Bi_2O_3 showed that the fcc phase is stable down to room temperature when the dopant content is between 25 and 42 mol%. Oxide migration is affected by the presence of the large dopant content and causes an increase in the Arrhenius energy and thus a decrease in the ionic conductivity. Battle et al.⁵⁴ published on the conductivity and

structure of Y-doped Bi_2O_3 . Where Y_2O_3 's content was 30%, the Arrhenius energy (also known as the activation energy which is extracted from the Arrhenius plots) increases to 0.7 eV from 0.4 eV for pure material⁵⁷. It is expected that the ionic conductivity would drop due to the high Y_2O_3 levels, but the Y^{3+} has no lone pair which is suggested to play a role in the high oxide conductivity of Bi_2O_3 . On the other hand, a variety of cations depress conductivity (such as Gd, Nb, Ta, W)⁵⁷. It is suggested that the mechanism by which oxide ion conduction occurs is independent of the type of cations in the lattice and thus the same mechanism is expected as for $\delta\text{-Bi}_2\text{O}_3$. This seems to be true on the surface but may be more complicated when looking at the conduction pathways which could be influenced by factors such as the strength of M-O bonds, the coordination around the metal ion and the presence of lone pairs.

Bi^{3+} and Pb^{2+} are isoelectronic meaning that both possess a lone pair. With the lone pair said to enhance the oxide conductivity, is it proposed that systems containing Pb^{2+} would also show improved conductivity provided the structure of the material is conducive to oxide mobility. In general, the structures of compounds in the $\text{Bi}_2\text{O}_3\text{-PbO}$ system are not very well known, but they have been found to form the tetragonal or β -phase.⁷¹ The β -phase also has a cubic symmetry and oxide conduction is also likely to be 3-dimensional. Not unexpectedly, the conductivity of the β $\text{Bi}_2\text{O}_3\text{-PbO}$ systems is comparable to that of $\delta\text{-Bi}_2\text{O}_3$. In fact, the parallel between Bi_2O_3 and Bi-Pb-O structures and conductivities is striking; thus, supporting the hypothesis of the link between a lone pair on the cation and the conductivity.

In addition, Pb^{2+} (with ionic radius 1.29 Å) has very indistinguishable structural properties similar to Bi^{3+} , as it is also strongly polarizable because of its stereochemically active $6s^2$ lone pair electrons and has an ionic radius comparable to Bi^{3+} (1.17 Å)³⁴. Studies conducted by Boivin et al. on the $\text{Bi}_2\text{O}_3\text{-PbO}$ system have shown that some of these solid solutions show high ionic conductivity ($9.20 \times 10^{-2} (\Omega\cdot\text{cm})^{-1}$) at ~ 600 °C, but unfortunately were found to be only stable within a narrow temperature range³⁵.

In replacing bismuth with the subvalent Pb^{2+} , additional oxide vacancies are introduced and if Pb^{2+} alone were substituted, it could give vacancy concentrations above that of pure $\delta\text{-Bi}_2\text{O}_3$. Apart from the related stereochemical behaviour of the $6s^2$ electron pairs, Pb^{2+} ions show several

additional similarities to Bi^{3+} . The polarizability for the neutral atoms of Pb and Bi are very much the same with $\alpha_D = 46$ and 50 a.u., respectively.⁷² When incorporated into oxide systems, both ions form distorted coordination environments. Despite these obvious similarities, it is only at elevated temperatures⁶⁹ that the cubic δ -phase is observed for the Bi_2O_3 -PbO binary system. However, it has been shown that δ -type phases can be sustained at room temperature in ternary systems of the Bi_2O_3 - MO_x -PbO type ($M = \text{Ca}, \text{Y}, \text{Er}$ and La).⁷³⁻⁷⁶

1.4. Aims and Objectives

SOFCS are energy conversion systems that are gaining popularity due to their many positive attributes. They can also be used as energy storage systems if they are designed as reversible SOFCs, meaning that they can electrolyse the consumed fuels, preferably using renewable energy sources. They are essentially made up of a solid ceramic electrolyte that generally conducts oxide ions (but some proton conducting materials are also being looked at) inserted between the anode and cathode. These cells are usually arranged in series into a fuel cell stack to supply the required voltages.

Although SOFCs are commercially available, there are a range of aspects that can still be improved upon. Currently the preferred solid oxide conducting electrolyte YSZ which requires the SOFC to operate above 800 °C to ensure it is sufficiently conducting. This is due to the thermally activated hopping mechanism of the ions through the lattice. Much research is underway to develop electrolytes that are ionic conductors at lower temperatures ($300 - 600$ °C).

The reason for wanting to run SOFCs at lower temperatures is many-fold. The electrode and electrolyte materials degrade faster at high temperatures due to high temperature oxidation, corrosion or phase transitions. Additionally, since the electrodes and electrolytes are in good contact with each other, chemical reactions between these components can occur or, if there is disparity in the thermal expansion of the different materials, delamination between these components can occur.⁷⁹ Also gas seals and interconnects between the cells in a fuel cell stack have to withstand the high temperatures and are thus made from more expensive materials

which increases the cost of the SOFCs.⁸⁰ The start-up and shut down cycles for high temperature SOFCs are also much longer. Therefore, if SOFCs are able to run efficiently at lower temperatures, the durability can be improved while the cost is decreased.

The aim of this work is to synthesize and study various doped and co-doped bismuth oxide materials to investigate whether the conductive δ -phase can be stabilised, and the thermal expansion reduced. The aim is to work towards a better understanding of these materials in terms of structure and ion conductivity so that better SOFC electrolytes can be designed to run at lower temperatures (between 300 – 600 °C). These materials will thus be studied at elevated temperature ranges. This work focuses on studying the Bi_2O_3 - Y_2O_3 - PbO ternary system to find which compositions produce a single-phase solid solution and also to gauge the total dopant percentage required to stabilize the Bi_2O_3 δ -phase. The oxide conductivity of this double doped system will also be studied with the aim of evaluating the effect of the presence of Pb^{2+} which is expected to enhance conductivity.

It is generally known that substituting yttrium for bismuth in Bi_2O_3 produces the highly conducting cubic δ -phase for a wide range of compositions^{76,77} as indicated in the review by Sammes et al.⁷⁸ In contrast, substituting lead for bismuth in Bi_2O_3 does not yield this same δ -phase at low temperatures.⁷² This is despite the number of similarities between the Bi^{3+} and Pb^{2+} cations as described. It is only in ternary systems, such as Bi_2O_3 - MO_x - PbO ($\text{M} = \text{Ca}^{3+}$, Y^{3+} , Er^{3+} and La^{3+}), where this phase is observed down to room temperature.⁷³⁻⁷⁶ Additional studies have shown that Pb^{2+} and Y^{3+} total content greater than 20 mol%^{33,54} readily stabilizes the δ -phase to room temperature.

Bi_2O_3 doped and co-doped materials will be synthesised using the sol-gel method. The samples will be analysed using differential thermal analysis (DTA) to gain insight into the initial thermal-dependent behaviour of the materials. The samples will also be characterised by powder X-ray diffraction (PXRD) at room temperature after sintering at different temperatures (using the DTA data as a guide) to build an understanding of the phase behaviour of the materials. Variable temperature (VT)-PXRD will also be done as an in-situ method to see more accurately where the phase changes occur, as well as to determine thermal expansion coefficients. VT-Raman

spectroscopy will be used to build a better understanding of the phase changes. VT-electrochemical impedance spectroscopy (EIS) will be used to determine whether each material is an ionic and/or electronic conductor and the temperature at which good conductivity is obtained.

1.5. References

1. Holze, R., 2008. S. Basu Ed.: Recent trends in fuel cell science and technology. *Journal of Solid-State Electrochemistry*, 13(10), pp.1623-1624.
2. Sachdeva, G., 2014. Modeling and Simulation of Fuel cell (Dicks Larminie Model) based 3-Phase Voltage Source Inverter. *International Journal of Electrical and Computer Engineering (IJECE)*, 4(5).
3. Hollins, P., 1988. Impedance spectroscopy: Emphasizing solid materials and systems. *Spectrochimica Acta Part A: Molecular Spectroscopy*, 44(8), p.853.
4. Holze, R., 2002. Book Review: Electrochemical Methods. Fundamentals and Applications (2nd Edition). By Allen J. Bard and Larry R. Faulkner. *Angewandte Chemie International Edition*, 41(4), pp.655-657.
5. Agnew, G. and Spangler, A., 2004. Reducing fuel cell system cost without lowering operating temperature. In *2nd International Conference on Fuel Cells Science Engineering and Technology (Rochester, NY)*, ASME.
6. Amaha, S., Baba, Y., Yakabe, H. and Sakurai, T., 2004. Improvement of the performance for the anode supported SOFCs. In *International Conference on Fuel Cell Science, Engineering and Technology* (Vol. 41650, pp. 45-48).
7. Bessette, N. and Wepfer, W., 1996. Prediction of on-design and off-design performance for a solid oxide fuel cell power module. *Energy Conversion and Management*, 37(3), pp.281-293.
8. Minh, N.Q. and Takahashi, T., 1995. *Science and technology of ceramic fuel cells*. Elsevier.
9. Holtappels, P., Bradley, J., Irvine, J.T.S., Kaiser, A. and Mogensen, M., 2001. Electrochemical characterization of ceramic SOFC anodes. *Journal of the Electrochemical Society*, 148(8), pp.A923.
10. Tsai, T. and Barnett, S.A., 1997. Effect of LSM-YSZ cathode on thin-electrolyte solid oxide fuel cell performance. *Solid State Ionics*, 93(3-4), pp.207-217.
11. Zhou, W., Shi, H., Ran, R., Cai, R., Shao, Z. and Jin, W., 2008. Fabrication of an anode-supported yttria-stabilized zirconia thin film for solid-oxide fuel cells via wet powder spraying. *Journal of Power Sources*, 184(1), pp.229-237.
12. Kuai, X., Yang, G., Chen, Y., Sun, H., Dai, J., Song, Y., Ran, R., Wang, W., Zhou, W. and Shao, Z., 2019. Boosting the Activity of BaCoFe_{0.4}Zr_{0.4}Y_{0.1}O_{3-δ} Perovskite for Oxygen Reduction Reactions at Low-to-Intermediate Temperatures through Tuning B-Site Cation Deficiency. *Advanced Energy Materials*, 9(38), p.1902384.
13. Tian, Y., Liu, Y., Wang, W., Jia, L., Pu, J., Chi, B. and Li, J., 2020. High performance and stability of double perovskite-type oxide NdBa_{0.5}Ca_{0.5}Co_{1.5}Fe_{0.5}O_{5-δ} as an oxygen electrode for reversible solid oxide electrochemical cell. *Journal of Energy Chemistry*, 43, pp.108-115.

14. Jeong, W., Yu, W., Lee, M.S., Bai, S.J., Cho, G.Y. and Cha, S.W., 2020. Ultrathin sputtered platinum–gadolinium doped ceria cathodic interlayer for enhanced performance of low temperature solid oxide fuel cells. *International Journal of Hydrogen Energy*, 45(56), pp.32442-32448.
15. Xu, X., Wang, W., Zhou, W. and Shao, Z., 2018. Recent advances in novel nanostructuring methods of perovskite electrocatalysts for energy-related applications. *Small Methods*, 2(7), pp.1800071.
16. Kaur, P. and Singh, K., 2020. Review of perovskite-structure related cathode materials for solid oxide fuel cells. *Ceramics International*, 46(5), pp.5521-5535.
17. Yang, G., Su, C., Shi, H., Zhu, Y., Song, Y., Zhou, W. and Shao, Z., 2020. Toward Reducing the Operation Temperature of Solid Oxide Fuel Cells: Our Past 15 Years of Efforts in Cathode Development. *Energy & Fuels*, 34(12), pp.15169-15194.
18. Goodenough, J.B., 2003. Oxide-ion electrolytes. *Annual Review of Materials Research*, 33(1), pp.91-128.
19. Brandon, N.P., Skinner, S. and Steele, B.C., 2003. Recent advances in materials for fuel cells. *Annual Review of Materials Research*, 33(1), pp.183-213.
20. Harwig, H.A., 1978. On the Structure of Bismuthsesquioxide: The α , β , γ , and δ -Phase. *Zeitschrift für anorganische und allgemeine Chemie*, 444(1), pp.151-166. Harwig, H.A. and Gerards, A.G., 1978. Electrical properties of the α , β , γ , and δ phases of bismuth sesquioxide. *Journal of Solid-State Chemistry*, 26(3), pp.265-274.
21. Berezovsky, J., Liu, H.K. and Dou, S.X., 1993. Conductivity and microstructure of bismuth oxide-based electrolytes with enhanced stability. *Solid State Ionics*, 66(3-4), pp.201-206.
22. Shuk, P., Wiemhöfer, H.D. and Göpel, W., 1997. Electronic Properties of Bi₂O₃-based Solid Electrolytes. *Zeitschrift für anorganische und Allgemeine Chemie*, 623, pp.892-896.
23. Jiang, N., Wachsman, E.D. and Jung, S.H., 2002. A higher conductivity Bi₂O₃-based electrolyte. *Solid State Ionics*, 150(3-4), pp.347-353.
24. Orlova, E.I., Kharitonova, E.P., Gorshkov, N.V., Goffman, V.G. and Voronkova, V.I., 2017. Phase formation and electrical properties of Bi₂O₃-based compounds in the Bi₂O₃-La₂O₃-MoO₃ system. *Solid State Ionics*, 302, pp.158-164.
25. Harwig, H.A. and Gerards, A.G., 1978. Electrical properties of the α , β , γ , and δ phases of bismuth sesquioxide. *Journal of Solid-State Chemistry*, 26(3), pp.265-274.
26. Shuk, P., Wiemhöfer, H.D., Guth, U., Göpel, W. and Greenblatt, M., 1996. Oxide ion conducting solid electrolytes based on bismuth oxide. *Solid State Ionics*, 89(3-4), pp.179-196.
27. Takahashi, T., Iwahara, H. and Nagai, Y., 1972. High oxide ion conduction in sintered Bi₂O₃containing SrO, CaO or La₂O₃. *Journal of Applied Electrochemistry*, 2(2), pp.97-104.
28. Takahashi, T., Esaka, T. and Iwahara, H., 1977. Oxide ion conduction in the sintered oxides of MoO₃-doped Bi₂O₃. *Journal of Applied Electrochemistry*, 7(1), pp.31-35.
29. Mairesse, G., Scrosati, B., Magistris, A., Mari, C. and Mariotto, G., 1993. Fast ion transport in solids. *Kluwer, Dordrecht, The Netherlands*, 372(1-2), p. 271.
30. Aurivillius, B. and Sillén, L.G., 1945. Polymorphy of bismuth trioxide. *Nature*, 155(3932), pp.305-306.
31. Rao, C.R., Rao, G.S. and Ramdas, S., 1969. Phase transformations and electrical properties of bismuth sesquioxide. *The Journal of Physical Chemistry*, 73(3), pp.672-675.
32. Jiang, N. and Wachsman, E.D., 1999. Structural stability and conductivity of phase-stabilized cubic bismuth oxides. *Journal of the American Ceramic Society*, 82(11), pp.3057-3064.
33. Inaba, H. and Tagawa, H., 1996. Ceria-based solid electrolytes. *Solid State Ionics*, 83(1-2), pp.1-16.

34. Aidhy, D.S., Nino, J.C., Sinnott, S.B., Wachsman, E.D. and Phillpot, S.R., 2008. Vacancy-Ordered Structure of Cubic Bismuth Oxide from Simulation and Crystallographic Analysis. *Journal of the American Ceramic Society*, 91(7), pp.2349-2356.
35. Wachsman, E.D., Boyapati, S., Kaufman, M.J. and Jiang, N., 2000. Modeling of ordered structures of phase-stabilized cubic bismuth oxides. *Journal of the American Ceramic Society*, 83(8), pp.1964-1968.
36. Walsh, A., Watson, G.W., Payne, D.J., Edgell, R.G., Guo, J., Glans, P.A., Learmonth, T. and Smith, K.E., 2006. Electronic structure of the α and δ phases of Bi₂O₃: A combined ab initio and x-ray spectroscopy study. *Physical Review B*, 73(23), p.235104.
37. Carlsson, J.M., Hellsing, B., Domingos, H.S. and Bristowe, P.D., 2002. Theoretical investigation of the pure and Zn-doped α and δ phases of Bi₂O₃. *Physical Review B*, 65(20), p.205122.
38. Skorodumova, N.V., Jonsson, A.K., Herranen, M., Strømme, M., Niklasson, G.A., Johansson, B. and Simak, S.I., 2005. Random conductivity of δ -Bi₂O₃ films. *Applied Physics Letters*, 86(24), p.241910.
39. Zhong, G., Wang, Y., Dai, Z., Wang, J. and Zeng, Z., 2009. Oxygen vacancy configuration of δ -Bi₂O₃: an ab initio study. *Physica Status Solidi (b)*, 246(1), pp.97-101.
40. Aidhy, D.S., Sinnott, S.B., Wachsman, E.D. and Phillpot, S.R., 2010. Effect of ionic polarizability on oxygen diffusion in δ -Bi₂O₃ from atomistic simulation. *Ionics*, 16(4), pp.297-303.
41. Medvedeva, N.I., Zhukov, V.P., Gubanov, V.A., Novikov, D.L. and Klein, B.M., 1996. Electronic structure and chemical bonding in δ -Bi₂O₃. *Journal of Physics and Chemistry of Solids*, 57(9), pp.1243-1250.
42. Wachsman, E.D., Boyapati, S. and Jiang, N., 2001. Effect of dopant polarizability on oxygen sublattice order in phase-stabilized cubic bismuth oxides. *Ionics*, 7(1-2), pp.1-6.
43. Shannon, R.D., 1976. Revised effective ionic radii and systematic studies of interatomic distances in halides and chalcogenides. *Acta crystallographica section A: crystal physics, diffraction, theoretical and general crystallography*, 32(5), pp.751-767.
44. Shirao, K., Iida, T., Fukushima, K. and Iwadate, Y., 1998. Refractive indexes and electronic polarizabilities of molten HoCl₃-NaCl and HoCl₃-KCl mixtures. *Journal of Alloys and Compounds*, 281(2), pp.163-168.
45. Jiang, N., Wachsman, E.D. and Jung, S.H., 2002. A higher conductivity Bi₂O₃-based electrolyte. *Solid State Ionics*, 150(3-4), pp.347-353.
46. Google Books. 2021. *X-Ray Studies on Bismuth Trioxide*. [online] Available at: <https://books.google.com/books/about/X_Ray_Studies_on_Bismuth_Trioxide.html?id=c9KdGwAACAAJ> [Accessed 9 December 2021].
47. Willis, B.T.M., 1965. The anomalous behaviour of the neutron reflexion of fluorite. *Acta Crystallographica*, 18(1), pp.75-76.
48. Sillén, L.G., 1937. X-ray studies on bismuth trioxide. Friedländer.
49. Punn, R., Feteira, A.M., Sinclair, D.C. and Greaves, C., 2006. Enhanced oxide ion conductivity in stabilized δ -Bi₂O₃. *Journal of the American Chemical Society*, 128(48), pp.15386-15387.
- Gattow, G. and Schütze, D., 1964. About bismuth oxides. VI. Above bismuth (III) oxide with a higher oxygen content (β modification). *Journal of Inorganic and General Chemistry*, 328 (1-2), pp.44-68.
50. Willis, B.T.M., 1965. The anomalous behaviour of the neutron reflexion of fluorite. *Acta Crystallographica*, 18(1), pp.75-76.
51. Battle, P.D., Catlow, C.R.A., Drennan, J. and Murray, A.D., 1983. The structural properties of the oxygen conducting δ phase of Bi₂O₃. *Journal of Physics C: Solid State Physics*, 16(17), p.L561.

52. Sillén, L.G. and Aurivillius, B., 1939. Oxide phases with a defect oxygen lattice. *Zeitschrift für Kristallographie-Crystalline Materials*, 101(1-6), pp.483-495.
53. Zachariasen, W.H., 1951. Crystal chemical studies of the 5f-series of elements. XIV. Oxyfluorides, XOF. *Acta Crystallographica*, 4(3), pp.231-236.
54. Iwahara, H., Esaka, T., Sato, T. and Takahashi, T., 1981. Formation of high oxide ion conductive phases in the sintered oxides of the system Bi_2O_3 Ln_2O_3 (Ln= La, Yb). *Journal of Solid-State Chemistry*, 39(2), pp.173-180.
55. Takahashi, T., Esaka, T. and Iwahara, H., 1977. Conduction in Bi_2O_3 -based oxide ion conductor under low oxygen pressure. II. Determination of the partial electronic conductivity. *Journal of Applied Electrochemistry*, 7(4), pp.303-308.
56. Verkerk, M.J. and Burggraaf, A.J., 1981. High Oxygen Ion Conduction in Sintered Oxides of the Bi_2O_3 - Dy_2O_3 System. *Journal of the Electrochemical Society*, 128(1), p.75.
57. Verkerk, M.J., Middelhuis, B.J. and Burggraaf, A.J., 1982. Effect of grain boundaries on the conductivity of high-purity ZrO_2 - Y_2O_3 ceramics. *Solid State Ionics*, 6(2), pp.159-170.
58. Shuk, P., Wiemhöfer, H.D., Guth, U., Göpel, W. and Greenblatt, M., 1996. Oxide ion conducting solid electrolytes based on Bi_2O_3 . *Solid State Ionics*, 89(3-4), pp.179-196.
59. Battle, P.D., Catlow, C.R.A., Heap, J.W. and Moroney, L.M., 1986. Structural and dynamical studies of δ - Bi_2O_3 oxide ion conductors: I. The structure of $(\text{Bi}_2\text{O}_3)_{1-x}(\text{Y}_2\text{O}_3)_x$ as a function of x and temperature. *Journal of Solid-State Chemistry*, 63(1), pp.8-15.
60. Battle, P.D., Catlow, C.R.A., Chadwick, A.V., Cox, P., Greaves, G.N. and Moroney, L.M., 1987. Structural and dynamical studies of δ - Bi_2O_3 oxide ion conductors: IV. An EXAFS investigation of $(\text{Bi}_2\text{O}_3)_{1-x}(\text{M}_2\text{O}_3)_x$ for M= Y, Er, and Yb. *Journal of Solid-State Chemistry*, 69(2), pp.230-239.
61. Watanabe, A. and Kikuchi, T., 1986. Cubic-hexagonal transformation of yttria-stabilized Σ -bismuth sesquioxide, $\text{Bi}_{2-2x}\text{Y}_{2x}\text{O}_3$ (x= 0.215– 0.235). *Solid State Ionics*, 21(4), pp.287-291.
62. Watanabe, A., 1989. Phase relations of hexagonal and cubic phases in holmia-doped bismuth sesquioxide, $\text{Bi}_{2-2x}\text{Ho}_{2x}\text{O}_3$ (x= 0.205–0.245). *Solid State Ionics*, 34(1-2), pp.35-39.
63. Boivin, J.C. and Thomas, D.J., 1981. Crystal chemistry and electrical properties of bismuth-based mixed oxides. *Solid State Ionics*, 5, pp.523-525.
64. Sammes, N.M., Tompsett, G.A., Näfe, H. and Aldinger, F., 1999. Bismuth based oxide electrolytes—structure and ionic conductivity. *Journal of the European Ceramic Society*, 19(10), pp.1801-1826.
65. Biefeld, R.M. and White, S.S., 1981. Temperature/Composition Phase Diagram of the System Bi_2O_3 - PbO . *Journal of the American Ceramic Society*, 64(3), pp.182-184.
66. Sammes, N.M., Tompsett, G., Phillips, R., Carson, C., Cartner, A.M., Fee, M.G. and Yamamoto, O., 1996. Characterisation and stability of the fast ion conductor $(\text{Bi}_2\text{O}_3)_{1-x}(\text{PbO})_x$. *Solid State Ionics*, 86, pp.125-130.
67. Drache, M. and Con, P., 1992. ant and JC Boivin. *Solid State Ionics*, 57, p.245.
68. Fruth, V., Ianculescu, A., Berger, D., Preda, S., Voicu, G., Tenea, E. and Popa, M., 2006. Synthesis, structure and properties of doped Bi_2O_3 . *Journal of the European Ceramic Society*, 26(14), pp.3011-3016.
69. Narang, S.N., Patel, N.D. and Kartha, V.B., 1994. Infrared and Raman spectral studies and normal modes of α - Bi_2O_3 . *Journal of Molecular Structure*, 327(2-3), pp.221-235.

70. Mallahi, M., Mazinani, V., Shokuhfar, A. and Vaezi, M.R., 2014. Synthesis of yttria-doped Bi₂O₃ nanopowders via sol gel used in electrolyte of solid oxide fuel cell. *International Journal of Engineering Research*, 3(4), pp.267-270.
71. Drache, M., Schrotter, J.C. and Conflant, P., 1993. Evidence for oxygen nonstoichiometry in a stabilized Bi–Ca–Pb–O fluorite-type phase. *Journal of Materials Chemistry*, 3(8), pp.789-792.
72. Benkaddour, M., Steil, M.C., Drache, M. and Conflant, P., 2000. The influence of particle size on sintering and conductivity of Bi_{0.85}Pr_{0.105}V_{0.045}O_{1.545} ceramics. *Journal of Solid-State Chemistry*, 155(2), pp.273-279.
73. Webster, N.A., Ling, C.D., Raston, C.L. and Lincoln, F.J., 2007. The structure and conductivity of new fluorite-type Bi₂O₃–Er₂O₃–PbO materials. *Solid State Ionics*, 178(25-26), pp.1451-1457.
74. Takahashi, T., Iwahara, H. and Arao, T., 1975. High oxide ion conduction in sintered oxides of the system Bi₂O₃–Y₂O₃. *Journal of Applied Electrochemistry*, 5(3), pp.187-195.
75. Punn, R., Feteira, A.M., Sinclair, D.C. and Greaves, C., 2006. Enhanced oxide ion conductivity in stabilized δ-Bi₂O₃. *Journal of the American Chemical Society*, 128(48), pp.15386-15387.
76. Datta, R.K. and Meehan, J.P., 1971. The System Bi₂O₃–R₂O₃ (R= Y, Gd). *Zeitschrift für Anorganische und Allgemeine Chemie*, 383(3), pp.328-337.
77. Watanabe, A. and Kikuchi, T., 1986. Cubic-hexagonal transformation of yttria-stabilized Σ-bismuth sesquioxide, Bi_{2-2x}Y_{2x}O₃ (x= 0.215– 0.235). *Solid State Ionics*, 21(4), pp.287-291.
78. Sammes, N.M., Tompsett, G.A., Näfe, H. and Aldinger, F., 1999. Bismuth based oxide electrolytes—structure and ionic conductivity. *Journal of the European Ceramic Society*, 19(10), pp.1801-1826.
79. Zhang, Y., Knibbe, R., Sunarso, J., Zhong, Y., Zhou, W., Shao, Z. and Zhu, Z., 2017. Recent progress on advanced materials for solid-oxide fuel cells operating below 500 C. *Advanced Materials*, 29(48), pp.1700132.
80. Gao, Z., Mogni, L.V., Miller, E.C., Railsback, J.G. and Barnett, S.A., 2016. A perspective on low-temperature solid oxide fuel cells. *Energy & Environmental Science*, 9(5), pp.1602-1644.

2.1. Synthesis of co-doped Bi₂O₃

Selected samples in the Bi₂O₃-Y₂O₃-PbO system were synthesised using a sol-gel method of a stoichiometric mixture of Bi(NO₃)₃·6H₂O, Y(NO₃)₃·6H₂O and Pb(NO₃)₂. Fig. 2.1 shows the schematic representation for the synthesis of co-doped Bi₂O₃. The starting compounds were all high purity (≥99.99 % Aldrich) powders. Stoichiometric mixtures of all nitrates were dissolved in 100 ml of glacial acetic acid (99.99%, Sigma-Aldrich) mixed with 50 ml of deionized water. In a separate beaker citric acid (99.5%, Sigma-Aldrich, ~10 g) was dissolved in acetic acid and then added to the mixture. The solution was continuously stirred using a magnetic stirrer for 2 hours and then a sol formed. The sol was heated to 90 °C for 1h to form a yellowish gel. This gel was decomposed at 160°C in oven. The gel initially started to swell and filled the beaker producing a foamy precursor. This foam consists of homogeneous flakes of very small particle size.

The gel was then dried in a fume-hood overnight, followed by a calcination step at 450°C for 8 hours. The samples were ground manually using an agate mortar for ~30 min, transferred into an alumina crucible then annealed at 700°C for 12 hours in air. Some samples were further annealed at 750°C for 16 hours while others at 800°C for 16 hours. Initially Y composition was fixed to 25 mol%. At the end of each heat treatment procedure, the annealed powders were various (BiO_{1.5})_{0.75-x} (PbO)_x (YO_{1.5})_{0.25} compositions with a fixed yttrium composition were prepared (where x = 0.015, 0.0375, 0.06, 0.075, 0.09, 0.1125, 0.15, 0.1875, 0.225).

Based on the percentage of the metal content we have adopted this naming, 1.5Pb25YSB for a composition where x = 0.015, with 1.5% being that of Pb²⁺, 25% Y³⁺ and the rest (73.5%) being that of Bi³⁺. The other samples are referred to as 3.75Pb25YSB, 6Pb25YSB, 7.5Pb25YSB, 9Pb25YSB, 11.3Pb25YSB, 15Pb25YSB, 18.8Pb25YSB, 22.5Pb25YSB respectively. Subsequently, another batch of samples (with lower total dopant concentration) were prepared with different compositions. Both lead and yttria compositions were varied and the samples were synthesized as stated before. The following compositional series were examined:

- I. (BiO_{1.5})_{0.90} (PbO)_x (YO_{1.5})_{0.10-x} (x = 0.02, 0.03)

- II. $(\text{BiO}_{1.5})_{0.88} (\text{PbO})_x (\text{YO}_{1.5})_{0.12-x}$ ($x = 0.03, 0.04$)
- III. $(\text{BiO}_{1.5})_{0.85} (\text{PbO})_x (\text{YO}_{1.5})_{0.15-x}$ ($x = 0.05, 0.075, 0.10$)
- IV. $(\text{BiO}_{1.5})_{0.80} (\text{PbO})_x (\text{YO}_{1.5})_{0.20-x}$ ($x = 0.05$)

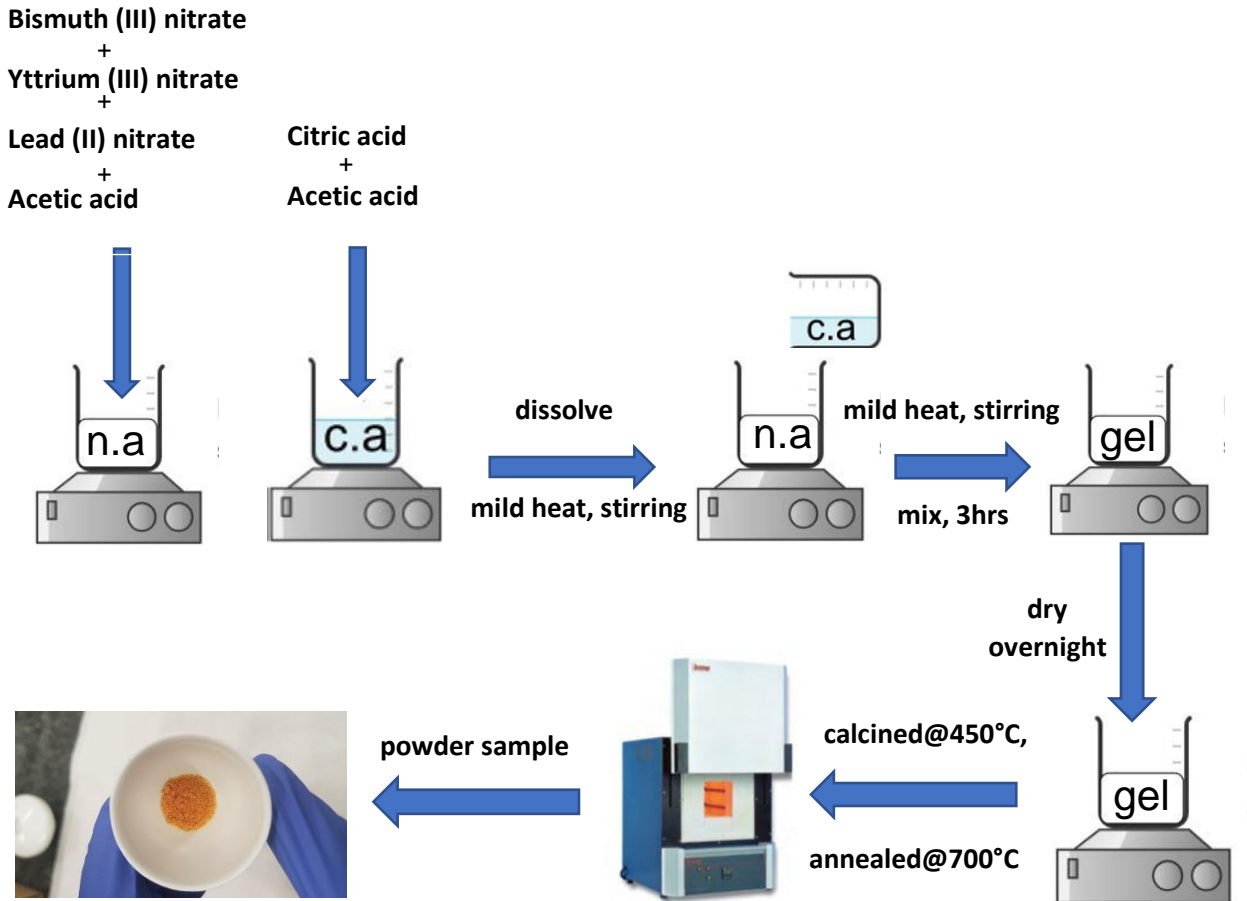


Fig. 2.1 Schematic representation of synthetic route for lead yttrium stabilized bismuth oxide (PbYSB) in a powder form obtained by calcining at 450°C, followed by annealing at 700°C in a furnace.

Omari et al.¹ investigated the $\text{Bi}_2\text{O}_3\text{-Y}_2\text{O}_3\text{-PbO}$ system in 1990, incorporating the good stability of the $\text{Bi}_2\text{O}_3\text{-Y}_2\text{O}_3$ system with high performance of the $\text{Bi}_2\text{O}_3\text{-PbO}$ system. This was sufficiently accomplished within some ratios of composition. They reported the variation in the lattice parameter with changing compositional ratios for $(\text{BiO}_{1.5})_{0.75-x} (\text{PbO})_x (\text{YO}_{1.5})_{0.25}$. They deduced that the double substitution of Pb^{2+} and Y^{3+} for Bi^{3+} in Bi_2O_3 could result in stabilized high

conductivity phases of δ -Bi₂O₃. In this case both the variation of the cubic lattice parameter and the Arrhenius plots for conductivity revealed nonlinear behaviour that they ascribed to two fluorite structure changes¹. From a viewpoint of solid solution range, the PbO-doped Bi₂O₃ system had a narrower range for fcc phase stabilization than the Y₂O₃-doped Bi₂O₃ system. The XRD results confirm the literature finding.¹ Therefore, it is expected that the Y content should be larger than the Pb content needed to attain fcc phase in doubly doped bismuth oxide.

The first compositional series where $x = 0.02$ is referred to as 2Pb8YSB with 10 mol% total dopant concentration and a ratio of 1:4 between Pb and Y. The same naming system was adopted for other compositional series. After sample preparation, we then pressed pellets (of mass 0.7 g) for 15 minutes using isostatic pressing at 1.5 ton (750 MPa) into pellet disks of about 1 mm in thickness using a disk-shape 5 mm diameter die for EIS measurements.

The pellets were then sintered at various temperatures using a furnace which was programmed to start from ambient temperature to 400°C with a holding time of 4 hours and then ramp-up to 750°C for samples with low total dopant concentration (≤ 20 mol%) as they melt beyond 750°C while those with high total dopant concentration (≥ 20 mol%) were allowed to reach 800°C both with a holding time of 14 hours. The furnace then switched itself off and the samples were cooled in there (uncontrolled).

The samples were then distinguished by powder X-ray diffraction (PXRD) at room temperature after sintering at different temperatures to build an understanding of the phase behaviour of the materials. Variable temperature (VT)-PXRD was done as an in-situ method to see more accurately where the phase changes, as well as to determine thermal expansion coefficients. VT-Raman spectroscopy was used to build a better understanding of any possible amorphous phases not detected by PXRD. Differential thermal analysis (DTA) was used to gain insight into the initial thermal-dependent behaviour of the materials. VT-electrochemical impedance spectroscopy (EIS) was used to establish the temperature at which ionic conductivity is good enough for usage as an electrolyte in fuel cells.

2.2. Materials characterization

2.2.1. Powder X-ray Diffraction (PXRD)

The sample was ground to a fine powder to minimize inducing extra strain (surface energy) that can offset peak positions, and to randomize orientation. The sample was then placed onto the sample surface and smeared uniformly onto a glass slide, assuring a flat upper surface pack into a sample holder. Care was taken to create a flat upper surface and to achieve a random distribution of lattice orientations. The intensity of diffracted X-rays was continuously recorded as the sample and detector rotate through their respective angles. A peak in intensity occurs when the sample contains lattice planes with d-spacings appropriate to diffract X-rays at that value of θ .

The calcined powder lattice structure was identified through X-ray diffraction analysis using a Bruker D2 phaser in Bragg-Brentano configuration, equipped with a primary and secondary soller slits, secondary beam Fe K_{β} filter, sealed Co K_{α} radiation tube and Bruker Lynxeye PSD detector which was used to obtain scans for phase identification from the powders at room temperature.

To analyse phase changes as a function of temperature, variable temperature (VT)-PXRD was used. For this, a Bruker D8 advance was used in the Bragg-Brentano setup, fitted with a sealed Cu K_{α} radiation tube, secondary beam Ni K_{β} filter, Bruker VÅNTEC detector, and primary and secondary soller slits. Using an Anton Paar XRK900 reaction chamber, the samples were heated and cooled at a rate of 6 °C /min from 30 °C to 780 °C and back to 30 °C. In both heating and cooling cycles, scans were taken at 30°C intervals.

Higher resolution powder diffractograms of the powder materials were collected at beamline 28-ID-2 ($\lambda = 0.1671 \text{ \AA}$) at the National Synchrotron Light Source II (NSLS-II). Synchrotron X-rays are produced by large particle accelerators where magnetic lattices like insertion devices (undulators and wigglers) and bending magnets accelerate high-speed electrons (nearing the speed of light).¹ The design of detectors is a key factor as well. The “zero-background” Pilatus detector (Dectris) is currently commonly used. Based on the photoelectric effect, it recognises the electrical signal converted from the incoming X-ray photons.¹ While maintaining high sensitivity, the Pilatus

detector has a high dynamic range. It can even make studies down to a couple of microns with spatial resolution.

In contrast with laboratory analogues, synchrotron X-ray powder diffraction (SXRD) is considered to be excellent due to its special characteristics of synchrotron X-ray beams:²

- a) Higher brilliance (tight and intense collimation) means (i) smaller beam angular divergence (resulting with high-angular resolution data) and (ii) deep analysis of high-contrast structural information (high signal to noise ratio) for small-feature detection data.
- b) As a function of 2θ , horizontal polarization decreases the dropping of intensity.
- c) Tenable X-ray wavelength, i.e., it is possible to avoid the X-ray absorption problems of single atoms by decreasing sample fluorescence.
- d) A large instrument with various sample environments.
- e) Acquisition of fast data.

A precise and accurate refinement requires, based on the statistical sentiment, a larger number of experimental observables than refinement parameters. Severe peak overlap occurs due to incidental effects resulting from very near lattice parameters, therefore high-resolution diffraction data is important for high-quality structure refinement, particularly with synchrotron X-rays. All diffractograms were indexed using DIFFRAC.EVA V4.2 Bruker AXS linked to the crystallography open database (COD)³. Rietveld refinement of diffractograms was carried out using Bruker AXS TOPAS-Academic V.6.⁴

All refinements were carried out using the fundamental parameters approach as implemented by Cheary et al.⁵ The initial structural refinement models for the cubic fluorite phase was based on the δ -Bi₂O₃ structure.⁶⁻⁸ A cubic sub-cell model was used in the space group *Fm-3m* with Bi, Y and/or Pb on the ideal fluorite $4a$ (0,0,0) site and the O₂ atoms occupying the regular $8c$ and interstitial $32f$ (x,x,x) site. A total occupancy limit was applied during refinements, allowing refinement of occupancy between the $8c$ and $32f$ sites, with the total O²⁻ ion content being set at that of the stoichiometric formula.

2.2.2. Differential Thermal Analysis/Thermal Gravimetry Analysis (DTA/TGA)

Thermal analysis includes the measurements, as a function of temperature, of a solid's properties, making it a valuable technique for examining potential phase changes. Phase shift generates either heat evolution or absorption. In DTA, during a programmed temperature change, the temperature of an inert reference material is compared to that of a sample. Both chambers are heated in a furnace at a regulated uniform rate and the temperature of the two remains the same until the sample either takes in (endothermic) or gives out (exothermic) heat energy and when there is a thermal event.

The Simultaneous Thermal Analyzer, STA 6000 device was used to conduct experiments (PerkinElmer, USA). STA is a simultaneous method that calculates the weight change of a sample (TG) and as a function of temperature and/or time, measures the change in temperature between a sample and the reference (DTA). The high versatility of the differential analysis function (DTA, DSC) and the validated capabilities of thermogravimetric (TG) measurement technology are combined in the STA 6000 to provide highly accurate information on characterization. For high quality simultaneous TG and DTA/DSC measurements, the STA 6000 features the revolutionary SaTurnA Sensor.⁹

Built with the reference ring directly below the sample pan holder, this advanced sensor is optimized to achieve flat DTA baselines and high sensitivity. One can be confident of the integrity of the analysis since both the sample and the comparison are calculated simultaneously. The pure platinum pan holder and corrosion-resistant reference ring make the instrument ideal for a wide range of samples and applications. In ceramic pans, samples of approximately 10mg were inserted and the lid was placed over the sample. The experiments were carried out in an atmosphere of dry nitrogen (flow rate of 20 mL min⁻¹). The sample was heated in the air at 10 °C/min from 30 °C to 750 °C or 800 °C and then cooled down at the same rate to 30 °C.

2.2.3. Raman Spectroscopy (RS)

Measurement of the Raman spectroscopic data were obtained using a Horiba LabRAM HR Raman system fitted with an emission line 514, 532 nm argon-ion laser, a cooled Symphony CCD detector using liquid nitrogen and a grating of 600 lines/mm. For the in situ variable temperature measurements, an Olympud optical microscope attachment with a 50x LWD objective lens and a Linkham TS1500 sample stage were used. The sample phase was purged with high purity argon gas and the spectra were determined using a heating rate of 10 °C/min between room temperature and 700°C or 800 °C at 100 °C increments. The overall acquisition time was 2 minutes, and the samples were analysed using the power form, pf.

2.2.4. Rapid acquisition pair distribution function (RA-PDF) technique

The key concepts outlined in Chupas, *et al.*¹⁰ is the most common setup for a synchrotron experimental station or beamline for performing total scattering measurements for use with PDF analysis. The setup uses the readily available beams of high-energy photons at modern synchrotron sources. A flat 2D area detector which is located near to the sample is used in the RA-PDF setup. This positioning helps the detector to collect the scattering to achieve the required Q_{\max} at sufficiently high angles. In transmission geometry, also referred to as Debye-Scherrer geometry, the sample is set in place in the beam path and the experiments are conducted.

Usually, the detector is located concentric with the beam, such that the full extent of the Debye-Scherrer cones can be obtained for optimum statistics. A beam stop that is mounted on a thin pole in the centre of the detector blocks the direct beam. The beam stop position also determines the Q_{\min} as it blocks a portion of the direct dispersion opposite the x-ray beam of the incident. The accessible Q window is defined by the detector's location in relation to the sample.¹⁰ The range can be determined using the maximum angle of 2θ that reaches the detector's outer pixels:

$$\tan 2\theta = \frac{r}{sd} \quad \mathbf{2.1}$$

r is the distance from the middle of the beam on the detector to the outer pixel, and sd is the distance from the sample to the detector. The geometry of scattering is shown in Fig. 2.2. As a

trade-off for the high angular range needed for PDF data, RA-PDF measurement $\Delta\theta$ resolution is generally low. Since the detector is usually motorized, the $\Delta\theta$ resolution can be enhanced to allow measurements of high-resolution powder diffraction while reducing the Q_{\min} - Q_{\max} window.

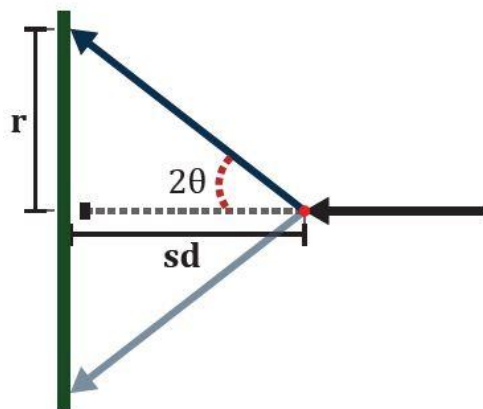


Fig. 2.2 Schematic representation of transmission geometry used on most typical RA-PDF beamlines.¹⁰

Total scattering measurements for this work were carried out at beamline 28-ID-2 (XPD) at the NSLS-II at Brookhaven National Laboratory. The beamline operates at wavelengths of 70 keV, in the hard X-ray range. When the detector is positioned in its closest proximity to the sample, about 170 mm, the high energy gives access to Q_{\max} between 25 – 30 \AA^{-1} . A large 2D Perkin Elmer amorphous silicon detector with a pixel size of 200 μm located orthogonally to the beam path was used, having an array of 2048 pixels. The detector is motorized, allowing it to be pushed back from the sample positions to distances of up to 1.5 m, enabling high-resolution powder diffraction measurements for $0.1 \text{\AA}^{-1} < Q_{\min}$.

Usually, the capillaries used are low scattering Kapton capillaries, alternatively quartz or borosilicate glass capillaries for more sensitive samples. The capillaries are placed on goniometer heads or fixed sample holders and can be rotated for powder averaging. Some beamlines also provide an option for using motorized sample changers to increase efficiency for multiple capillaries. Good quality measurements can be taken in a matter of several minutes at a standard

photon flux of a PDF beamline. The experimental stations are not limited to only capillary measurements and can be modified to fit exotic sample holders and environments with the aid of the beamline workers. Flow cells and advanced equipment regularly expand the setups.

2.2.5. Electrochemical Impedance Spectroscopy (EIS)

Using a Bio-Logic impedance analyser (MTZ-35) over the 10Hz- 1MHz frequency range with an AC voltage amplitude of 0.05 V, impedance measurements were carried out on the sample. It was equipped with an HF-1100 furnace and an HT-1100 sample holder. HTSH-1100 is a sample holder dedicated to electrical characterization across the temperature spectrum between room temperature and 1100 °C of solid materials. HTSH-1100 can also be used in controlled atmospheres for heat treatment. The HTF-1100 is a horizontal laboratory tube furnace dedicated to electrical material characterization and thermal treatment in the ambient temperature range up to 1100 °C.

Before impedance measurements, open- and short-circuit compensations were performed using MT-Lab¹¹ software to eliminate stray impedances caused by HTSH-1100 cell cables and sample holder. In MT-Lab¹¹ software, precise temperature stabilization mode was used to stabilize the sample temperature at each point of measurement.⁸ Upon temperature stabilization, an additional 30-minute soak period was set to guarantee a steady-state at each measurement point. Current shunt was set to Auto. This allows the equipment to determine the correct current range based on the actual current present in the cell. Impedance diagrams were collected ranging between 300 and 750 °C at 50 °C intervals using a heating/cooling rate of 10 °C/min.

The frequency range was from 10 Hz to 1 MHz with an A.C. amplitude of 10 mV. The PbYSB samples were sandwiched between HTSH-1100 platinum discs with a diameter of 12 mm. In the HTF-1100 furnace, the HTSH-1100 was mounted and connected to MTZ-35 by a two-terminal connection. MT- lab¹¹ software was used to control the furnace and sample temperatures using a heat-up rate of 10 °C/min. Two K-type thermocouples, integrated into HTSH-1100 and HTF-1100, measured both temperatures. Z Fit analysis tool accessible in MT-Lab¹¹ software was used

to evaluate the impedance data and to model equivalent electrical circuits. Upon determination of the electrical parameters using Z Fit, the ionic conductivities of the PbYSB samples in the air were calculated and plotted as a function of temperature.

2.3. X-ray diffraction technique

2.3.1. Introduction to diffraction

Diffraction methods are widely utilised to analyse crystal structure.¹² X-ray is a type of radiation that can be described as having wave-like behaviour. Waves are dispersed when they meet a barrier in their direction of propagation.¹³ Dispersed waves can interfere destructively or constructively, and this pattern of interference reflects the configuration of obstacles in space. In the case of a periodic structure in 3-dimension, where the wavelength of the radiation used is equal to the distance between obstacles, the positive interference of the scattered waves leads to the observation of diffraction. Periodically ordered solids are crystalline materials.

An atom or a group of atoms constitutes the fundamental repeating unit (unit cell) when it can be translationally repeated in all directions in a 3-dimensional system and this then generates the entire crystal.¹⁴ The unit cell of a crystal is characterized by three translations: a , b , and c , and three angles: β , α and γ (Fig. 2.3).¹⁵ Interatomic distances are of the order of 1-2 Å in crystals. Thus, in crystallographic experiments, radiation with similar wavelengths (~ 1 Å) such as neutrons, X-rays and electrons are frequently used.

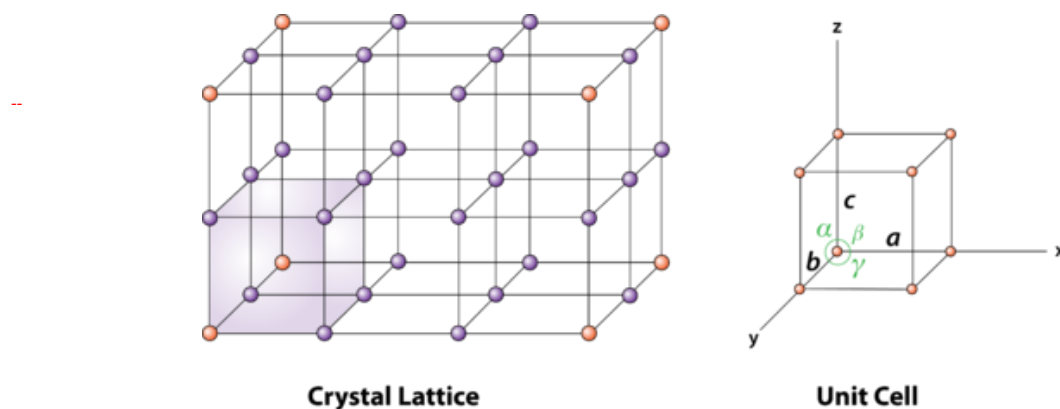


Fig. 2.3 crystal lattice (left) and unit cell (right) in three-dimensional space.¹²

Wilhelm Conrad Roentgen (1845-1923), a professor at Wuerzburg University in Germany, discovered X-rays in 1895.¹³ Working in his laboratory with a cathode-ray tube, Roentgen found on a table near his tube a fluorescent glow of crystals. A glass bulb with encapsulated positive and negative electrodes made up the tube that Roentgen was working with. The air in the tube was released, and the tube created a fluorescent glow when a high voltage was applied. With heavy black paper, Roentgen shielded the tube and noted a material located a few feet away gave off a green, fluorescent light.

Via experimentation, he discovered that most substances could go through the mysterious light but leave shadows of solid objects. He named them 'X' meaning 'unknown' rays, since he did not know what the rays were. Crystallographers had postulated that crystals are made of an ordered arrangement of atoms prior to Conrad Roentgen's discovery of X-rays in 1895 and inferred much about the ordered arrangement by determining the angles between crystal faces. With X-rays being discovered, crystallographers now had a valuable tool that allowed them to view “inside” the crystal and enable crystal structures and unit cell size to be determined in detail.¹³

Like all electromagnetic radiation, the energy of X-rays is inversely proportional to the wavelength, as indicated in the equation by Einstein:

$$E = h\nu = \frac{hc}{\lambda} \quad \mathbf{2.2}$$

where E represents energy, h is plank constant, ν is the frequency, c is velocity of light and λ is the wavelength. X-rays, having shorter wavelengths than visible light, have greater energy and can thus more readily penetrate matter. The level of penetration depends on the density of the substance. This has led to its widespread use as a medical tool.¹³

An example of an X-ray tube used to generate X-rays is depicted in Fig. 2.4. It has a tungsten filament cathode at one end and a metal target anode on the other side and is housed in an evacuated bulb. Current is passed through the cathode enabling it to emit electrons and with the large potential difference developed between the two electrodes (of the order of kV), electrons move toward the anode at high velocity.¹⁴

The inner shell electrons in the metal target are dislodged, resulting in the outer shell electrons moving to these vacated positions. The best way to picture this is to think of the basic Bohr model of the atom where the nucleus, comprising protons and neutrons, is surrounded by electron shells. The inner K-shell is then encircled by the M- and L-shells. Transitions thus occur from the M- and L-shells to the K-shell. Two types of X-ray spectra are generated as a result of these electronic transformations. The X-rays then pass through a window in the tube and they can be used according to their application.¹⁵

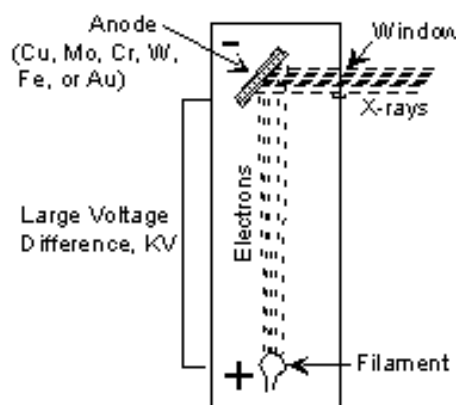


Fig. 2.4 X-ray tube depicting the production X-ray spectra.¹³

A continuous spectrum is generated as indicated in Fig. 2.5 that has a minimum wavelength. The intensity (in terms of counts/s) depends on the target material and the voltage applied. With an increase in voltage, the minimum wavelength decreases, and the amplitude increases.¹⁶

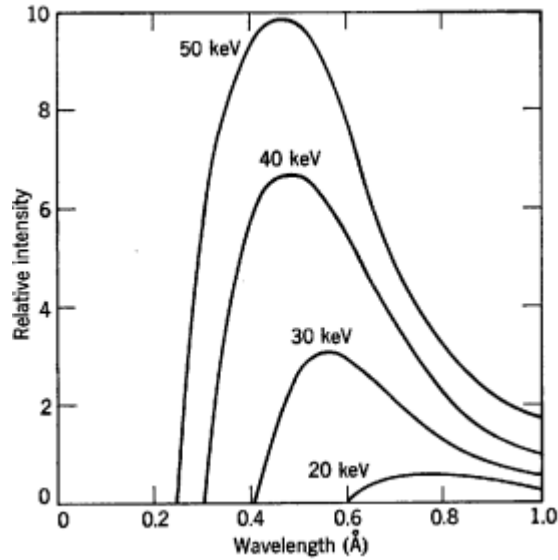


Fig. 2.5 The continuous X-ray spectrum emitted from tungsten target for four different values of eV , the incident electron energy.¹³

A second type of spectra, called the characteristic spectra, is formed at high voltage as shown in Fig. 2.6.¹³ Both K_{α} and K_{β} X-ray radiation are produced where the K_{α} radiation comes from the transfer of electrons from the L- to the K-shell, while the K_{β} radiation is from the M- to the K-shell transitions. These characteristic X-rays produce much larger intensities compare to the continuous spectra, and the intensity of $K_{\alpha} > K_{\beta}$. Thus, for different metal targets, these characteristic X-rays will have different wavelengths. A filter is often used to exclude the lower intensity K_{β} X-rays. Table 2.1 shows a range of commonly used metals and their corresponding X-ray wavelengths.¹⁶

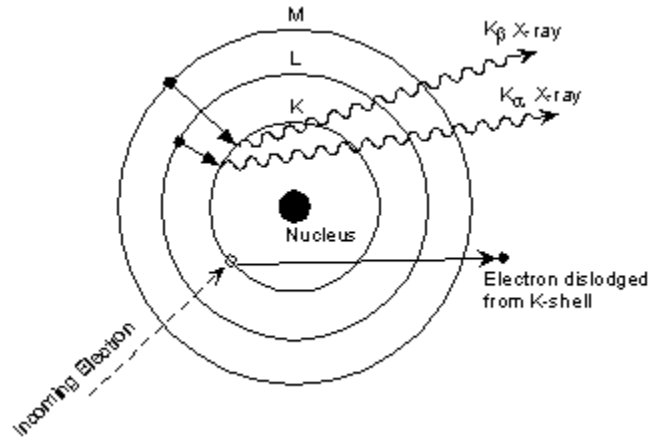


Fig. 2.6 An electron shell showing the production of $K\alpha$ and $K\beta$ when an electron is dislodged.¹³

The monochromatic X-ray beam generated in the X-ray tube is made up of a bundle of different waves which interact with each other. If the waves are in-phase they undergo constructive interference giving a resultant wave of higher amplitude. If the waves are out of phase, destructive interference will occur thus diminishing the amplitude of the resultant wave as demonstrated in Fig. 2.7. In a similar fashion, when the atoms in crystals interact with X-ray waves, the diffracted waves interact. Since the atoms are arranged periodically, the diffracted waves undergo both constructive and destructive interactions, where the former gives the reflections observed in a diffraction pattern.¹⁷

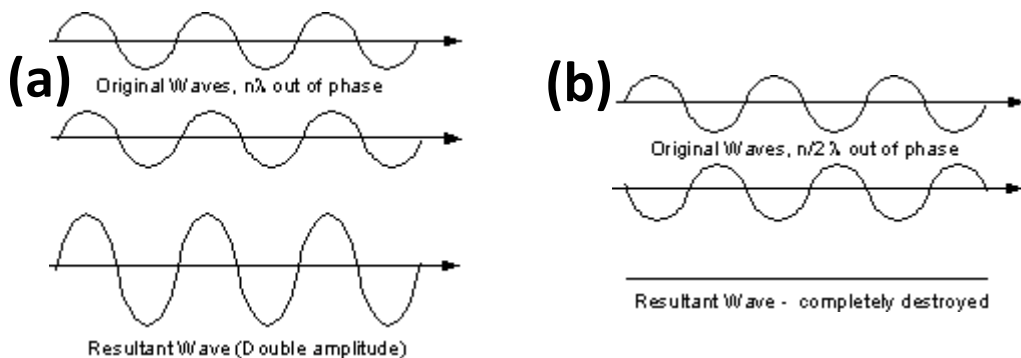


Fig. 2.7 Constructive (a) and destructive (b) interferences of X-ray monochromatic beam.¹³

Consider an X-ray beam entering a crystal and interacting with the atoms in their planes (with a spacing d between the planes) positioned at an angle θ to the incoming X-ray beam (Fig. 2.8) illustrates X-rays. Here Ray 1 reflects off the upper atomic plane at an angle $= \theta$. Similarly, for Ray 2 reflects off the atomic plane just below that. From the figure it can be seen that Ray 2 travels a longer distance (equivalent to $2a$) through the crystal. If the distance $2a = n\lambda$, where n is an integer and λ is the X-ray wavelength, then constructive interference will occur when the X-rays exit the crystal. However, if $2a$ is not equivalent to an integral number of wavelengths, there will be destructive interference.¹⁷

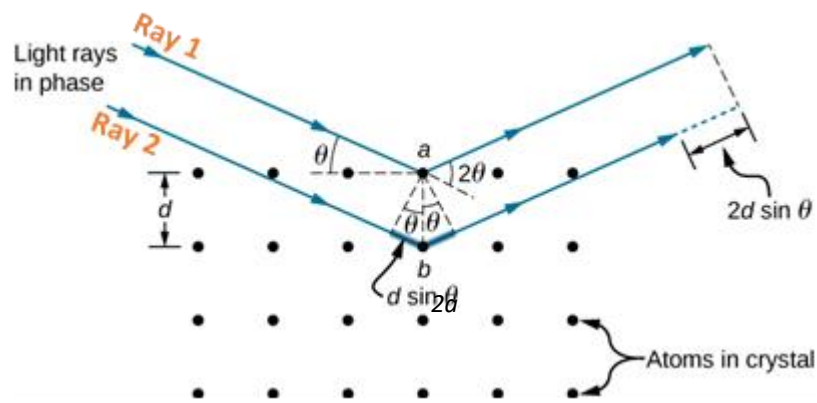


Fig. 2.8 Diffraction phenomena used to derive Bragg's law.¹⁷

Therefore, the condition for there to be constructive interference is

$$n\lambda = 2a \quad \mathbf{2.3}$$

But, from trigonometry, in terms of spacing, d , between the atomic planes, we can work out what the distance $2a$ is.

$$a = d \sin \theta \quad \mathbf{2.4}$$

$$\text{or } 2a = 2 d \sin \theta \quad \mathbf{2.5}$$

$$\text{thus, } n\lambda = 2d \sin \theta \quad \mathbf{2.6}$$

Equation 2.3 is known as Bragg's Law. It basically means that if we know the wavelength of the X-rays entering the crystal and can measure the angle of diffracted X-rays leaving the crystal, we can figure out how far apart the atomic planes are (referred to as d-spacing).

$$d = \frac{n\lambda}{2 \sin \theta} \quad 2.7$$

It is worth noting that this diffraction will only happen if the rays are in phase when they appear, and this will only happen if n (1, 2, 3, etc.) and θ values are both acceptable. In principle, the crystal could then be re-oriented to show another atomic plane, and the d-spacing between all atomic planes in the crystal could be measured, allowing us to calculate the unit cell size.¹⁶

Powder and single-crystal XRD, both of which have distinct advantages and disadvantages, are two different forms of X-ray diffraction. Although powder XRD has a much simpler preparation of the sample, structural data from a powder can be difficult to obtain because the sample molecules are randomly arranged in space; the signal-to-noise ratio is greatly diminished without the periodicity of a crystal lattice, and it becomes impossible to distinguish reflections from the various orientations of the molecule. The benefit of powder XRD is that it can be used to classify a known substance easily and reliably, or to check that two unknown samples are the same material.¹⁷

Single-crystal XRD is much more time-consuming and data-intensive, but it is important for structural determination of small molecules and solid-state macromolecules in many fields. Relatively small signals from individual reflections are magnified by constructive interference due to the periodicity inherent in crystals. This can be used to determine the precise spatial positions of atoms in molecules and can provide details about bond distances and conformation. The problem with single-crystal XRD is that it can be difficult to synthesize single crystals, and the instrument itself may be cost-prohibitive.¹⁶

The following is an example of common diffraction patterns for single-crystal and powder XRD (Fig. 2.9a and Fig. 2.9b, respectively). The dots correspond to Bragg reflections in the first picture and together form a single vision of the reciprocal space of the molecule. Random orientation of the crystals in powder XRD means reflections from all of them are seen at once, creating the

diffraction rings observed that correspond to unique vectors in the reciprocal lattice of the material.¹⁶

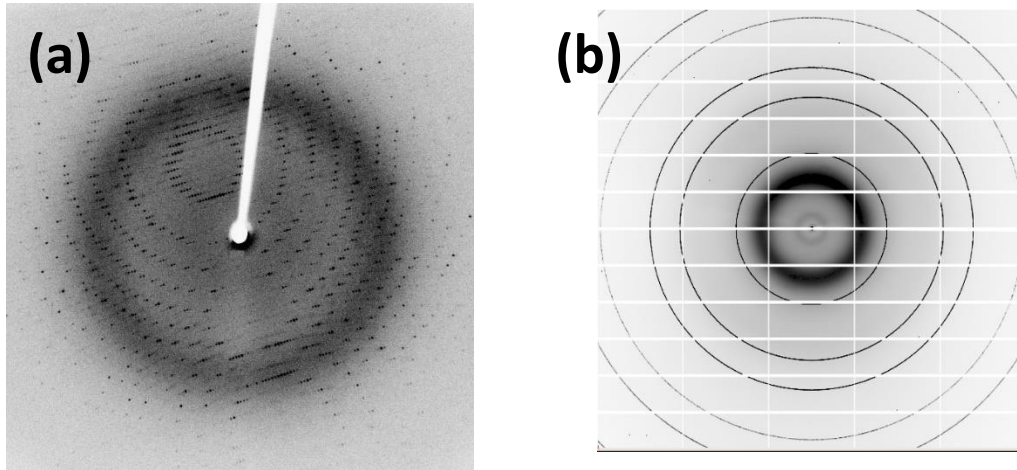


Fig. 2.9 Single-crystal diffraction pattern of an enzyme. The white rod protruding from the top is the beamstop (a). Powder X-ray diffraction spectrum of silicon (b).¹⁶

2.3.2. Powder X-ray diffraction (PXRD)

In practice, reorienting the crystal, calculating the angle, and deciding the d-spacing for all atomic planes will be a time-consuming process. A quicker approach is to use a technique known as the powder method. For this process, a mineral is finely ground to a powder, that contains grains with random orientations. Different atomic planes in some of the grains can be expected to lie parallel to the surface. Scanning through an angle of incident X-ray beams of 0 to 90°, enables angles where diffraction has occurred to be located, and these angles have a different atomic spacing.¹⁸

An X-ray powder diffractometer is the method used for doing this. It consists of an X-ray tube that can create a beam of monochromatic X-rays that can be rotated from 0 to 90°. A sample of powdered mineral is placed on a sample stage so that the X-ray tube can irradiate it. An electronic detector from the X-ray tube is mounted on the other side of the sample to detect the diffracted X-rays, and it is also allowed to rotate to create angles from 0 to 90° (Fig. 2.10) A goniometer is

referred to as the instrument used to rotate both the X-ray tube and the detector.¹⁶ The goniometer keeps track of the angle and transfers this information to a computer, whereas the detector tracks the rate of X-rays coming from the other side of the sample and sends this information to the computer (in units of counts/sec).¹⁸

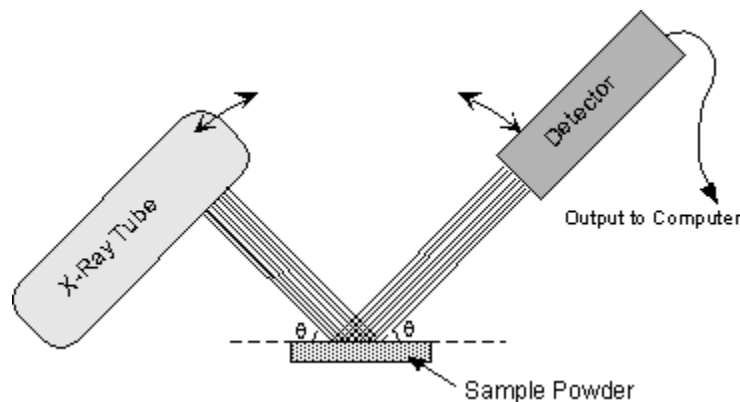


Fig. 2.10 Schematic representation of x-ray powder diffractometer.¹⁶

The angle (stated as 2θ) can be plotted against the X-ray intensity after a scan of the sample to construct a graph, as shown in Fig. 2.11. Using the Bragg equation, the angle 2θ can then be translated to d-spacing for each diffraction peak. The crystal structure can then be calculated using the Miller Index for that plane, and each of the diffraction peaks can be associated with a different atomic plane (hkl). You can acquire this data as a JCPDS Powder Diffraction Format.¹⁶

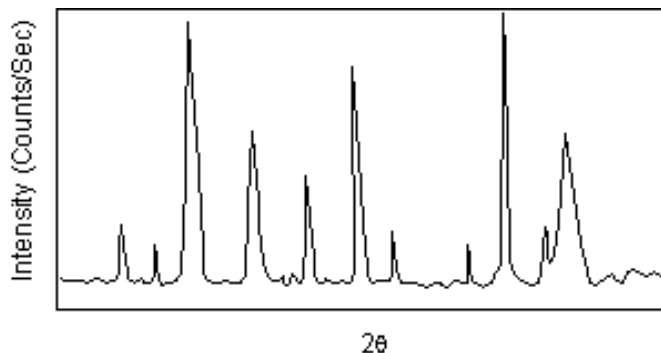


Fig. 2.11 Diffractogram of X-ray intensity plotted against the angle 2θ .¹⁶

2.3.2.1. Laboratory X-ray sources

Electromagnetic radiation with wavelengths in the estimated range of 0.1-5 Å (equivalent to an energy range of around 125 KeV-2.5KeV) is an X-ray used for diffraction experiments.¹⁷ X-rays are emitted at a sealed-tube source in a typical laboratory instrument (Fig. 2.12), where, inside a vacuum tube, electrons were accelerated by a potential difference of up to 60 kV to bombard a metal anode. The electrons cause a cascade of electronic transitions in the atoms of the target state.¹⁷

Via beryllium windows in the X-ray tube, divergent X-rays escape the tunnel. There is a power level of up to 3 kW in a standard tube.¹⁷ To spread the higher heat load over the target, higher power generators exploit rotating anodes. Such sources vary only in the intensity of the emitted radiation. Anode materials must have a suitably high melting point and be good conductors of both electricity and heat. Mo and Cu, with Fe, Cr, Co, W and Ag for specialist applications, are the most common target components.¹⁷

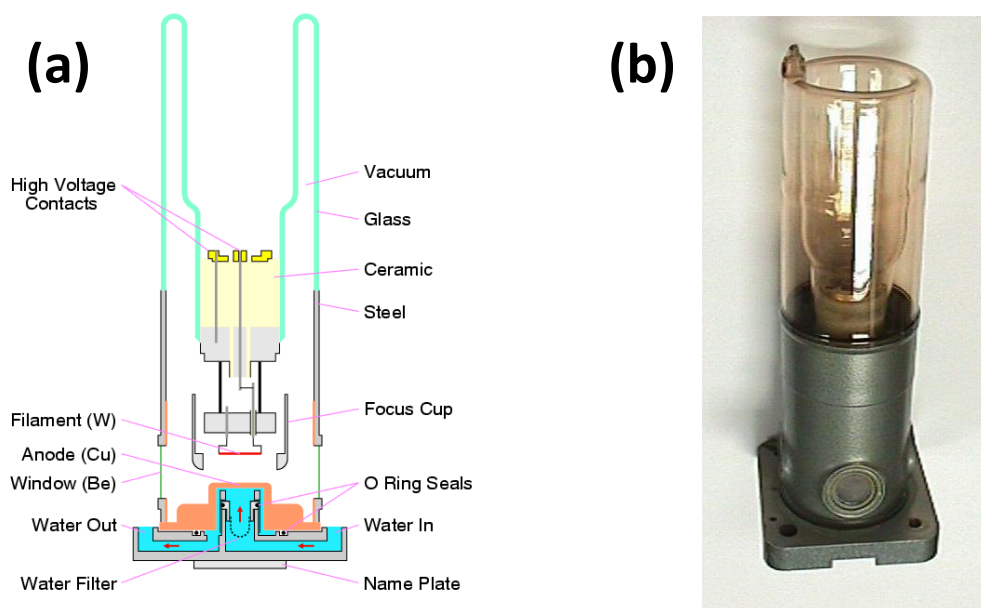


Fig. 2.12 A schematic diagram of a sealed X-ray laboratory tube with indicated main components (a) and a tube photograph (b).¹⁸

Fig. 2.13 shows a standard spectrum of X-ray emissions from a Cu anode. The electrons' loss of energy by collision with the atoms typically occurs via several events. The effect is the generation of a continuous X-ray spectrum referred to as white radiation.¹⁸ The maximum energy lost, $E(\max)$, defines the shortest wavelength, $\lambda(\min)$, which can be obtained as stated by the which can be obtained as stated by equation 2.2 ¹⁹ This equation is given a more practical form by:

$$\lambda = \frac{12.398}{V} \quad \mathbf{2.8}$$

Where λ is in \AA and V is in kV. Thus, the greater the X-ray generator's accelerating voltage, the smaller the minimum wavelength that can be achieved. The white radiation intensity peak occurs at a wavelength of approximately $1.5 \times \lambda(\min)$. Multiple-collision processes gain longer wavelengths. The cumulative strength of the white radiation, $I(w)$, is roughly proportional to the filament current, i , the anode target's atomic number, Z , and the accelerating voltage square, V .¹⁹

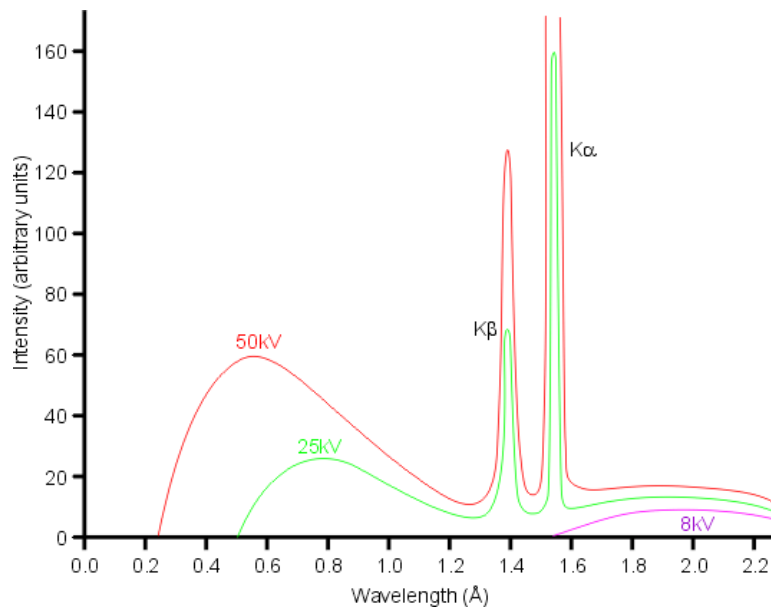


Fig. 2.13 X-ray spectrum generated from a Cu anode by different accelerating voltages. Until the voltage level reaches a critical value (about 8.5 kV for Cu), no radiation features are produced. The average operating voltage is approximately 4 times the critical voltage: higher voltage levels simply contribute to an increase in the "white" high-energy X-ray radiation intensity with a relatively small increase in the characteristic line intensity.¹⁸

A second type of spectrum is obtained when the energy of the accelerated electrons is greater than a definite threshold value (which rely on the metal anode) and is placed over the white radiation. The energy (and wavelength) of the peaks depends entirely on the metal used for the target and is caused by an electron being expelled from one of the metal atom's inner electron shells. This results in an electron falling to the vacancy level from a higher atomic level with the emission of an X-ray photon distinguished by the energy gap between the two levels. Fig. 2.14 displays the levels of electronic energy for a copper atom. Just two characteristic lines are seen at low energy resolution in the copper X-ray range. At higher resolution, however, the K alpha line is shown to be a doublet, whose components are labelled as K_{α_1} and K_{α_2} .¹⁹ There is very little splitting of the 2p orbitals in Cu (0.020 KeV) and the two wavelengths K_{α_1} (1.54056 Å) and K_{α_2} (1.54439 Å) are the same.¹⁹

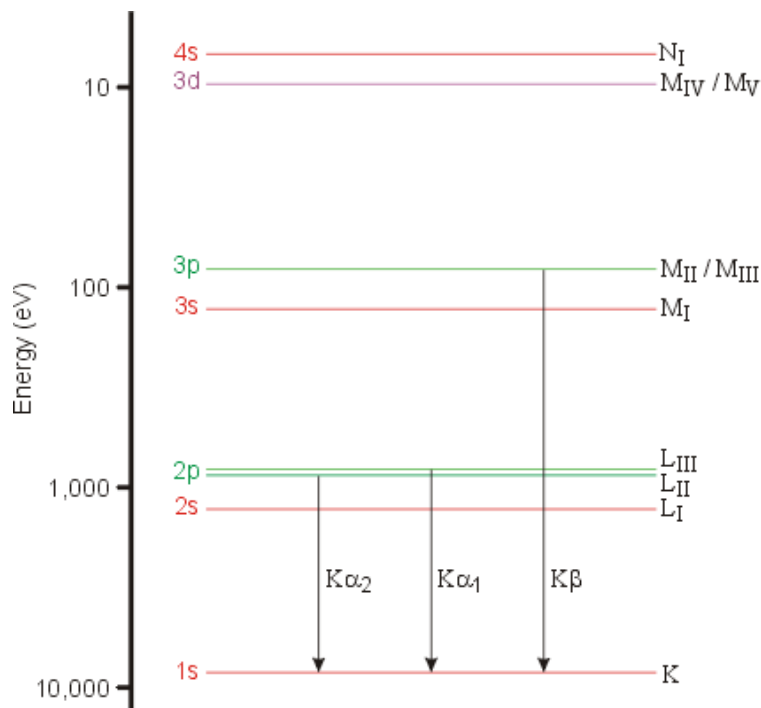


Fig. 2.14 Diagram of energy level for a neutral Cu atom. The features of the peaks shown in Fig. 2.6 emerge from the shown electronic transitions.²⁰

In fact, the above definition is a simplified version of reality since a high-resolution study of Cu K_{α} 's spectral lines shows that both alpha α_1 and α_2 peaks are clearly asymmetric.²¹ In implanting the so-called fundamental parameters approach to the profile fitting of powder diffraction data

peaks, in which the detailed spectrum of the incident X-rays must be known, an understanding of the origin of this asymmetry is important. In detailed investigations to describe the continuation of the X-ray spectrum, a combination of five Lorentzian functions is widely used to model the peak form of Cu K_α radiation.^{5,21}

For different anode targets, Table 2.1 lists the estimated wavelengths of the principal emission lines. For most practical use in the laboratory, the heavier elements offer wavelengths too short, although they are necessary for total scattering and PDF studies. In order to prevent fluorescence from samples containing elements excited by Cu radiation, longer wavelength sources are used, for example to research materials such as steels, Fe and Co tubes are preferred.²² Higher absorption by the sample, increased air scatter and less usable Bragg reflections are the drawbacks of such sources.²²

Table 2.1 Approximate theoretical emission lines for different anode targets.²²

Anode	$\lambda(K_\alpha)$ (Å)
<i>Cu</i>	1.5418
<i>Mo</i>	0.7107
<i>Cr</i>	2.2909
<i>Fe</i>	1.9373
<i>Co</i>	1.7902

In order to customize the features of the X-ray beam, different optical elements may be positioned in the beam direction. Diffraction (e.g. a monochromator) crystal, reflection (e.g. a mirror), or absorption (e.g. a filter or slits) may operate for these. To choose a specific wavelength, a monochromator is used, a mirror can concentrate the beam or block higher harmonics, and filters can be used to minimize unnecessary radiation.²¹

2.3.2.2. Filters

Two diffractometers, one with Cu and another with Co anode were used. Cobalt as an anode material (equipped in a Bruker D2 Phaser) is often used to investigate ferrous samples, the iron (Fe) fluorescence radiation would cause interference and cannot be eliminated by other measures. Copper (equipped in a Bruker D8 advance) is suitable for most diffraction examinations, and it is the most widely used anode material. Almost all diffractometers will have a method of monochromation to remove the K_{β} component, either a Ni filter on a Cu anode or Fe filter on Co anode.

By introducing a Ni filter (essentially a uniform thin sheet of nickel) in the beam direction, Cu K_{β} radiation can be greatly attenuated since the energy of the Cu K_{β} X-rays (with $\lambda = 1.392 \text{ \AA}$) is marginally above the threshold energy of Ni K absorption (with $\lambda = 1.488 \text{ \AA}$) resulting in K_{β} radiation being strongly absorbed.²⁰ On the other hand, K_{α} X-rays (with $\lambda = 1.542 \text{ \AA}$) have inadequate energy and are only modestly absorbed by this filter. The filter thickness must be optimised to allow a balance between reducing the intensity of the undesirable Cu K_{β} and decreasing the intensity of the desired Cu K_{α} .²⁰

2.3.2.3. Monochromator

X-ray filters have traditionally been used to minimize unwanted white radiation from an X-ray source and to remove (as much as possible) K radiation. The disadvantage of filters is that the background radiation is still high and that the transmitted radiation is still not very monochromatic. Single-crystal monochromators are an alternative and more selective way to produce a beam of radiation with a narrower wavelength distribution. In practice, "single crystals" are mosaics made up of several small crystal blocks that are roughly aligned in the same direction.²³ The so-called mosaic spread of the crystal is determined by the distribution of block alignment. The difference in the mosaic spread of the crystals can be used to differentiate two forms of monochromator. Pyrolytic graphite and silicon are two widely used materials for making wide band and narrow band ($\Delta\lambda / \lambda$) monochromators, respectively.²³

In comparison to silicon, where the mosaic blocks are almost perfectly aligned, the mosaic spread for pyrolytic graphite is relatively wide. The monochromator works by reflecting wavelengths that follow Bragg's Law for the monochromator's specific d spacings.²⁴ The highest d spacing, from

the (111) planes, for a silicon crystal (which is cubic with a unit cell size of 5.4309 Å) is 3.136 Å.²⁴ The Bragg equation ($\lambda = 2d \sin \theta$) indicates that the diffraction condition will be satisfied for $2\theta = 28.442^\circ$ for Cu $K\alpha_1$, but only $2\theta = 28.514^\circ$ for Cu $K\alpha_2$, resulting in a difference in Bragg angle of only 0.072° . As a result, only narrow band pass monochromator crystals, such as silicon, would be able to distinguish the $K\alpha_1$ and $K\alpha_2$ wavelengths from a laboratory copper X-ray source. Pyrolytic graphite monochromators, on the other hand, can pass all $K\alpha$ wavelengths but not $K\beta$ for which the Bragg angle is significantly different due to their wide band pass.²⁴

2.3.3. Synchrotron X-ray powder diffraction

2.3.3.1. Synchrotron X-ray sources

For conducting high-quality powder diffraction measurements, the use of synchrotron X-ray radiation has many advantages over laboratory sources. Synchrotron radiation is extremely intense and highly collimated, enabling instruments with a far higher 2θ resolution to be constructed. For a specific measurement, the wavelength may be optimized, such as operating at short wavelengths to infiltrate through absorbing samples or tuning to the absorption edge of an element in the sample to take advantage of anomalous scattering phenomena.²⁵

Synchrotron radiation is released when charged particles that travel at relativistic speeds modify velocity, such as when a magnetic field is forced to adopt a curved trajectory.²⁵ Dedicated devices (wigglers or undulators) are modern sources of synchrotron radiation, where electrons or positrons are accelerated to speeds similar to that of light and propagate in ultra-high vacuum tubes, driven by magnet arrays. The energy of an electron traveling at speed v is

$$E = m_e c^2 / \sqrt{1 - v^2/c^2} \quad \mathbf{2.9}$$

where m_e is the rest mass of the electron [$9.1093826(16) \times 10^{-31}$ kg] and c is the speed of light (299792458 m s⁻¹). The term $1/\sqrt{1 - v^2/c^2}$ is referred to as γ and is the factor by which, due to its relativistic speed, the mass of the electron increases from its resting mass.²⁵

The electrons are guided by magnetic fields in a storage ring. The storage ring consists of several sections, with a straight section followed by a curved section, and so on, with bending magnets used to steer the electrons through the curved sections (Fig. 2.15). In these curved sections, synchrotron radiation is produced, which can thus serve as the source of X-rays for experiments. The clusters of magnets in the straight section, typically referred to as insertion devices, can be placed to generate alternating magnetic fields that cause the electron path to oscillate. Each oscillation leads to synchrotron radiation emissions, and radiation can be optimized for several different applications by selecting the number, amplitude, frequency and direction of the oscillations.²⁶

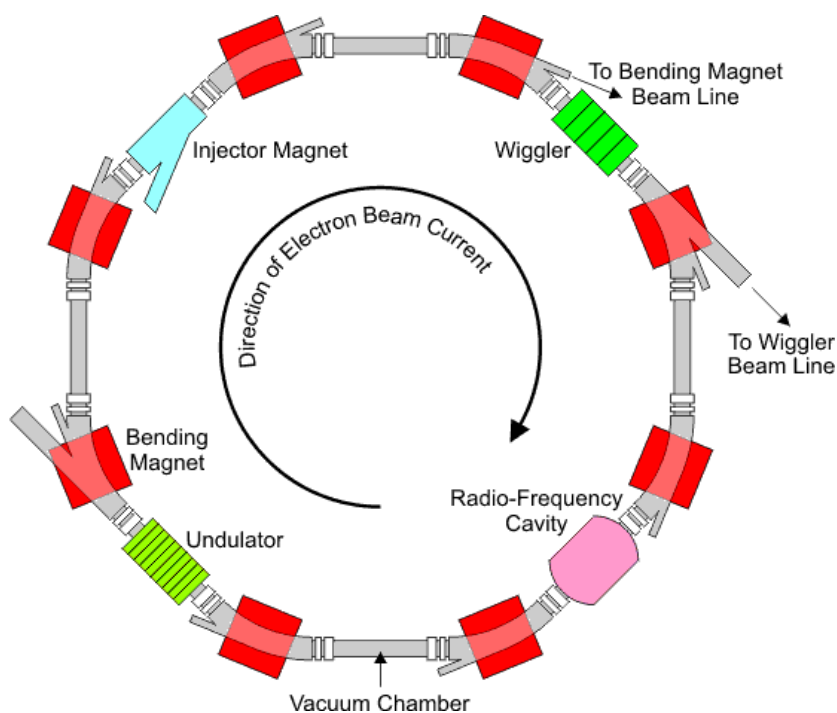


Fig. 2.15 Schematic of a synchrotron storage ring. Machines of the third generation have several straight segments and are optimized as X-ray sources by employing undulator and wiggler insertion systems.²⁶

The synchrotron X-ray sources of interest for powder diffraction are bending magnets, and the insertion devices are known as undulators and wigglers. These have their magnetic field in the vertical position that causes the electrons in the horizontal plane to deflect.²⁷ Consequently, with

the electrical component situated in the plane of the synchrotron orbit, radiation is linearly polarized. A thin cone of angular width $\sim 1/\gamma$ radians forms the radiation released by a single electron, contributing to the very high vertical collimation of the X-ray beam. Radiation is released tangentially in the entire bent segment for bending magnets, resulting in the emission of a broad tangential fan of X-rays (Fig. 2.16a).²⁷ This then reflects one of the great benefits of synchrotron radiation: that it is concentrated into a tiny angular fan, providing much greater strength and collimation than can be obtained from traditional laboratory sources.

The magnetic field varies sinusoidally for insertion devices and each electron oscillation induces tangential synchrotron radiation bursts. The oscillations are of relatively large amplitude for wigglers, and these add incoherently together, increasing the flux proportional to the number of magnetic periods (Fig. 2.16b).

The deflection of the electrons is relatively small for undulators and equivalent to the normal opening angle of the released $1/\gamma$ radiation.²⁷ In the horizontal plane, radiation from various oscillations interferes, and the beam is collimated.²⁷ Thus, unlike with a bending magnet or a wiggler where the radiation is spread out in a horizontal fan, for undulators the radiation is focused into a central on-axis cone surrounded by additional weaker rings (Fig 2.16c). Therefore, the flux density coming from a small sample of the central cone is very high. There are also some other interesting properties of this radiation: it is polarized horizontally in the plane of the electron orbit and polarized circularly above and below the orbit.²⁷ As seen in Fig. 2.17, while with laboratory sources the electric X-ray vector vibrates in all directions perpendicular to the X-ray propagation; this vibration is horizontally polarized with the synchrotron. This has benefits that can be used both in synchrotron diffraction and in spectroscopy.²⁷

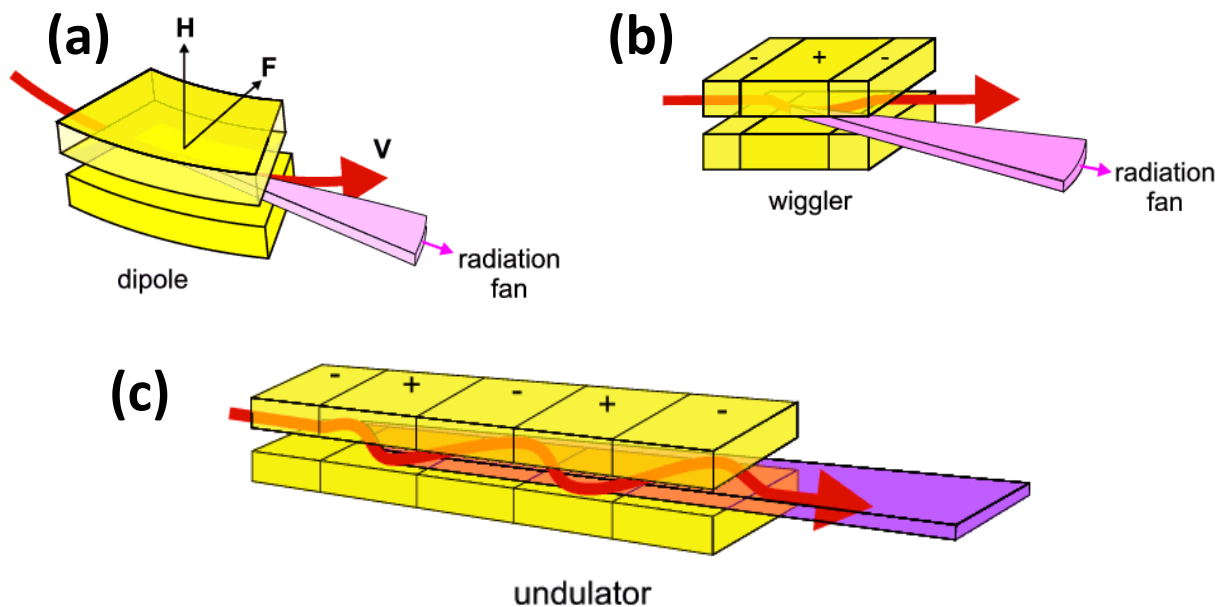


Fig. 2.16 Representations of (a) a bending magnet emitting a tangential radiation fan, (b) a fan of wiggler-emitted radiation and (c) an undulator emitted collimated beam.²⁷

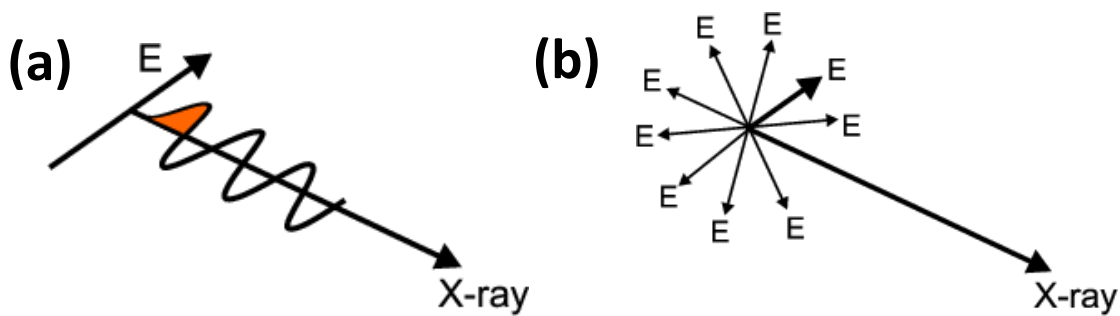


Fig. 2.17 Schematic representation of synchrotron radiation (a) and laboratory sources (b).²⁷

2.3.3.2. Filters

Attenuators such as aluminium, graphite or synthetic-diamond foils may be introduced into the primary beam path at synchrotron sources to minimize the heat load on the optical element thereby preventing X-ray detector saturation or to decrease the rate of radiation damage to the sample.²⁸

2.3.3.3. Monochromators

To select the wavelength from the polychromatic source, monochromators for synchrotron-based diffractometers are used. A double-crystal (“double-bounce”) structure is used to maintain the direction of the incident beam (Fig. 2.18); this can be either a crystal cut from a tube, or two crystals aligned separately.²⁹ Due to its very high degree of crystalline perfection, and its excellent thermal properties in the extreme synchrotron beam, Si is a common choice of crystal. A frequent option is the 111 reflections, but when higher energy resolution is needed, 220 and 311 are also used. To maintain a stable temperature for the crystal(s) under the heat load from the source, cooling is vital.²⁹

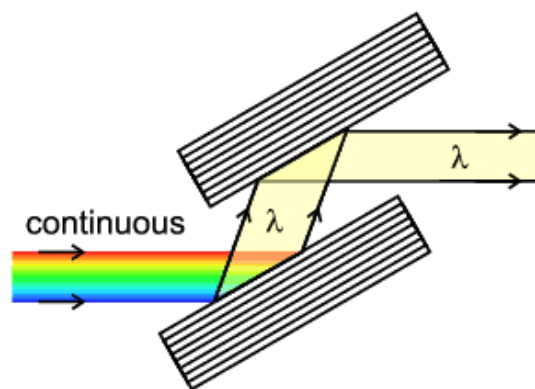


Fig. 2.18 Representation of a double-bounce monochromator used in synchrotrons. From the polychromatic source, the first crystal chooses a wavelength, which the second crystal reflects in the initial direction. For efficient transmission of the beam, the lattice planes of the latter have to be precisely aligned with the first crystal.²⁷

2.3.4. The Rietveld method

The Rietveld method is a structural refinement technique that requires modelling the entire diffraction profile.³⁰ The Rietveld refinement technique for powder-diffraction data is essentially a multiparameter curve-fitting procedure. The model function comprises a parameterized definition of a curve that is fitted using least squares to incorporate data points that comprise the powder-diffraction scan. The model function includes both the contribution from a smooth background that highlights the peaks and contributions from the crystalline component of the sample from the sharp Bragg peaks. The peak magnitudes are derived from parameters of the crystal structure (e.g. atom coordinates) and their shapes from parameterized functions which are a convolution of instrumental and microcrystalline broadening effects.³⁰

The model also involves parameterized illustrations of the numerous systematic effects (e.g. absorption) which change the intensity of the profile from that expected from an idealized experiment. Subsequently, the outcome of a Rietveld refinement involves information on the crystal structure (site fractions, lattice parameters, displacement factors and atomic coordinates) and macroscopic sample information (crystalline phase fractions, micro-strain distribution and crystallite size).³¹

In 1969 Hugo Rietveld proposed this approach to analyse complex diffraction patterns through a curve-fitting process.³² When calculating the intensity of a given point y_i in the diffraction profile (Eqn 2.9), the calculated structure factors along with the peak shape, background and instrumental parameters are used in the Rietveld method.

$$y_i(cal) = \sum_k I_k \Omega(2\theta_i, 2\theta_k) \quad \mathbf{2.10}$$

$\Omega(2\theta_i, 2\theta_k)$ is the function describing an individual profile and I_k is the integrated intensity for reflection k .³³ The least-squares refinement is performed in the Rietveld method until the best fit is obtained for the observed powder diffraction pattern. The least-squares refinement minimizes the difference between the observed and calculated profiles. Probably the best way to follow and direct a Rietveld refinement is looking at a differential profile plot. The fit of the calculated

pattern to the observed data can also be given numerically. Typically, this is achieved in terms of the indexes of agreement or the R-values. The weighted-profile R-value, R_{wp} , is defined as

$$R_{wp} = \left\{ \frac{\sum_i w_i [y_{i(obs)} - y_{i(cal)}]^2}{\sum_i w_i [y_{i(obs)}]^2} \right\}^{\frac{1}{2}} \quad \mathbf{2.11}$$

where $y_{i(cal)}$ is the calculated intensity at step i , $y_{i(obs)}$ the observed intensity, and w_i the weight. The numerator expression is the value that is reduced during a Rietveld refinement. If the background is subtracted, $y_{i(obs)}$ is the total intensity after-subtraction, but if the background is refined, $y_{i(obs)}$ and $y_{i(cal)}$ will incorporate the background input. In the latter case, a high background would necessarily produce a low R_{wp} value, since the background feature accounts for a large proportion of the intensity. Therefore, the comparison of profile R values from different kinds of powder diffraction experiments may be highly misleading. The final R_{wp} should ideally approach the statistically anticipated R-value, R_{exp} ,

$$R_{exp} = \left\{ \frac{(N - P)}{\sum_i^N w_i [y_{i(obs)}]^2} \right\}^{\frac{1}{2}} \quad \mathbf{2.12}$$

where P is the number of parameters and N the number of observations.³³ R_{exp} reflects the quality of the data (i.e. the counting statistics). Thus, the ratio between the two (goodness-of-fit) is given as:

$$\chi^2 = \frac{R_{wp}}{R_{exp}} \quad \mathbf{2.13}$$

which is also quoted quite often in the literature, and should approach 1.³³

2.4. Thermal Analysis

Thermogravimetry is a branch of thermal analysis that studies how a substance's weight changes as a function of time or temperature.³⁴ When the sample is exposed to a controlled heating or cooling environment, the weight change profile is recorded. The term "isothermal mode" refers to a weight change that is registered as a function of time. The weight change is registered as a function of temperature in scanning mode. The mass change for a sample can be analysed under

programmed conditions, which is the core concept of thermogravimetry analysis (TGA). As a result, TGA is primarily used to comprehend thermal events such as sublimation, adsorption, vaporization, desorption, absorption, decomposition, reduction and oxidation.³⁵

TGA may also be used to assess the number of volatile products lost during chemical reactions in polymer nanocomposites, nanomaterials, polymers, fabrics, coatings, films and paints. TGA may be used to study the kinetics of chemical reactions under different conditions in addition to predicting thermal stability for samples. It is critical to optimize the variables or conditions that influence the mass change for samples over the course of the experiment when investigating kinetics. The mass shift is influenced by many factors, including (i) the volume and weight of the sample taken for analysis, (ii) the physical form of the sample, (iii) the shape and nature of the sample holder, (iv) the nature of the environment under which the analysis is carried out, (v) the atmosphere pressure sustained in the sample chamber throughout the analysis, and (vi) the rate of heating or cooling conditions. Temperature levels are well known to cause changes in sample mass.³⁶

Advanced instruments for simultaneous determination of heat flow curves and TG are now available on the market. Perkin Elmer, for example, introduced the STA 6000³⁷ (used in this project), which use advanced analytical techniques to calculate the TG and heat flow curves simultaneously. Heat flow data is measured using differential scanning calorimetry (DSC) and weight loss data is measured using TGA on the STA 6000 instruments. The heat flow data from DSC is usually expressed in mW or J/g. The STA 6000 simultaneous thermal analyser instrument is designed with cutting-edge sensor technology to provide excellent accuracy and results. In addition, as compared to other simultaneous TGA-DSC analysers, the STA 6000 instrument includes a patent-pending “SaTurnA” sensor and a highly compact furnace, ensuring improved temperature regulation, accurate measurements, and faster cool-down timing.

DTA has been used in the present research to monitor possible solid-state reactions, but more likely phase changes in the samples during heating and cooling processes. Thermodynamics

dictates that any occurrences, such as diffusion and nucleation of the reacting material, growth of new crystal grains, change of state between solid and liquid, etc., are all correlated with changes in energy. Endothermic or exothermic peaks can be seen in a heat-flow versus temperature plot in these situations. DTA requires calculation of the temperature difference between a sample and an inert reference under the same heating regimes.³⁸

Fig. 2.19a displays the time shift in the furnace temperature, the reference and the sample. Fig. 2.19b displays the increase in temperature difference (ΔT) with the differential thermocouple observed with time. ΔT is referred to as the DTA signal. Substances which do not change in the temperature range of the measurement (usually α -alumina) are used as the reference.³⁸ The static-state signal is known as baseline. For instance, when the furnace temperature is increased and melting starts to occur in the sample, the sample temperature rise stops as shown in graph Fig. 2.19a. However, since both the furnace and reference temperature are still increasing, the ΔT changes reflecting an endothermic process as shown in graph Fig. 2.19b.³⁹

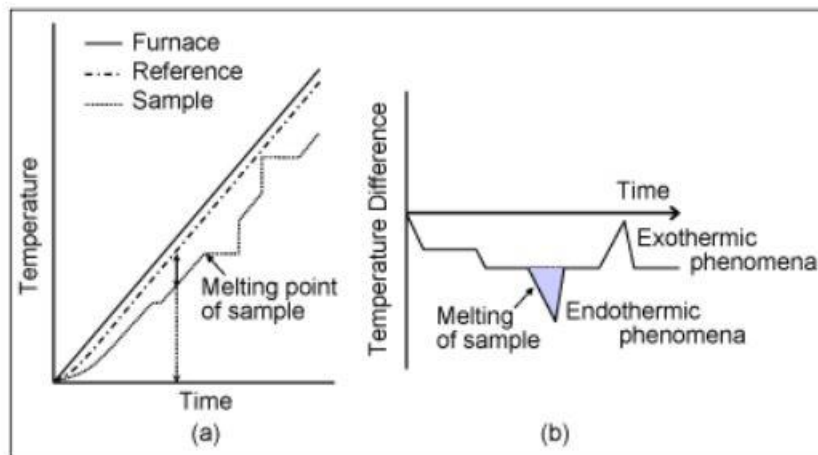


Fig. 2.19 Measurement principles of DTA.³⁶

2.5. Raman Spectroscopy

Spectroscopy is the study between the interaction of matter and light. There are many types of spectroscopy, each of which is named after either the light-matter interaction mechanism used or the light source used. Raman spectroscopy is based on inelastic light scattering in a substance, whereby incident light converts energy to molecular vibrations.⁴⁰ A Raman spectrometer can detect the scattered light, which reflects the substance's "chemical fingerprint." A substance can be classified or described using spectral information. A systematic approach for translating the Raman spectra of transition metal oxides was established by Hardcastle *et al.*⁴¹

This method treats each metal-oxygen bond in a molecular species or crystalline lattice as vibrationally independent of its surroundings, allowing for the development of a direct relationship between the Raman stretching frequencies and the lengths of the metal-oxygen bonds. This method clearly does not contribute to an examination of the vibrational mode as it ignores nearest-neighbour interactions and hence external modes and wagging/bending. This approach can't tell the difference between symmetric and antisymmetric stretching modes. This method is validated and can be used to test metal-oxygen bond lengths from Raman stretching frequencies within the limits of experimental error given by crystallographic bond length determinations.⁴²

Imposing two stages of approximation enables analysis of the Raman spectrum of a transitional metal oxide species in solid state.⁴³ Firstly, it is believed that the crystal's internal and external modes are independent of one another. The internal modes of metal oxide within the unit cell of a crystal occur in the medium and high frequency regions ($>200\text{ cm}^{-1}$ for bismuth oxide), while the external modes, including translation and vibrational modes, occur at lower frequencies ($<200\text{ cm}^{-1}$). Secondly, by assigning a high degree of symmetry to an atom or site within the unit cell, approximation of site-symmetry can be achieved.⁴³ Even though the site symmetry method predicts the Raman active modes from the crystal and the total number and types of infrared, a detailed understanding of crystal structure is needed before performing the above mentioned vibrational mode analysis.

The site symmetry approach enables direct comparison of the internal modes of a metal oxide restrained to a crystalline lattice in solution or gas phase with those of a similar molecule. Consequently, the approach to site symmetry forms the basis for the process of fingerprinting metal oxide. Nevertheless, the fingerprint method cannot be used reliably for metal oxides with distorted molecular geometries because of inconsistent spectral matches due to a nearly infinite number of potential geometric anomalies for a distorted species of metal oxide. Obviously, a systematic method for evaluating Raman spectra of metal oxide structures is needed, that do not depend on the subjectivity and ambiguity of the characteristic vibrational bands used in fingerprinting.⁴¹

In addition, the favoured systematic method would generally be applicable to enable it to provide extensive structural details for distorted metal oxide species as well as for typical symmetrical geometries. For many transition metal oxide systems including molybdenum⁴⁰, vanadium⁴¹, niobium⁴², tungsten⁴³, and titanium-oxygen⁴² bonds, metal-oxygen Raman stretching frequencies and metal-oxygen bond lengths were identified to have empirical relationships. This relationship was discovered to follow the same simple exponential sequence in each case:

$$\nu = A e^{BR} \quad \mathbf{2.14}$$

where B and A are fitting parameters, R is metal-oxygen bond length in angstroms and ν is Raman stretching frequency in wavenumbers. For this analysis, Eqn 2.14 was found to accurately describe the relationship between the Raman stretching frequencies and bond lengths of bismuth-oxygen bonds present in bismuth-oxide reference compounds. The Pauling bond strengths of metal-oxygen bonds are important for discussing the plausibility of proposed metal oxide structures in valence units, commonly known as bond orders or bond valences.⁴³ The differential distribution of accessible valence electrons over a group of metal oxide covalent bonds is represented by the Pauling bond strength.

In addition, the valence correlated with the metal cation is maintained by the valence sum rule, which enables the valence sum rule to be used as a bookkeeping device for the number of valence electrons in a structure. Brown and Wu⁴⁴ have established a generally applicable relationship which relates the valence of the metal-oxygen bond to its interatomic distance R . The empirical definition of a Bi-O bond length in angstroms explicitly refers to its bond power in valence units.

2.6. Pair distribution function and total scattering

Comprehension of the local atomic arrangement of materials is importance in order to understand their physical/chemical properties. These properties are generally dependent on the structural arrangement, including short- or middle-range interactions between atoms. This ordering can be expressed, in the case of crystals, by giving the atomic displacement parameters, unit cell dimension, the atomic positions and the symmetry of the space group for the small set of atoms constituting the asymmetric unit. An experiment conducted using X-rays, electrons, or neutrons would result with diffracted energy being absorbed into Bragg reflections regardless of the lattice periodicity.⁴⁵

The locations of these reflections characterize the symmetry of the unit cell dimensions and crystal structure. Their widths and shapes yield information about the sample microstructure, specifically in the event of powders and their intensities can be used to acquire the asymmetric unit atomic arrangement. The methods of crystallographic analysis at present are capable of building the foundation for our understanding of materials in various fields of chemistry, solid-state physics and biology, providing incomparable precision in the solution and refining of crystal structures.⁴⁵

However, not all substances are present as crystallised powders or single crystals, and crystallographers have had to establish original methods to obtain knowledge about the structural arrangements of liquid or amorphous materials. For nano-crystalline powders or for compounds where the local structure varies considerably from the typical structure that can be calculated by Bragg reflections measurements, an analysis of the pair distribution function (PDF) can be used. Data for PDF analysis is obtained experimentally in a way that is similar to a powder diffraction experiment as was discussed in section .⁴⁵

The waves emitted by each pair of atoms in the sample will interfere, and the sum of these signals over all pairs will produce the experimental diffraction pattern, which is then specifically linked to the atom distribution in direct space. For the general case there can be scattering at any angle of diffraction. The periodicity of the atomic arrangement for a crystalline material will lead to the presence of Bragg peaks where the scattered amplitude is concentrated. In several other cases,

examining the complete intensity distribution enables the collection of all information available on the atomic structure, i.e. the pair distribution.⁴⁶

In direct space this function is defined as describing the likelihood of finding a pair of atoms at a given interatomic distance r . Therefore, it can simply be calculated for any given sample atomic arrangement model. In order to compare the model's PDF, the experimental diffraction pattern needs to be transformed into direct space, essentially using a Fourier transformation. To provide sufficient quality experimental PDF to tackle complex structural problems, the diffraction pattern must satisfy criteria such as a sufficiently large Q_{\max} value (i.e. the maximum measurement value) and high statistics counting.⁴⁶

$$Q = 4 \pi \sin \frac{\theta}{\lambda} \quad \mathbf{2.15}$$

Such conditions have long restricted the use of PDF applications to the study of amorphous or liquids materials. At the same time, developing third generation synchrotrons yielding very high-energy X-ray beams and very strong intensities, enable PDF measurements to be carried out in a few seconds. PDF research is now being extended to a wide variety of fields from mineralogy⁴⁶ to solid state physics.⁴⁸

While PDF analysis is by no means in its infancy, experimental methods and new tools for data analysis and reduction are still in the early stages of development.^{49, 50} Both the Bragg and the diffuse scatter are considered in the development of a pair distribution function, which is why it is sometimes defined as a total scattering technique. The PDF provides the opportunity to explore the local structure and is defined as “the probability of finding two distance-separated atoms, r ”.⁵¹ This enables the PDF to provide details on the average, longer-range structure and the local structural disorder at the same time. The $G(r)$ PDF is defined as:

$$G(r) = \frac{1}{r} \sum_i \sum_j \left[\frac{b_i b_j}{\langle b \rangle^2} \delta(r - r_{ij}) \right] - 4\pi r \rho_0 \quad \mathbf{2.16}$$

where the sum is distributed around the atoms in the structural model, separated by the distance r_{ij} . b_i is the scattering power of the atom i (its X-ray or electron scattering factor); $\langle b \rangle$ is the sample's average scattering power; ρ_0 is the compound's numerical density, i.e. the number of

atoms per unit volume.⁵² This function will present peaks for values of r corresponding to the model's interatomic distance, the intensity of these peaks being proportional to the product of the atoms forming the pair's scattering factors. Within the PDF, all contributions from all pairs of atoms add up. However, partial PDFs can be calculated considering only the selected atoms.⁵²

The $G(r)$ can provide details at the fundamental level about how many atoms are located at a spherical distance (r) from any given atom (coordination number). It can provide details on any local disorder present in the system, and it is possible to quantify atom pair distances from the PDF pattern. Even if the sample structure is unclear, analysis can be done simply by directly obtaining atom-atom distances and coordination numbers from the PDF.⁵³ However, the introduced error is small enough in practice to remain valid for quantitative analysis of X-ray PDFs.

The PDF peak position is a reflection of the distance distribution in the material. For the case of a totally random distribution of atoms, the PDF will be flat and $G(r)$ would equal to 0 for any r . The second term in Eqn 2.16, $-4\pi r \rho_0$, is a normalisation term introduced to compensate for the numerical density ρ_0 increase in the number of atomic pairs. The regular (i.e. more than average) presence or absence of interatomic distances therefore appears as PDF fluctuations about zero.⁵⁴

In the case of short distances corresponding to near atomic neighbours, isolated peaks can be observed. In the case of structural disorder, the width of the peaks depends on the distribution of the distances around their average value, either due to thermal vibration or a statistical distribution.⁵⁴ For a crystalline solid, the interatomic distance distribution is determined by atom co-ordinates, atomic displacement parameters, and unit cell periodicity.⁵⁵ At each of these distances the PDF will produce a peak and the width of the peak being related to the relative atomic displacement parameters of the atoms forming the pair. The PDF should display these peaks in theory up to the largest interatomic distances in the crystal.

In the case of nanoparticles, the sets of coherently scattering atoms are confined to the volume of the individual particles and thus there will be no peak in the PDF beyond the maximum interatomic distance within the particles. Only randomly distributed interatomic distances between the atoms belonging to different particles will exist above this distance, and the

PDF will disappear due to the normalization term in Eqn 2.16.⁵⁵ Therefore, the PDF should provide a precise estimate of the particle size and the distribution of interatomic distances within the particles. With amorphous compounds the effect will be similar as the PDF will vanish with the disorder-induced loss of structural coherence. Simple observation of the PDF can easily deduce a particle size of $\sim 8-9 \text{ \AA}$; a model of atomic arrangement inside the particle can be checked and fitted to the data to provide a quantitative estimate of the interatomic distances and ultimately the structural arrangements.⁵⁵

$$G(r) = 4\pi r [\rho(r) - \rho_0] = \frac{2}{\pi} \int_0^{\infty} Q [S(Q) - 1] \sin(Qr) dQ \quad \mathbf{2.17}$$

where $\rho(r)$ is the microscopic pair density and $S(Q)$ is the total structure function, i.e. the normalized coherent scattered intensity. It is worth noting that the whole diffraction pattern is used to obtain $G(r)$, not only the Bragg peak intensities as for a classical crystallographic analysis.

The PDF, $G(r)$ is generated from the total scattering function $S(Q)$ through a sinus Fourier transform. From the normalized scattering intensity, $I(Q)$, the $S(Q)$ is generated and is defined as:

$$S(Q) = \frac{I(Q) - \sum c_i |f_i(Q)|^2}{|\sum c_i f_i(Q)|} + 1 \quad \mathbf{2.18}$$

The $I(Q)$ must be adjusted for a variety of factors, such as the variety of atoms in the sample and the experimental history, where c_i is the atomic concentration and $f_i(Q)$ is the atomic shape factor for type i atoms based on Q .⁵⁵ The PDF technique is very sensitive to background subtractions, particularly when the sample is weakly distributed compared to the background, as it is necessary to calculate the diffuse scattering. Usually, a background measurement requires an empty sample container placed in the same position in the experimental set-up, but further measurements might be required, such as only the beam without a container and the container with some fluid transmitting pressure.⁵⁶ This background is then removed from the data obtained on a sample such that the final measured scatter preserves diffuse scatter solely from the sample material. Therefore, the extent of the disorder, defects and so on, which contribute to the pattern through diffuse scattering outside of the Bragg peaks, will be included in $G(r)$.

In theory, a compound's PDF, which can act as a kind of fingerprint, can therefore be used to classify it, as shown in the case of pharmaceutical materials.^{56,57} It can be used to assess the length of structural coherence or the size of nanoparticles. Since the entire PDF is the sum of the PDFs of the individual phases weighted by their proportions within the mixture, it can be used for quantification regardless of whether the phases are crystalline or amorphous.

2.6.1. Termination Errors

The Fourier transform includes data from $Q = 0$ to $\infty \text{ \AA}^{-1}$, but experimental limitations imply that this data range cannot be accessed.⁵⁶ This influences the PDFs generated from the total scattering pattern. Consequently, in our experiments, it is necessary to understand the range from Q_{min} to Q_{max} that is being accessed and what effect these data ranges can have on our calculated PDFs.

2.6.1.1. Q_{max}

For obvious reasons $Q_{max} = \infty$ cannot be accessed experimentally, however, high-quality PDFs can be generated if the value of Q_{max} is sufficiently high. Accurate data analysis can be performed on $Q_{max} \geq 20 \text{ \AA}^{-1}$ generated PDFs and this is theoretically a conservative estimation, with the publishing of PDFs using $Q_{max} \leq 20 \text{ \AA}^{-1}$. Data from finite Q_{max} results in termination ripples at low r , which decrease as r increases in magnitude (Fig. 2.20). With lower Q_{max} values, these ripples are worse and can add to the pattern at low r , making it important to ensure that this effect is as small as possible, particularly when the atom-atom distances are short.

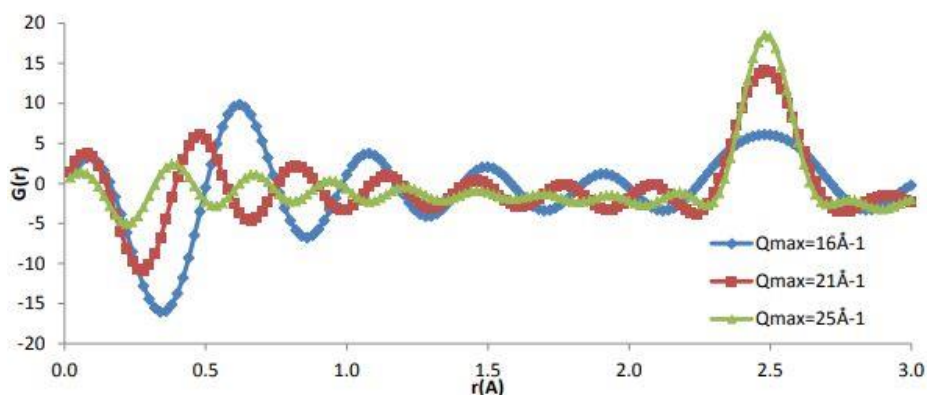


Fig. 2.20 Ni X-ray PDF gathered in a capillary generated using varying Q_{max} values.⁵⁶

On the other hand, if the counting statistics become too low, the use of very high Q_{max} values may also introduce noise into the PDF.⁵⁶ For this purpose, the entire Q range obtained does not need to be used, thereby ensuring that statistical errors are not included in the PDF. The $S(Q)$ can be tested in practice to investigate at what point the scattering from the sample is lost in the noise from the detectors and different Q_{max} values can be used to generate the highest possible PDF output (Fig. 2.21).

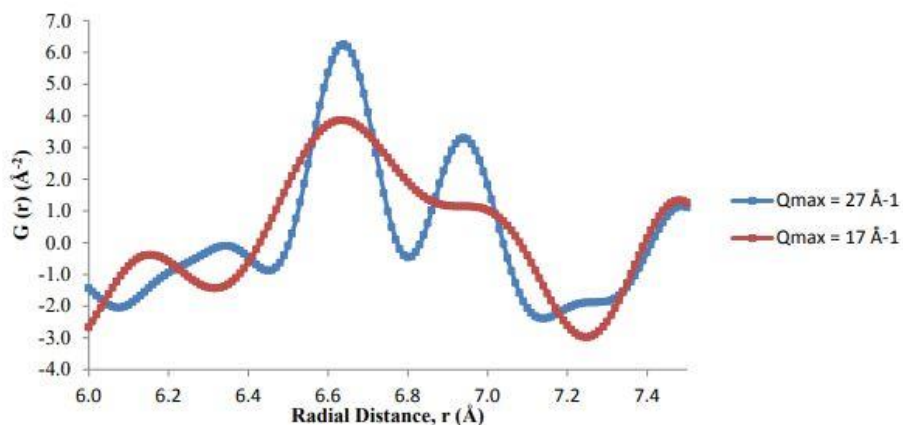


Fig. 2.21 Comparison of X-ray PDF patterns for BaTiO₃ using various Q_{max} values.⁵⁶

The Q_{max} value used for the Fourier transform would also determine the PDF's true space resolution. The greater the Q_{max} value, the higher the resolution in the PDF file (Fig. 2.21). Higher peak resolutions, particularly when considering subtle changes in overlapping peaks, are clearly advantageous for PDF analysis.⁵⁷

2.6.1.2. Q_{min}

Experimental factors would result in the inability to calculate the dispersion of the sample down to $Q = 0 \text{ \AA}^{-1}$. A beam stop, for example, prevents the beam from directly reaching the detector in X-ray diffraction tests, but then the beam stop also blocks the dispersion at very low Q values. This will introduce errors in the PDF (shortest atom-atom distance) at the first peak.⁵⁷ If $Q_{min} > 0 \text{ \AA}^{-1}$, then termination errors are introduced that lead to overestimation of coordination numbers along with termination errors introduced by $Q_{max} < \infty$. Extrapolating data to

$Q_{min} = 0$ is feasible in the absence of experimental data at low Q , thereby minimizing termination errors (Fig. 2.22).

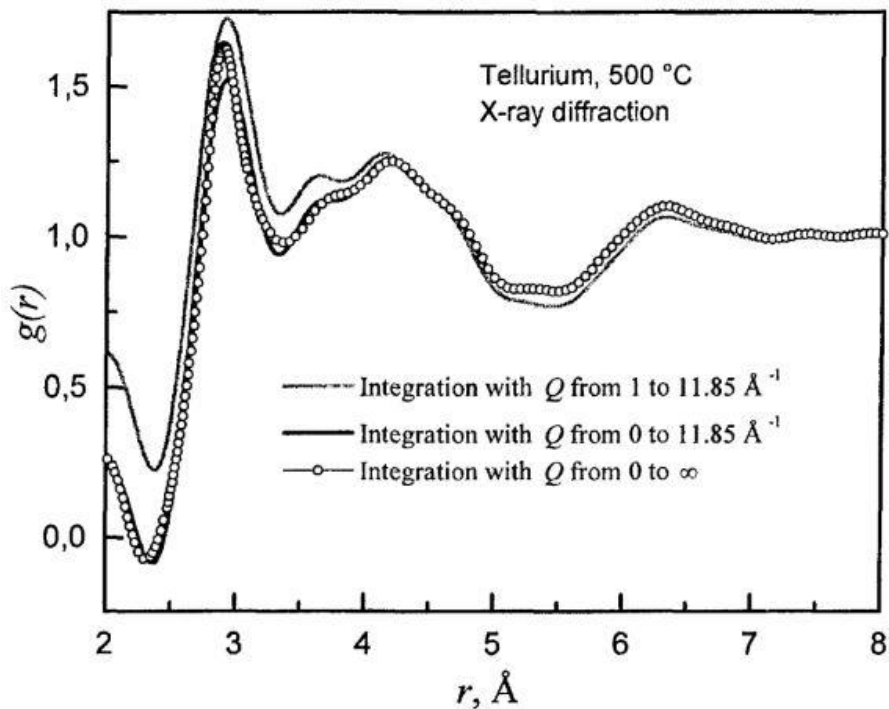


Fig. 2.22 Calculated $G(r)$ values of liquid Te using various integration limits.⁵⁸

2.6.2. Modelling of PDF

The key function of the PDF is, through the distribution of interatomic distances, to provide a description of the structure of a compound in a range of scales, ranging from local order ($< 10\text{Å}$ as local order) to average structure (a few tens of nm). It then constitutes a true method for examining multi-scale structures and will be fruitfully applicable in cases where these local and average structures differ, either because of the coherent domain/grain size (nano-crystalline and amorphous compounds) or because of localized defects or structural disorders (static and dynamic) that traditional crystallographic approaches cannot effectively take into account.

We have seen that from total scattering measurements, the PDF can be obtained experimentally and can also be calculated provided some kind of atom distribution is given. As always, it is

important to look for the configuration that produces the best agreement between the calculated and observed PDF in order to validate and develop the structural model. In order to model the PDF, two main types of methods are used.

The first approach is focused on Reverse Monte Carlo style numerical minimization techniques (e.g. when using the program RMCPProfile).⁵⁶ The structural model is constructed by distributing atoms in a (large) box more or less randomly, and is optimized using a Reverse Monte Carlo algorithm to minimize the difference between the calculated and measured PDFs.⁵⁷ Consequently, as the size of the problem increases and its likelihood of success is highly dependent on the selection of the physico-chemical constraints applied to the model (distance/angle limits, coordination imposed, bond valence sum), it requires large computational resources. It needs dedicated computers to analyse the resulting structure statistically. This approach is especially well suited to compounds and liquids that are amorphous or almost amorphous.

The second approach consists of the refining of the experimental PDF with a periodic structural model in the least squares profile, a kind of Rietveld refining in direct space (e.g. when employing the program PDFGui⁵⁷). This technique is quicker and better suited to substances that are close to a crystalline state. To compare local and average structure, symmetry constraints can be placed on all or part of the structure and refinements can be applied to different ranges of distances.

2.7. Electrochemical Impedance Spectroscopy (EIS)

Impedance spectroscopy (IS) is a tool for testing many of the material's electrical properties and interfaces, comprising of ionic, mixed and semiconducting electronic-ionic materials. Measurements are usually made with a cylindrical pellet or rectangular block for solid specimens to characterize the conducting action of solid electrolyte or electrode materials. In a typical two-probe experiment, two identical electrodes are applied to the sample's parallel sides. Depending on the requirements, measurements can be conducted under vacuum or in different atmospheres over large temperature ranges.⁵⁹

EIS is an effective linear electrochemical AC perturbation technique that is used in complex fuel cell processes to investigate failure modes, reaction pathways and degradation mechanisms.^{60,61} In certain cases, it also helps to investigate the properties of the electrolytes of the materials. The primary function it serves is to differentiate and distinguish the various processes such as that exist in different timescales. EIS is used in fuel cell research to identify the ohmic, concentration and activation polarization contributions.⁶⁰ In order to access these various processes, measurements are made within a range of frequencies. Here we will look specifically at the application of EIS to investigate a possible electrolyte for a SOFC and how to analyze the data.

Generally, EIS data in the form of a Nyquist plot is analyzed quantitatively using equivalent circuit modelling (ECM).⁶⁰ ECM involves building electrical circuits by using circuit elements (such as resistor, capacitors and so on) placed either in parallel and/or series to model the actual behaviour encountered on electrochemical systems in EIS data. The method consists of proposing a physically relevant circuit on which the model is built and fitting data using complex non-linear squares (CNLS), combined with a stochastic error structure assessment, to make it a consistent and provide a valid simulation process.⁶⁰

The overall approach to A.C. Impedance spectroscopy is to examine the response to an alternating voltage by impedance (complex resistance) measurement.³⁵ Normally it involves the implementation in the frequency domain of a variety of single-frequency voltages and impedance measurements. Measurements are usually performed over a wide frequency range, which was 1 Hz to 1 MHz in the present work. Electrochemical impedance is usually done by applying an AC potential in the form of a sine wave to an electrochemical cell and then measuring the current through the cell, especially for systems with higher resistances.⁶¹

An AC current signal is the response to this potential. It is possible to evaluate this current signal as a sum of sinusoidal functions (a Fourier series). Normally, electrochemical impedance is measured using a small signal of excitation. This is done in such a way that the cell's response is pseudo-linear. A sinusoid with the same frequency but shifted in phase will be the current

response to a sinusoidal potential in a linear (or pseudo-linear) system (see Fig. 2.23).⁶¹ The signal of excitation when expressed as a function of time, has the form:

$$E_t = E_0 \sin(\omega t) \quad \mathbf{2.19}$$

where E_0 is the amplitude of the signal, E_t is the potential at time t , and ω is the radial frequency. The relation between the radial frequency ω (expressed in radians/second) and frequency f (expressed in hertz) is:

$$\omega = 2\pi f \quad \mathbf{2.20}$$

The response signal, I_t , is shifted in phase ($\omega t + \phi$) in a linear system and has a different amplitude than I_0 .

$$I_t = I_0 \sin(\omega t + \phi) \quad \mathbf{2.21}$$

An equation similar to Ohm's law enables one to measure the system impedance as:³⁵

$$Z = \frac{E_t}{I_t} = \frac{E_0 \sin(\omega t)}{I_0 \sin(\omega t + \phi)} = Z_0 \frac{\sin(\omega t)}{\sin(\omega t + \phi)} \quad \mathbf{2.22}$$

As a result, the impedance is expressed as a magnitude, Z_0 (surge impedance), and a phase shift, ϕ as shown in Fig. 2.23.

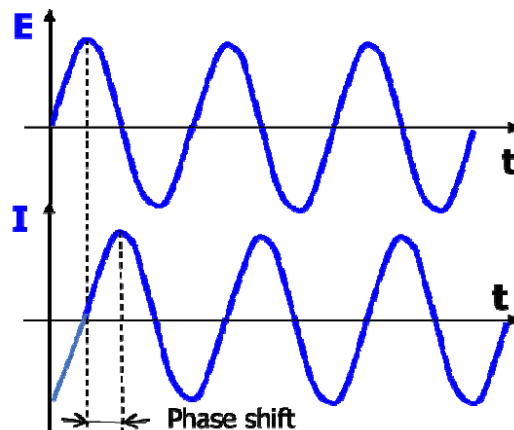


Fig. 2.23 Sinusoidal excitation signal (applied) and linear response signal (measured).⁶¹

For the plot, the applied E_t in the form of a sine wave on the X-axis and the sinusoidal response signal I_t on the Y-axis, an oval shape is produced in response called a "Lissajous Figure" (Fig 2.24). Before modern-day EIS instrumentation, oscilloscopes were used and these produced Lissajous figures. At that stage it was the method by which impedance measurements were done.⁶¹

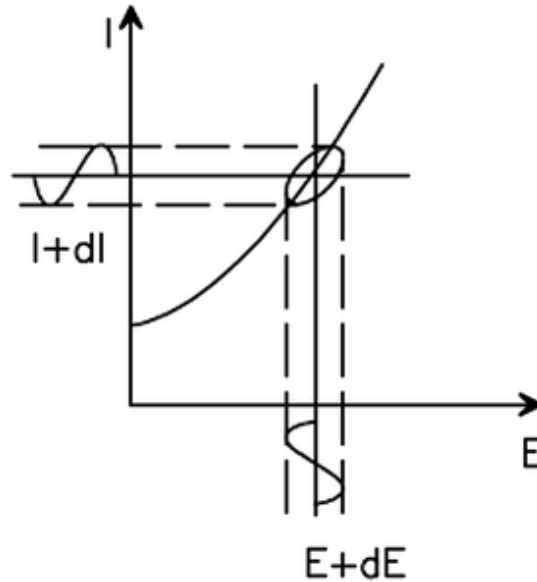


Fig. 2.24 A diagram during EIS experiments, the observed pseudo linear spectrum was depicted by a polarization curve. The origin of Lissajous diagrams is also visible in the observed field.⁶¹

With Eulers relationship,

$$\exp(j\phi) = \cos \phi + j \sin \phi \quad \mathbf{2.23}$$

Impedance can also be expressed as a complex function. The potential is defined as,

$$E_t = E_0 \exp(j\omega t) \quad \mathbf{2.24}$$

and the current response as,

$$I_t = I_0 \exp(j\omega t - \phi) \quad \mathbf{2.25}$$

Thereafter, the impedance is expressed as a complex number,

$$Z(\omega) = \frac{E}{I} = Z_0 \exp(j\phi) = Z_0 (\cos \phi + j \sin \phi) \quad \mathbf{2.26}$$

The term for $Z(\omega)$ is comprised of a real and an imaginary component.⁶² When the real component is plotted on the X-axis and the imaginary component is plotted on the Y-axis of a graph, a "Nyquist Plot" (Fig. 2.25) is obtained. The Y-axis is generally plotted as the negative of the imaginary impedance, and each point in the Nyquist Plot represents the impedance at a given frequency. The low frequency data occurs on the right side and higher frequencies are on the left side of the plot. An alternative way to look at this is to interpret the impedance as a vector (arrow) of length $|Z|$ and the angle between X-axis and the vector is commonly referred to as the phase angle.⁶²

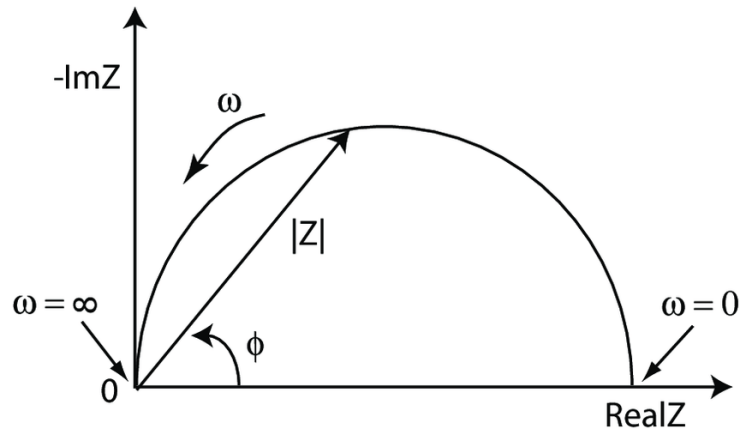


Fig. 2.25 Impedance vector Nyquist plot.⁶¹

There is one major flaw in the Nyquist Plot. You cannot tell what frequency was used to record each data point on the plot by looking at it. In Fig. 2.25, the Nyquist Plot results from Fig. 2.26's electrical circuit. A single 'time constant' is typical of the semicircle. Several semicircles may make up a full Nyquist Plot and at times just a part of a semicircle is often seen.⁶²

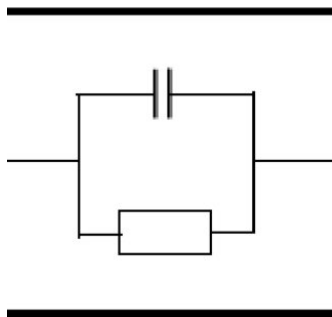


Fig. 2.26 With a single time constant, a simple equivalent circuit is created.⁶¹

Three key factors to remember when measuring EIS data to allow the models to apply are.⁶⁰⁻⁶³

(i) stability-where the current response contains no or minimal drift or background noise, (ii) linearity – where to have a linear output the input amplitude should be small, (iii) causality-where the current response is triggered only by the potential disturbance. It is also necessary to test for the validity of the data obtained to ensure the above three conditions were met when measuring an impedance plot, and before applying circuit modelling. Then, the data can be considered reliable and valid. The Kramers Kronig (K-K) transform is a relationship established by which the quality and validity of the data can be checked.^{59,60}

This is done by integrating the imaginary part of the data to obtain the real part of the impedance data, or vice versa. It is fair to say that the K-K transform relations would hold for any EIS data if the above three conditions are met. However, if the real part is not produced when processing the imaginary part, or vice versa, it means the data is not valid and any further analysis of this data (for example by using ECM) will not provide the correct information. As a result, using K-K evaluation of impedance data is a useful tool to ensure valid data was collected before even trying to assess the models which would apply to the data.⁶⁰

2.7.1. Equivalent Circuit Modelling (ECM)

ECM, as previously mentioned, provides both qualitative and quantitative insight into impedance data, allowing for a better understanding of electrochemical processes and their behaviour.⁶⁰ In

this sense, ECM can be used after proper validation of the EIS data to associate physically meaningful parameters with the system impedance. Therefore, ECM offers enough information on process parameters such as reaction rate constant and diffusion coefficient, etc. In short, it gives an empirical meaning to EIS information for process investigation. The circuit models are designed using three primary elements: inductors (L), capacitors (C), and ideal resistors (R). To account for non-ideal behaviour of real-world systems, specialized circuit elements are also used, namely the Gerischer element (Ge), the Warburg element (W), the constant phase element (CPE), etc.⁶³ These circuit elements are discussed in more details below.

2.7.1.1. Resistors

The symbol shown in Fig. 2.27a represents a perfect resistor element (R). A resistor's impedance is frequency independent and has no imaginary part. The current remains in phase through a resistor with the voltage across the resistor ($\phi = 0$). Therefore, it can be associated with Ohm's law, $Z_R = E/I = R$, where R is the resistance.⁶³ The Nyquist plot for a resistor is simply a single point on the x-axis that will give the same value irrespective of the frequency, implying that it has just a real impedance value (Fig. 2.27b).

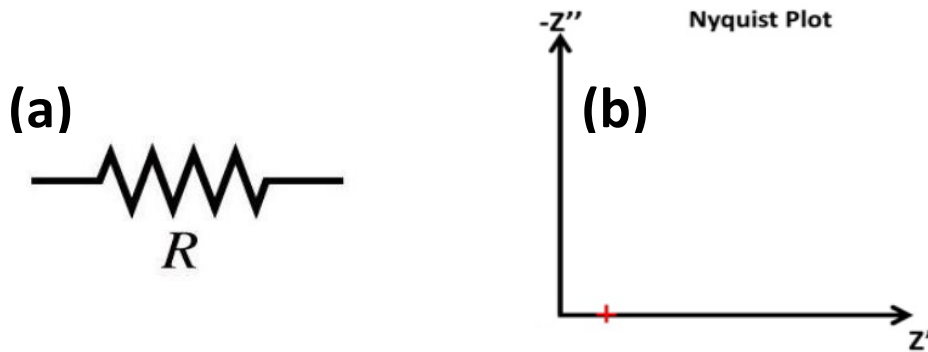


Fig. 2.27 (a) Representation of a perfect resistor in a circuit diagram, (b) Nyquist plot for a resistor⁶².

2.7.1.2. Capacitors

The impedance of capacitors is purely reactive. The resistance of an ideal capacitor is zero. When an AC voltage is applied to a capacitor, the phase angle is -90° and is described as the current leading the voltage. The impedance of a capacitor is inversely proportional to the frequency, meaning that its impedance increases as the frequency of the signal decreases.⁶⁴ The symbol shown in Fig 2.28a is for a perfect capacitor (C). Capacitors only have an imaginary component of impedance. The charge q stored in the capacitor plates is related to the potential around the plate and this gives equation:⁶⁴

$$q = CE \quad \mathbf{2.27}$$

The equation describing the impedance of a capacitor is:⁶⁴

$$Z_C = 1/j\omega C \quad \mathbf{2.28}$$

where j is the imaginary unit, ω is the radial frequency and C is the capacitance. As a result, the Nyquist plot for a capacitor is a vertical line (Fig. 2.28b), with $Z' = 0$ at all frequencies. Capacitances appear in electrochemical systems almost everywhere there is an interface. In cells containing solutions the capacitance is due to double layer formation when the charged electrode attracts oppositely charged ions in solution which arrange in a layer more-or-less parallel to the electrode surface. It can also be due to the dielectric capacitance or, as is found in solids including the solid electrolytes, at grain boundaries.⁶⁴

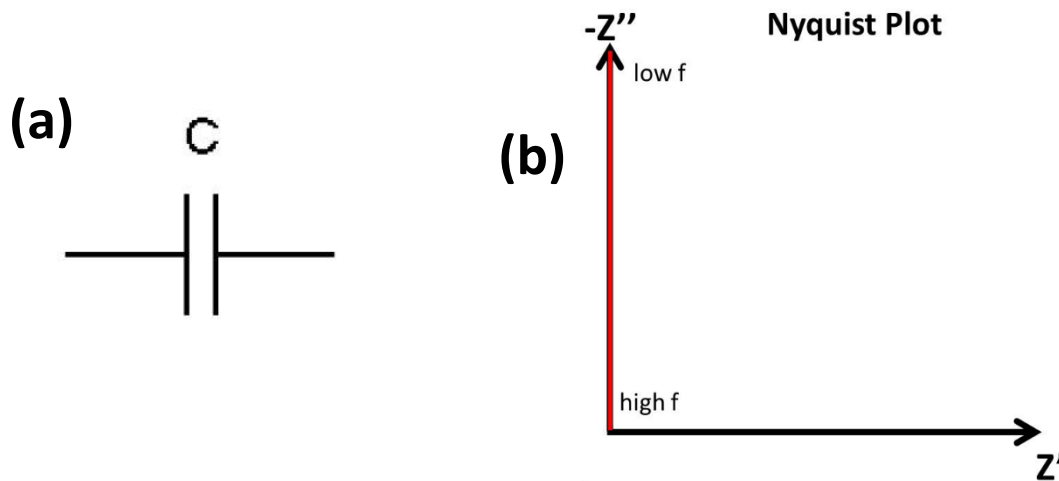


Fig. 2.28 (a) An ideal capacitor representation, (b) Nyquist plot for a capacitor⁶⁵.

2.7.1.3. Series R-C circuit

When the above two-phase elements have been positioned in series (as shown in Fig 2.29a), this equivalent circuit could apply to an ideally polarizable electrode. In this circuit the total potential drop is the sum of the capacitive and resistive impedances. As a result, the previous relationships can be represented as a sum of real and imaginary components, resulting in a complex notation. The impedance of the series RC circuit is therefore given as:⁶⁵

$$Z = Z_R + Z_C = R + 1/j\omega C \quad \mathbf{2.29}$$

Fig 2.29b shows the Nyquist plot for this circuit. For all frequencies, the real impedance (Z') equals the resistance of the resistor, and the imaginary component of the impedance ($-Z''$) behaves similarly to the ideal capacitor.

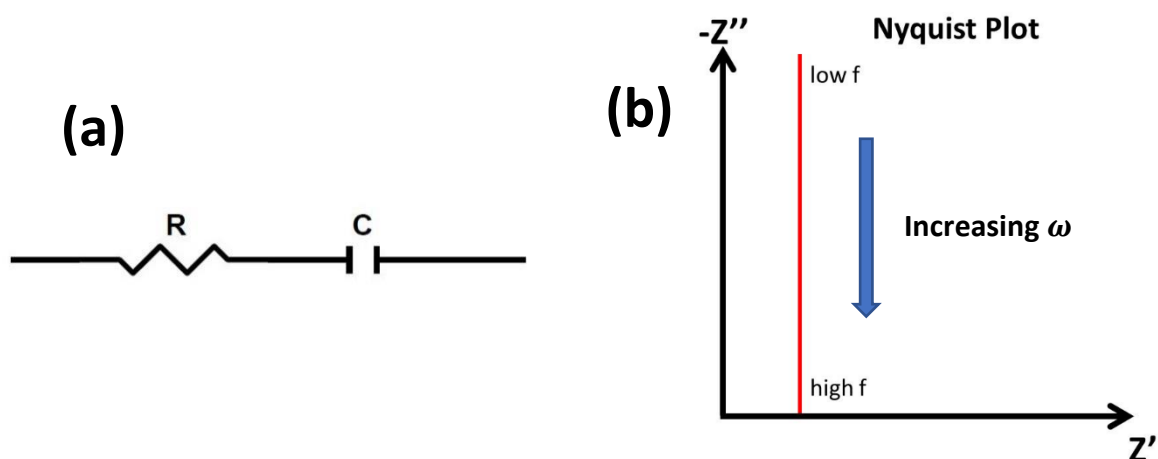


Fig. 2.29 (a) R-C circuit connected in series, (b) Nyquist plot for an ideal polarizable electrode.⁶⁴

2.7.1.4. Parallel R-C circuit

The parallel R-C circuit (Fig. 2.30a) can be representative of a real (non-ideal) polarizable electrode, which involves both Faradaic and capacitive currents. In actual electrochemical systems, these Nyquist plots are most frequently observed.⁶⁵ The admittances (i.e. the reciprocals of the impedances) are additive in parallel. As a result, we can write the parallel RC circuit expression as:

$$1/Z = 1/R + j\omega C \quad 2.30$$

If we rewrite the equation for Z (by multiplying all of the terms by R first), we get:

$$Z = R/(1 + j\omega RC) \quad 2.31$$

This equation shows that as the denominator of the fraction approaches infinity at high frequencies, (as $\omega \rightarrow \infty$), the impedance tends to zero; the ideal circuit acts like a capacitor at infinite frequency, with zero impedance. The denominator tends to 1 at low frequencies ($\omega \rightarrow 0$), so the total impedance of the circuit equals R, and the circuit behaves like a resistor. As shown in Fig. 2.30b, the Nyquist plot for this circuit is a semicircle, intersecting the real (Z') axis at 0 and R.⁶⁶

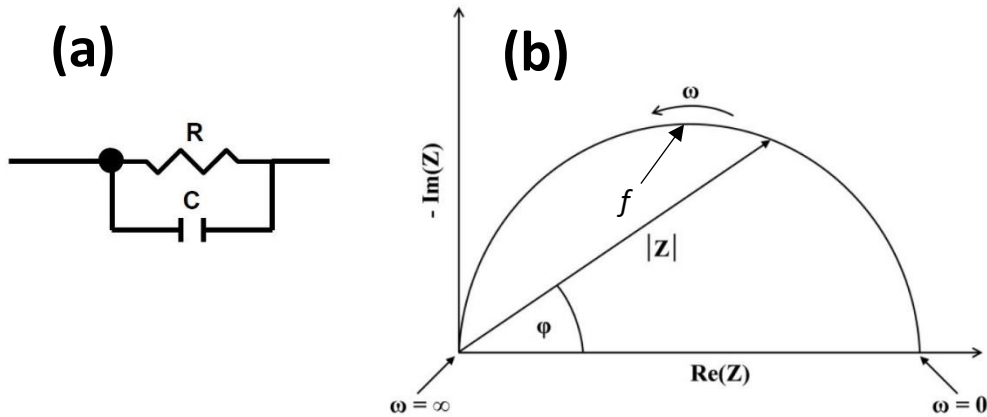


Fig. 2.30 (a) Representation of an R-C circuit connected in parallel, (b) Nyquist plot of a polarizable electrode in real life.⁶⁶

Semicircles in the Nyquist plot are often associated with processes like charge transfer where the two processes at the electrode surface, namely charge transfer which is met with a resistance and the charging of the double-layer to produce a capacitance, occur in parallel and hence the semicircle. The letter *f* written at the topmost point of the semicircle (see Fig. 2.30b.) implies the relaxation frequency, and it is related to the time constant of the RC circuit. It can be seen from Eqn. 2.31 that the semicircle's peak occurs when $\omega RC = 1$. The time constant is thus described using the following relationship:⁶⁶

$$\tau = 1/\omega = 1/2\pi f = RC$$

2.32

This provides crucial information about the time frames in which various processes take place. It is also a way to estimate the value of the capacitance, given that the resistance can be estimated from the diameter of the semicircle. Another way to assess this is using a form of the Bode plot (Fig. 2.31). In a log-scaled plot of the imaginary component against frequency, the peak of this plot corresponds to the top of the semicircle.⁶⁷

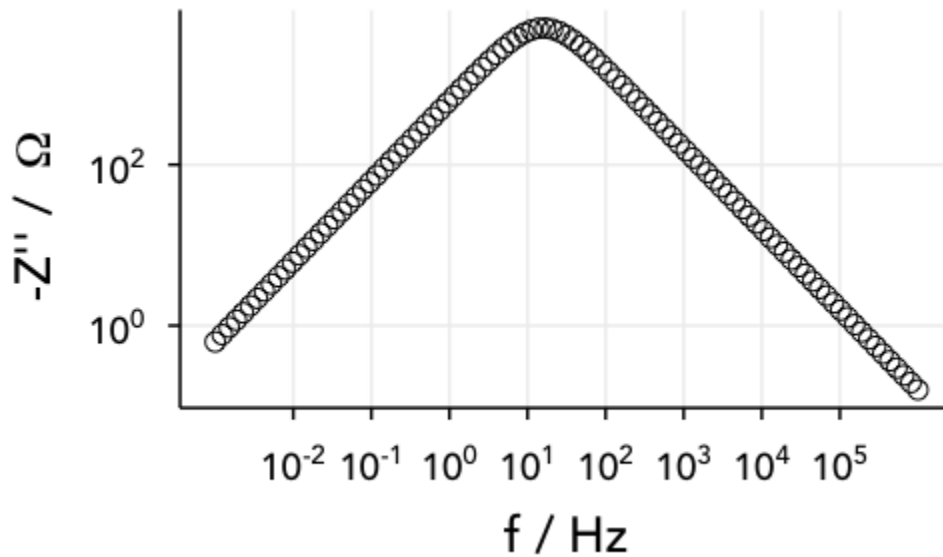


Fig. 2.31 Bode plot for a parallel RC circuit.⁶⁷

If there are a sequence of semicircles in a Nyquist plot, the value of the time constant (that is, their frequency dependence) for each of these plays a role in allocating the processes responsible for each of these RC circuits. A smaller time constant implies a higher relaxation frequency and thus the RC circuit will appear at higher frequencies. For RC circuits having very similar or identical time constants, it is generally impossible to separate the details of the processes occurring since the semicircles will overlap extensively.

Using standard circuit laws for series and parallel configurations, the total impedance can be calculated based on impedances of the individual elements. For most real electrochemical

systems an ohmic resistance is present and this can be modelled by adding a simple resistor element in series with the one shown in Fig. 2.32a. The Nyquist plot is moved by the value of the ohmic resistance in the positive X-axis direction. A depiction is shown in Fig. 2.32b. Here C_{dl} refers to the double layer capacitance at the electrode interface, R_t is the charge transfer resistance arising from processes and R_Ω describes the ohmic resistance.⁶⁷

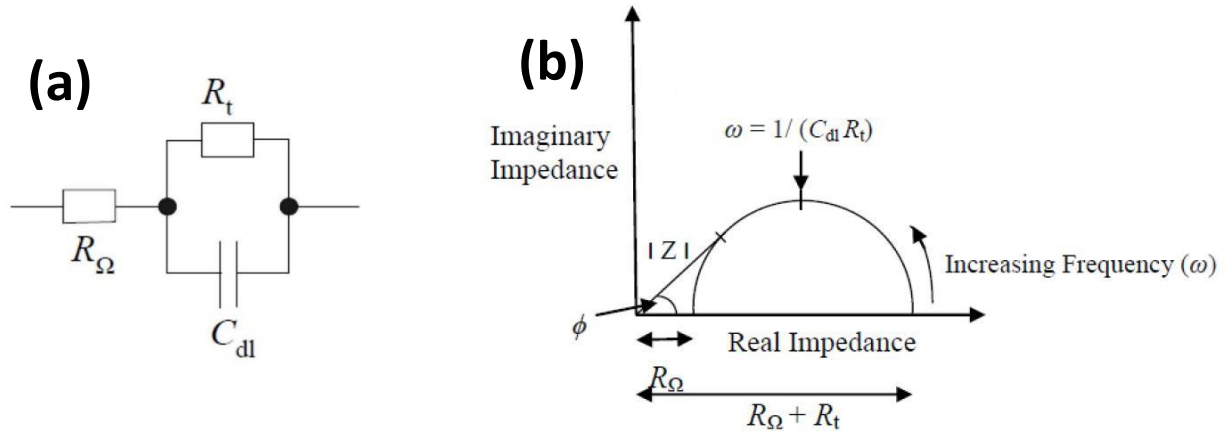


Fig. 2.32 (a) Parallel R-C circuit with a series ohmic resistance, (b) the corresponding Nyquist plot for a real-world polarizable electrode.⁶⁷

2.7.1.5. Constant Phase Element (CPE)

The CPE (symbol Q) is similar to a capacitor but represents a non-ideal capacitor, resulting in the Nyquist plot shown in Fig. 2.33a. They are often used to model solid state systems which do not show ideal capacitance. In a Nyquist plot, a RQ circuit is normally depicted as a depressed semi-circle (unlike the typical semi-circle for a capacitor) which has its centre below the actual x-axis (see Fig. 2.33b). The mathematical definition of its impedance is very similar to that of the capacitor and is given as:⁶⁸

$$Z_Q = \frac{1}{Q(j\omega)^n} \quad 2.33$$

The phase is constant (independent of frequency) and is equal to $(-90 \times n)^\circ$ and n is a number between 0 and 1.

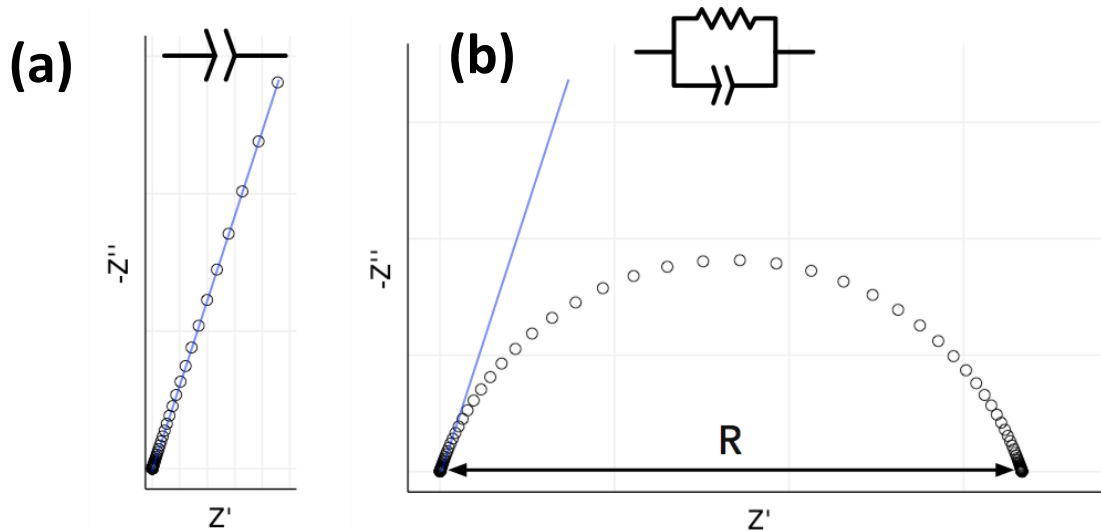


Fig. 2.33 Nyquist plot for a CPE element, on its own (a), and in the form of a depressed semi-circle (b).⁶⁵

The centre of the semi-circle is located at an angle of $(1-n) \times 90^\circ$ from the origin and n is thus the parameter of depression. The case where $n=1$ applies to an ideal capacitive element. The CPE component implies non-uniform current distribution, and this can be caused by factors such as electrode surface roughness, variations in the electrode thickness or composition, or systems with highly distributed reaction rates.⁶⁹ For example, if looking at SOFCs, the electrodes are generally porous and as a result of its manufacturing process, different regions on the catalyst are expected to have different activation energy.⁶⁹

Therefore, electrochemical oxidation or reduction reactions occur differently around the anode or cathode surface, respectively, resulting in a CPE activity at different levels. Different "edge effects" creep through due to different current collector materials (mesh and paste) used in a SOFC in a home-made environment, causing current variation across the entire surface.⁷⁰ As a result of this effect, the current in the active area's center may be lower than at the edge, increasing the device's overall surface roughness factor. Because of these factors, fuel cell stacks which are commercially built to be more robust show more ideal capacitive behavior, while home-made cells are less uniform and thus show CPE behaviour.⁷⁰

2.7.1.6. Warburg Element

The Warburg impedance (symbol W), models semi-infinite linear diffusion – that is, one-dimensional diffusion bounded only by a large planar electrode on one side.⁷¹ The equation for the Warburg impedance is relatively simple for such an element and is given as:

$$Z_W = \sigma\omega^{-0.5} - j\sigma\omega^{-0.5} \quad \mathbf{2.34}$$

where σ is the Warburg coefficient, with units of $\Omega s^{-0.5}$. The Warburg impedance Z_W is used to model the low frequency regions where the relatively slow process of diffusion dominates (Fig. 2.34). At high frequencies, the reactants or ions do not have time to move or diffuse when the applied signal is alternating very fast.⁷¹ On a Nyquist plot, the Warburg impedance should preferably appear as a line with a slope of 0.5 or at a 45° angle to the x-axis, as shown in Fig. 2.34b. The Warburg or diffusion impedance is a physical parameter that is derived from Fick's first law of diffusion and the information obtained from this parameter can be used to find values of the diffusion layer thickness and the diffusion coefficient for systems where this plays an important role.⁷²

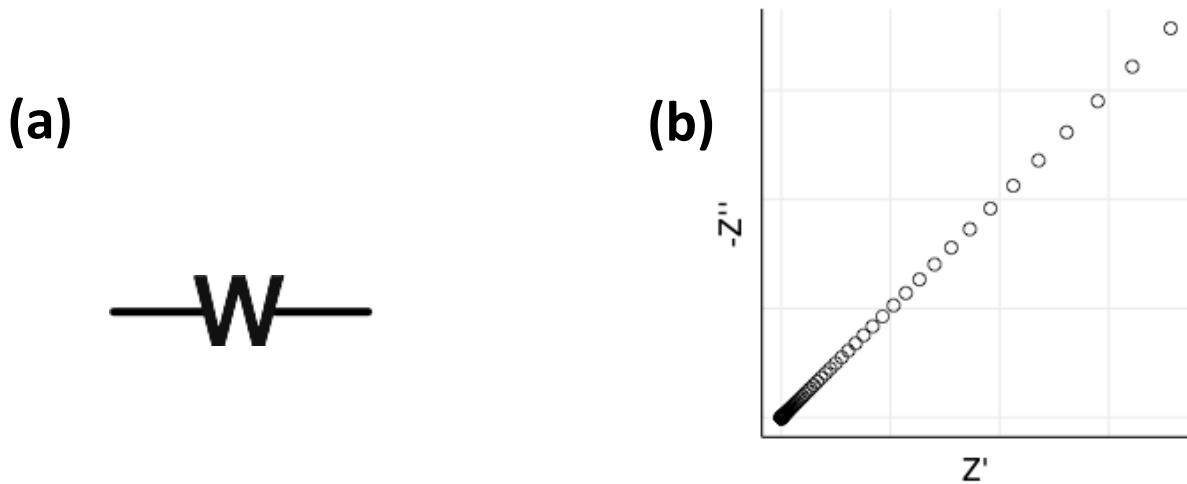


Fig. 2.34 (a) Warburg element representation, (b) representative Nyquist plot for a Warburg element showing mass diffusion behaviour.⁶⁵

Based on the frequencies used the time scale of the experiment is too short for the system to reach a stable state therefore diffusion tends to be semi-infinite. In some cases, diffusion is often further restricted, either by the system or by the experimental parameters. This causes finite diffusion behaviour, which differs from the standard Warburg impedance response.⁶⁶

Finite diffusion has two main equivalent circuit components. These are the finite space Warburg (FSW) and finite-length Warburg (FLW), also called the "open" and "short" Warburg elements, respectively (Fig. 2.35). For this study, we will only focus on FLW as FSW is not expressed in our Nyquist plots as it is associated with the diffusion of ions within a storage electrode, such as in lithium-ion batteries.⁷³ Nyquist plot example of their responses are given in Fig. 2.35.

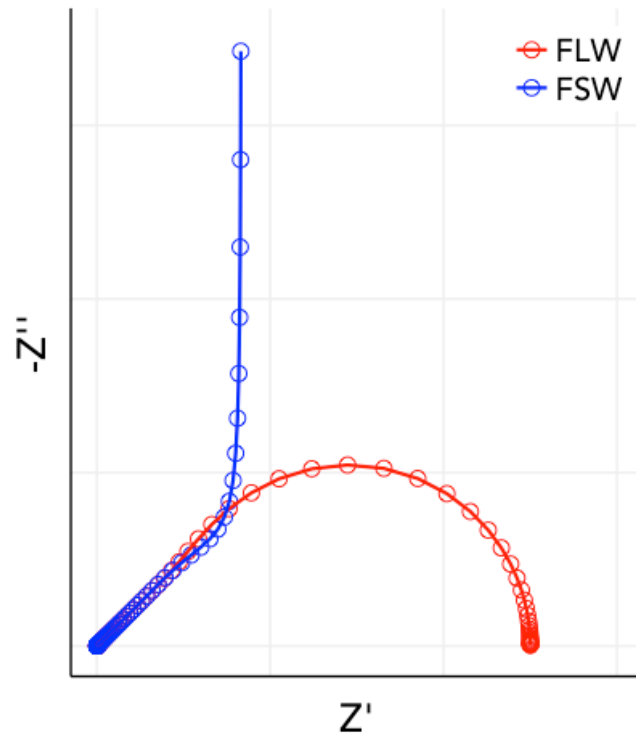


Fig. 2.35 Nyquist plot for finite Warburg elements.⁶⁵

Mathematically, the impedance of a FLW⁶⁵ can be given as:

$$Z_{FLW} = Z_0(j\omega\tau)^{-0.5} \tanh(j\omega\tau^{0.5}) \quad \mathbf{2.35}$$

The properties of the device or process that causes FLW behavior are described by Z_0 and τ . The impedance of the FLW approaches Z_0 at lower frequencies. At high frequencies, the response is similar to Warburg impedance. As a result, the FLW shape in the Nyquist plot appears as a 45° line at higher frequencies and transforms into a semi-circle shape at lower frequencies. It's like a Warburg being "shorted" by a resistor, although the same response will not be given by a parallel W-R circuit.⁷⁴ Usually, this response is correlated with diffusion (or mass transport) through a finite-length layer. An example where this plays a critical role is in rotating disk electrodes where the convection from the electrode reduces the diffusion layer thickness (i.e. the distance between the electrode and the bulk solution).⁷⁵

2.7.1.7. Circuit Obscurity and Fitting Algorithms

While EIS is a powerful technique in conjunction with ECM, it does have a big downside. The circuit models could be non-unique, where a single specific Nyquist plot could fit several models. Therefore, as a researcher, it's much more critical to first understand the system's physical nature and potential reaction schemes before attempting to fit a definite model to the impedance data. From the outset, it is a good idea to use simpler circuits to begin modelling the system after understanding the basics of the system. Complex and specialized circuits can then be incorporated into existing models to better simulate the behaviour, both in terms of fitting and valid conceptual reasoning.⁷⁶

ZFit is the program that is used to fit impedance data to analogous circuit models. The program uses the standard, complex nonlinear least squares (CNLS) method which is one of the most common experimental data fitting techniques.⁶⁰ The chi-squared (χ^2) algorithm was used to increase the efficiency of the CNLS-fitting. A smaller χ^2 value suggests a better statistical fit for the circuit model being considered. The CNLS method can converge when a "local minimum" is reached, as indicated by a large χ^2 . To reach the global minimum the initial estimated values for the various parameters should be slightly altered and then the fitting process restarted. It is also possible to fix the values of specific parameters while the others are being refined.^{75,76}

2.8. References

1. Omari, M., Drache, M., Conflant, P. and Boivin, J.C., 1990. Anionic conduction properties of the fluorite-type phase in the $\text{Bi}_2\text{O}_3\text{-Y}_2\text{O}_3\text{-PbO}$ system. *Solid State Ionics*, 40, pp.929-933.
2. Förster, A., Brandstetter, S. and Schulze-Briese, C., 2019. Transforming X-ray detection with hybrid photon counting detectors. *Philosophical Transactions of the Royal Society A*, 377(2147), p.20180241.
3. Laufek, F., Paout, R. and Makovicky, E., 2007. Crystal structure of owyheeite, $\text{Ag}_{1.5}\text{Pb}_{4.43}\text{Sb}_{6.07}\text{S}_{14}$: refinement from powder synchrotron X-ray diffraction. *European Journal of Mineralogy*, 19(4), pp.557-566.
4. Gražulis, S., Chateigner, D., Downs, R.T., Yokochi, A.F.T., Quirós, M., Lutterotti, L., Manakova, E., Butkus, J., Moeck, P. and Le Bail, A., 2009. Crystallography Open Database—an open-access collection of crystal structures. *Journal of Applied Crystallography*, 42(4), pp.726-729.
5. Coelho, A.A., 2018. TOPAS and TOPAS-Academic: an optimization program integrating computer algebra and crystallographic objects written in C++. *Journal of Applied Crystallography*, 51(1), pp.210-218.
6. Cheary, R.W. and Coelho, A., 1992. A fundamental parameters approach to X-ray line-profile fitting. *Journal of Applied Crystallography*, 25(2), pp.109-121.
7. Harwig, H. and Weenk, J., 1978. Phase Relations in Bismuthsesquioxide. *Zeitschrift für Anorganische und Allgemeine Chemie*, 444(1), pp.167-177.
8. Battle, P., Catlow, C., Drennan, J. and Murray, A., 1983. The structural properties of the oxygen conducting δ phase of Bi_2O_3 . *Journal of Physics C: Solid State Physics*, 16(17), pp.L561-L566.
9. Battle, P., Catlow, C., Heap, J. and Moroney, L., 1986. Structural and dynamical studies of $\delta\text{-Bi}_2\text{O}_3$ oxide ion conductors. *Journal of Solid-State Chemistry*, 63(1), pp.8-15.
10. Chupas, P.J., Qiu, X., Hanson, J.C., Lee, P.L., Grey, C.P. and Billinge, S.J., 2003. Rapid-acquisition pair distribution function (RA-PDF) analysis. *Journal of Applied Crystallography*, 36(6), pp.1342-1347.
11. Biologic. 2021. HTF-1100 - Biologic. [online] Available at: <<https://www.biologic.net/products/htf-1100-high-temperature-furnace/>> [Accessed 9 December 2021].
12. Kovyakh, A., 2018. *X-ray pair distribution function analysis of transition and noble metals for industrial applications in sensing and catalysis* (Doctoral dissertation, The Niels Bohr Institute, Faculty of Science, University of Copenhagen).
13. Bacon, G., 1966. The applications of X-ray and neutron diffraction. *Endeavour*, 25(96), pp.129-135.
14. Dorset, D., 1998. X-ray Diffraction: A Practical Approach. *Microscopy and Microanalysis*, 4(5), pp.513-515.
15. Humphreys, C.J., 2013. The significance of Bragg's law in electron diffraction and microscopy, and Bragg's second law. *Acta Crystallographica Section A: Foundations of Crystallography*, 69(1), pp.45-50.
16. Elton, L.R.B. and Jackson, D.F., 1966. X-ray diffraction and the Bragg law. *American Journal of Physics*, 34(11), pp.1036-1038.
17. Huff, W., 1990. X-ray Diffraction and the Identification and Analysis of Clay Minerals. *Clays and Clay Minerals*, 38(4), pp.448-448.
18. Dinnebier, R.E. and Billinge, S.J., 2008. Principles of powder diffraction. *Powder Diffraction: Theory and Practice*, pp.1-19.
19. Fitch, A. and Cockcroft, J., 1992. Low-temperature powder diffraction studies using synchrotron radiation. *Phase Transitions*, 39(1-4), pp.161-170.

20. Cheary, R.W., Coelho, A.A. and Cline, J.P., 2004. Fundamental parameters line profile fitting in laboratory diffractometers. *Journal of Research of the National Institute of Standards and Technology*, 109(1), p.1.
21. Deutsch, M., Förster, E., Hölzer, G., Härtwig, J., Hämäläinen, K., Kao, C.C., Huotari, S. and Diamant, R., 2004. X-ray spectrometry of copper: new results on an old subject. *Journal of research of the National Institute of Standards and Technology*, 109(1), p.75.
22. Sciencedirect.com. 2021. *Journal of Physics and Chemistry of Solids | ScienceDirect.com by Elsevier*. [online] Available at: <<https://www.sciencedirect.com/journal/journal-of-physics-and-chemistry-of-solids>> [Accessed 9 December 2021].
23. Parkin, I., 2000. Basic Solid State Chemistry Anthony R. West 2nd edn. John Wiley & Sons, Chichester. *Applied Organometallic Chemistry*, 14(4), pp.227-228.
24. Uvarov, V. and Popov, I., 2007. Metrological characterization of X-ray diffraction methods for determination of crystallite size in nano-scale materials. *Materials Characterization*, 58(10), pp.883-891.
25. Caciuffo, R., Melone, S., Rustichelli, F. and Boeuf, A., 1987. Monochromators for x-ray synchrotron radiation. *Physics Reports*, 152(1), pp.1-71.
26. vdocuments.site. 2021. *Solid state chemistry. Techniques: Edited by A. K. Cheetham and P. Day, The Clarendon Press, Oxford University Press*. [online] Available at: <<https://vdocuments.site/solid-state-chemistry-techniques-edited-by-a-k-cheetham-and-p-day-the.html>> [Accessed 9 December 2021].
27. Friedrich, W., Knipping, P. and Laue, M., 1913. Interferenzerscheinungen bei Röntgenstrahlen. *Annalen der Physik*, 346(10), pp.971-988.
28. Uruga, T., 2017. Synchrotron-Radiation Sources, X-ray Optics and Beamlines. In *XAFS Techniques for Catalysts, Nanomaterials, and Surfaces* (pp. 53-62). Springer, Cham. Courant, E.D., Livingston, M.S. and Snyder, H.S., 1952. The strong-focusing synchrotron—A new high energy accelerator. *Physical Review*, 88(5), p.1190.
29. Benedek, G., 1992. 2nd European Conference on Progress in X-Ray Synchrotron Radiation Research. *Il Nuovo Cimento A*, 105(3), pp.453-453.
30. Smith, D., Fiala, J. and Ryba, E., 1993. Book Reviews - The Rietveld Method, R. A. Young, Editor, IUCr Monographs in Crystallography, 5, International Union of Crystallography, Oxford University Press, New York, NY. *Powder Diffraction*, 8(4), pp.252-254.
31. Von Dreele, R., 1996. Rietveld analysis of high-pressure powder diffraction data. *High Pressure Research*, 14(4-6), pp.321-326.
32. Rietveld, H., 1967. Line profiles of neutron powder-diffraction peaks for structure refinement. *Acta Crystallographica*, 22(1), pp.151-152.
33. McCusker, L.B., Von Dreele, R.B., Cox, D.E., Louër, D. and Scardi, P., 1999. Rietveld refinement guidelines. *Journal of Applied Crystallography*, 32(1), pp.36-50.
34. Nikolic, J., Expósito, E., Iniesta, J., González-García, J. and Montiel, V., 2000. Theoretical concepts and applications of a rotating disk electrode. *Journal of Chemical Education*, 77(9), p.1191.
35. Schmidt, C., Rittmeier-Kettner, M., Becker, H., Ellert, J., Krombach, R. and Schneider, G., 1994. Differential thermal analysis (DTA) and differential scanning calorimetry (DSC) at high pressures. Experimental techniques and selected results. *Thermochimica Acta*, 238, pp.321-336.
36. Apostolescu, D., 1995. Thermal methods of analysis, principles, applications and problems. *Journal of Thermal Analysis*, 45(1-2), pp.335-336.
37. Mackenzie, R., 1984. Origin and development of differential thermal analysis. *Thermochimica Acta*, 73(3), pp.307-367.
38. Kasper, M., 2004. G.W.H. Höhne, W.F. Hemminger, H.-J. Flammersheim: Differential scanning calorimetry. *Analytical and Bioanalytical Chemistry*, 380(3), pp.366-367.

39. Székely, T., 1986. Thermophysical properties of solids. Their measurement and theoretical thermal analysis. *Journal of Analytical and Applied Pyrolysis*, 9(3), pp.265-266.
40. Hitachi-hightech.com. 2020. *Principle Of Thermogravimetry (TG) : Hitachi High-Tech GLOBAL*. [online] Available at: <<https://www.hitachi-hightech.com/global/products/science/tech/ana/thermal/descriptions/tg.html>> [Accessed 1 October 2020].
41. Wachs, I.E., Hardcastle, F.D. and Chan, S.S., 1986. Raman spectroscopy of supported metal oxide catalysts. *Spectroscopy*, 1, pp.30-38.
42. Hardcastle, F.D. and Wachs, I.E., 1992. The molecular structure of bismuth oxide by Raman spectroscopy. *Journal of Solid-State Chemistry*, 97(2), pp.319-331.
43. Brown, I.D., 1978. Bond valences—a simple structural model for inorganic chemistry. *Chemical Society Reviews*, 7(3), pp.359-376.
44. Brown, I.T. and Wu, K.K., 1976. Empirical parameters for calculating cation–oxygen bond valences. *Acta Crystallographica Section B: Structural Crystallography and Crystal Chemistry*, 32(7), pp.1957-1959.
45. Bordet, P., 2015. Local structure studies using the pair distribution function. *EPJ Web of Conferences*, 104, p.01003.
46. Bordet, P., 2018. Application of the pair distribution function analysis for the study of cultural heritage materials. *Comptes Rendus Physique*, 19(7), pp.561-574.
47. Grey, I.E., Bordet, P., Wilson, N.C., Townend, R., Bastow, T.J. and Brunelli, M., 2010. A new Al-rich hydroxylated pseudorutile from Kalimantan, Indonesia. *American Mineralogist*, 95(1), pp.161-170.
48. Chapman, K.W., Chupas, P.J., Halder, G.J., Hriljac, J.A., Kurtz, C., Greve, B.K., Ruschman, C.J. and Wilkinson, A.P., 2010. Optimizing high-pressure pair distribution function measurements in diamond anvil cells. *Journal of Applied Crystallography*, 43(2), pp.297-307.
49. Yang, X., Masadeh, A.S., McBride, J.R., Božin, E.S., Rosenthal, S.J. and Billinge, S.J., 2013. Confirmation of disordered structure of ultrasmall CdSe nanoparticles from X-ray atomic pair distribution function analysis. *Physical Chemistry Chemical Physics*, 15(22), pp.8480-8486.
50. Egami, T. and Billinge, S., 2003. Underneath the Bragg Peaks. *Materials Today*, 6(6), p.57.
51. Grena, R., Masson, O., Portal, L., Remondiere, F., Berghout, A., Jouin, J. and Thomas, P., 2015. Stabilization Effect of Surface Impurities on the Structure of Ultrasmall ZrO₂ Nanoparticles: An Ab-Initio Study. *The Journal of Physical Chemistry C*, 119(27), pp.15618-15626.
52. Olaj, O., 1976. Pair distribution function and pair potential of lattice model chains under theta conditions, 2. Theoretical approach. *Die Makromolekulare Chemie*, 177(11), pp.3427-3435.
53. Davis, T., Johnson, M. and Billinge, S.J., 2013. Toward Phase Quantification at the Nanoscale Using the Total Scattering Pair Distribution Function (TSPDF) Method: Recrystallization of Cryomilled Sulfamerazine. *Crystal growth & design*, 13(10), pp.4239-4244.
54. Dykhne, T., Taylor, R., Florence, A. and Billinge, S.J., 2011. Data requirements for the reliable use of atomic pair distribution functions in amorphous pharmaceutical fingerprinting. *Pharmaceutical Research*, 28(5), pp.1041-1048.
55. Kaban, I., Jóvári, P., Hoyer, W. and Welter, E., 2007. Determination of partial pair distribution functions in amorphous Ge₁₅Te₈₅ by simultaneous RMC simulation of diffraction and EXAFS data. *Journal of Non-Crystalline Solids*, 353(24-25), pp.2474-2478.
56. Keen, D.A., Tucker, M.G. and Dove, M.T., 2005. Reverse Monte Carlo modelling of crystalline disorder. *Journal of Physics: Condensed Matter*, 17(5), p.S15.
57. Farrow, C.L., Juhas, P., Liu, J.W., Bryndin, D., Božin, E.S., Bloch, J., Proffen, T. and Billinge, S.J.L., 2007. PDFfit2 and PDFgui: computer programs for studying nanostructure in crystals. *Journal of Physics: Condensed Matter*, 19(33), p.335219.

58. Larminie, J., 2003. Fuel Cell-Technology Handbook. *Proceedings of the Institution of Mechanical Engineers, Part D: Journal of Automobile Engineering*, 217(5), pp.415-415.
59. Hollins, P., 1988. Impedance spectroscopy: Emphasizing solid materials and systems. *Spectrochimica Acta Part A: Molecular Spectroscopy*, 44(8), p.853.
60. Holze, R., 2002. Book Review: Electrochemical Methods. Fundamentals and Applications (2nd Edition). By Allen J. Bard and Larry R. Faulkner. *Angewandte Chemie International Edition*, 41(4), pp.655-657.
61. Goodenough, J., 2007. Oxide Components for the Solid Oxide Fuel Cell. *ChemInform*, 38(2).
62. Choi, W., Shin, H.C., Kim, J.M., Choi, J.Y. and Yoon, W.S., 2020. Modeling and Applications of Electrochemical Impedance Spectroscopy (EIS) for Lithium-ion Batteries. *Journal of Electrochemical Science and Technology*, 11(1), pp.1-13.
63. Virkar, A., Williams, M. and Singhal, S., 2019. Concepts for Ultra-high Power Density Solid Oxide Fuel Cells. *ECS Transactions*, 5(1), pp.401-421.
64. Matt lacey. 2020. Simple circuits with resistors and capacitors. [ONLINE] Available at: <http://lacey.se/science/eis/simple-circuits/>. [Accessed 31 August 2020].
65. Palmsens. 2020. Bode and Nyquist Plot. [ONLINE] Available at: <https://www.palmsenscorrosion.com/knowledgebase/bode-and-nyquist-plot/>. [Accessed 31 August 2020].
66. Fletcher, S., Black, V.J. and Kirkpatrick, I., 2014. A universal equivalent circuit for carbon-based supercapacitors. *Journal of Solid-State Electrochemistry*, 18(5), pp.1377-1387.
67. Bredar, A.R., Chown, A.L., Burton, A.R. and Farnum, B.H., 2020. Electrochemical Impedance Spectroscopy of Metal Oxide Electrodes for Energy Applications. *ACS Applied Energy Materials*, 3(1), pp.66-98.
68. Kalinin, S. and Bonnell, D., 2002. Scanning Impedance Microscopy: From Impedance Spectra to Impedance Images. *Microscopy Today*, 10(1), pp.22-27.
69. Holze, R., 2002. Book Review: Instrumental Methods in Electrochemistry. Edited by Southampton Electrochemistry Group. *Angewandte Chemie International Edition*, 41(4), pp.655-657.
70. Zheltikov, A., 2006. Impedance Spectroscopy: Theory, Experiment, and Applications Second Edition. Evgenij Barsoukov and J. Ross Macdonald (eds). John Wiley & Sons, Inc., Hoboken, New Jersey, 2005, pp. 595. *Journal of Raman Spectroscopy*, 38(1), pp.122-122.
71. Rodrigues, S., Munichandraiah, N.S.A.K. and Shukla, A.K., 1999. AC impedance and state-of-charge analysis of a sealed lithium-ion rechargeable battery. *Journal of Solid-State Electrochemistry*, 3(7-8), pp.397-405.
72. Kochowski, S. and Nitsch, K., 2002. Description of the frequency behaviour of metal-SiO₂-GaAs structure characteristics by electrical equivalent circuit with constant phase element. *Thin Solid Films*, 415(1-2), pp.133-137.
73. Matt lacey. 2020. Diffusion Impedance [ONLINE] Available at: <http://lacey.se/science/eis/simple-circuits/>. [Accessed 31 August 2020].
74. Taylor, S.R. and Gileadi, E., 1995. Physical interpretation of the Warburg impedance. *Corrosion*, 51(9), pp.664-671.
75. Boukamp, B.A., 2004. Electrochemical impedance spectroscopy in solid state ionics: recent advances. *Solid State Ionics*, 169(1-4), pp.65-73.
76. Boukamp, B.A., 2017. Derivation of a Distribution Function of Relaxation Times for the (fractal) Finite Length Warburg. *Electrochimica Acta*, 252, pp.154-163.

3.1. X-ray diffraction analysis

The two batches of samples, as described based on the total dopant concentration, were analysed by PXRD at room temperature. One batch of samples (ranged from ~25-48%) had a higher total dopant concentration, for example, 26.5 mol% (1.5Pb25YSB) whereas the other (ranged from 10-20%) had a lower total dopant concentration, for example, 15 mol% (5Pb10YSB). The high total dopant composition samples were chosen in line with the findings of Omari et al.¹ who published a paper on the Bi₂O₃-PbO-Y₂O₃ system, with the goal of integrating the high efficiency of the Bi₂O₃-PbO system with the better stability of the Bi₂O₃-Y₂O₃ system. Within some compositional areas, this was accomplished satisfactorily. In the Bi_{0.75(1-x)}Pb_{0.75x}Y_{0.25}O_{1.5-0.375x} system, the authors stated the compositional variation of the lattice parameter and concluded that double substitution of Pb²⁺ and Y³⁺ for Bi³⁺ in Bi₂O₃ yields stabilised δ-Bi₂O₃ type phases with high conductivity.¹ Thus moving from pure Bi₂O₃ that exists as a α-phase (*P21/c*, space group) at room temperature, the Bi₂O₃ doped systems with particular compositions (for example doped with Dy₂O₃, Y₂O₃, Er₂O₃ and Yb₂O₃) can stabilise the cubic δ-Bi₂O₃ type phase (space group *Fm-3m*) at ambient temperature.

The samples with lower total dopant concentration were synthesised to determine the minimum total dopant concentration required to stabilize δ-Bi₂O₃ and improve the conductivity by varying the dopant ratio between Pb²⁺ and Y³⁺. It has been shown that δ-phase stabilization was achieved with co-doping at a comparatively lower total dopant concentration (~12 mol%) when compared to the single dopant method.² With the lower dopant concentrations, the resulting conductivities were thus higher.² For example high conductivity (0.098 S/cm) was obtained from (DyO_{1.5})_{0.08}(WO₃)_{0.04}(BiO_{1.5})_{0.88} composition (8D4WSB) with a total dopant concentration of 12 mol% at 500°C.^{3,4} Jung et al.⁵ have developed a co-doped bismuth oxide electrolyte with a total dopant concentration of 12 mol%, consisting of 8 mol% Dy and 4 mol% Gd (8D4GSB). Again, the phase pure cubic crystal structure was achieved. At 600 and 500 °C, this material showed an

oxygen ion conductivity of 0.18 and 0.1 S cm⁻¹, respectively. In this temperature region, these are among the highest conductivity values recorded.

In this work, by developing a different co-doping system (one isovalent Y³⁺ dopant and one aliovalent dopant Pb²⁺), PbYSB material with lower total dopant concentration, we wanted to improve these recorded conductivity values in order to determine the effect of PbO and Y₂O₃ in the PbYSB system. Additionally, by having the Pb²⁺ ion present, we wanted to see if the extra O-vacancies and the lone pair on Pb²⁺ improved the conductivity.

3.1.1. Higher total dopant concentration

Fig. 3.1 shows the XRD patterns of the singly doped specimens, namely 25PbSb. The diffractogram showed the coexistence of the majority of cubic and minor tetragonal phases. Thus, this result indicates that Pb²⁺ alone cannot stabilise the high conductivity cubic structure of bismuth oxides. Studies conducted by Omari *et al.*¹ on the Bi₂O₃-PbO system showed that some solid solutions (β -Bi₅Pb₃O_{10.5} and β -Bi₈Pb₅O₁₇) in this system show high ionic conductivity at ca. 600°C. These highly conductive tetragonal phases, however, have only been found to be stable over a very narrow temperature range (630°C). Therefore, the fluorite δ -phase of Bi₂O₃ was found to be unstable when Pb was used as a main substituent.

Laboratory X-ray diffraction information indicated that (BiO_{1.5})_{0.75-x}(PbO)_x(YO_{1.5})_{0.25} solid solutions annealed at 700°C retain a fluorite structure throughout the composition range studied (0.015 ≤ x ≤ 0.225). The synthesized co-doped bismuth oxide materials were generally divided into low (e.g., 5Pb10YSB) and high (e.g., 1.5Pb25YSB) total dopant concentration classes, with the intention to produce and stabilize the fcc type δ -Bi₂O₃ solid solution. Due to limitations in access to state-of-the-art techniques, such as, Synchrotron Powder X-ray Diffraction and Raman Spectroscopy (RS), only two samples were fully characterized. These were 5Pb10YSB and 1.5Pb25YSB which represent co-doped bismuth oxide materials from the low and high total dopant concentration range, respectively. Fig. 3.2a shows laboratory diffraction patterns for 1.5Pb25YSB, 6Pb25YSB, 9Pb25YSB and 15Pb25YSB. All the indexed peaks belong to the δ -Bi₂O₃ (from inorganic crystal structure data base) and no additional peaks were observed in the diffractograms, indicating phase stability of the pure δ -Bi₂O₃ at room temperature. The same

samples (containing 25% Y and from 1.5 – 15% Pb) were measured on a beamline 28-ID-2 at the National Light Source II at Brookhaven National Laboratory and showed the same δ - Bi_2O_3 phase (Fig. 3.2b) as the ones measured on a Bruker D2 phaser, indicating that indeed δ - Bi_2O_3 phase was stabilised at ambient temperature by using a high total dopant concentration (26.5 – 40%).

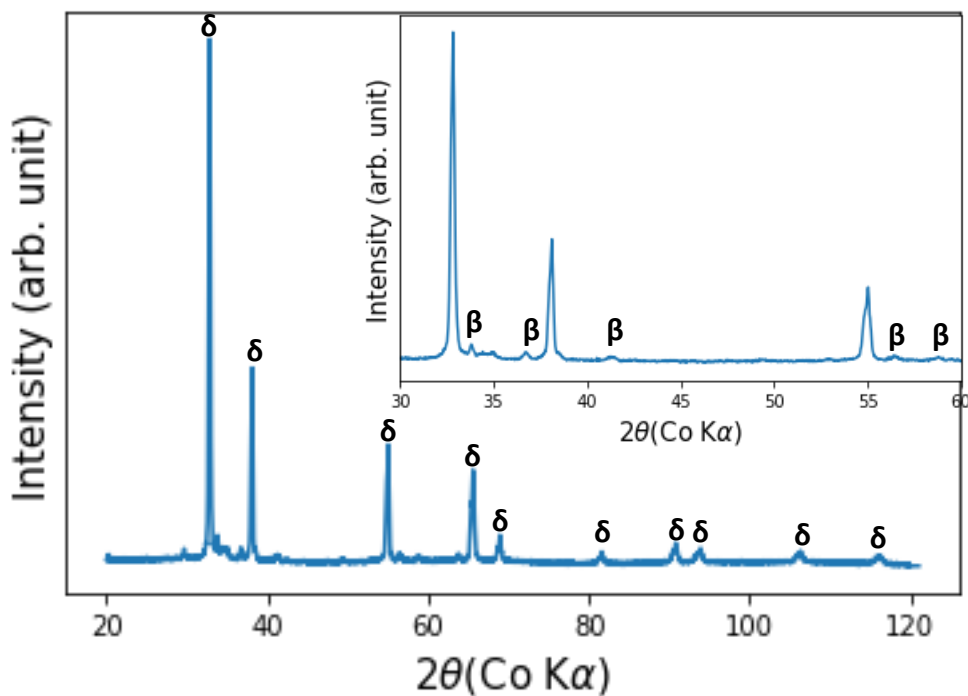


Fig. 3.1 XRD pattern of 25PbSB showing a mixture of phases annealed at 700°C. Inset shows a magnified region at the range of 2θ angle from 30 to 60 degrees.

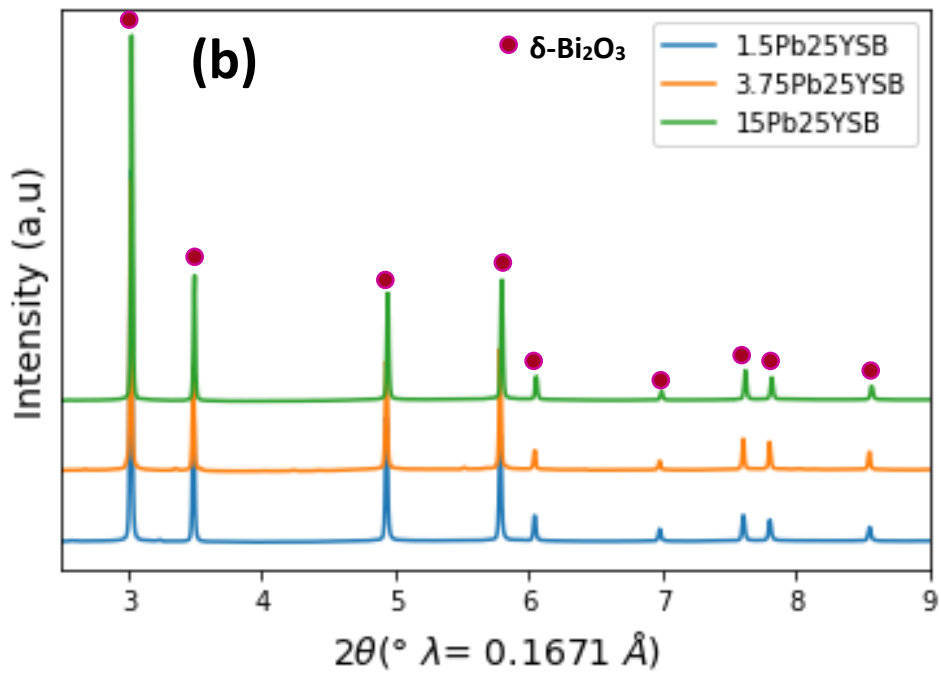
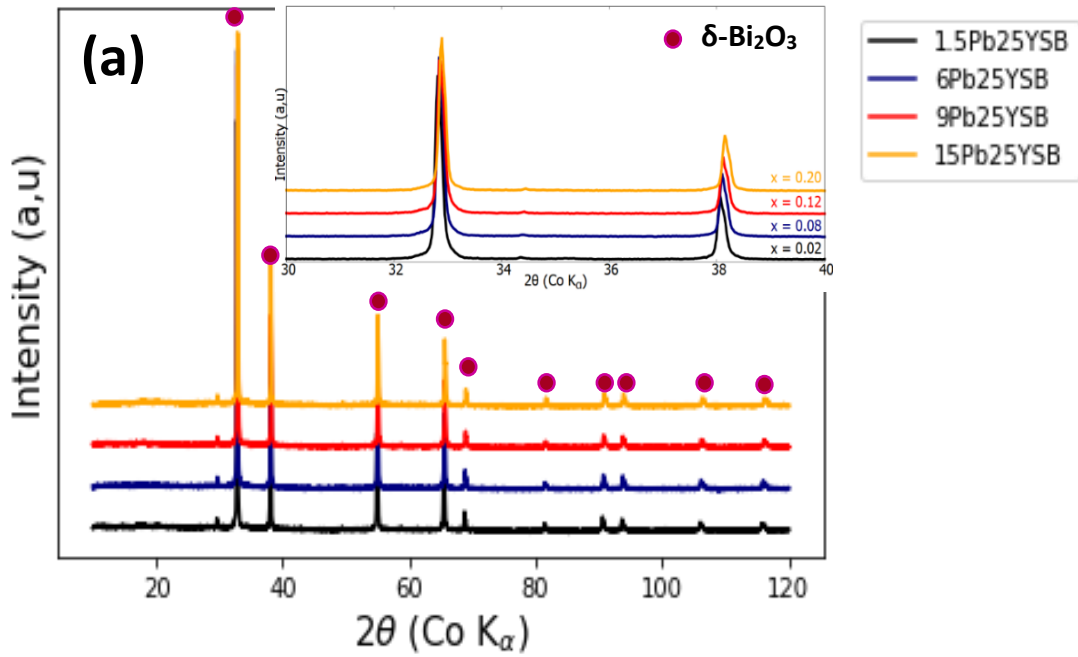


Fig. 3.2 Laboratory XRD patterns for 1.5Pb25YSB, 6Pb25YSB, 9Pb25YSB and 15Pb25YSB and a magnified inset showing data between 30° to 40° (2θ) (a); Synchrotron diffractograms for 1.5Pb25YSB, 3.75Pb25YSB and 15Pb25YSB (b). All samples were annealed at 700°C for 12 hours.

Two of the samples, 3.75Pb25YSB and 7.5Pb25YSB, from the high dopant concentration class were further annealed at 800°C for 20 hours as they were the only two samples from the high dopant concentration class that maintained the δ -phase at 750°C to see if they are stable at even higher temperatures. However, both exhibited anisotropic peak broadening, peak splitting and showed additional peaks which are yet to be identified in the diffractograms (Fig. 3.3) with phase degradation taking place to form a mixture of phases. From this observation it was concluded that to obtain a δ -phase at higher temperature it is best to anneal the samples at 700°C as this temperature results with a single phase as it is close to a temperature which results in phase degradation.

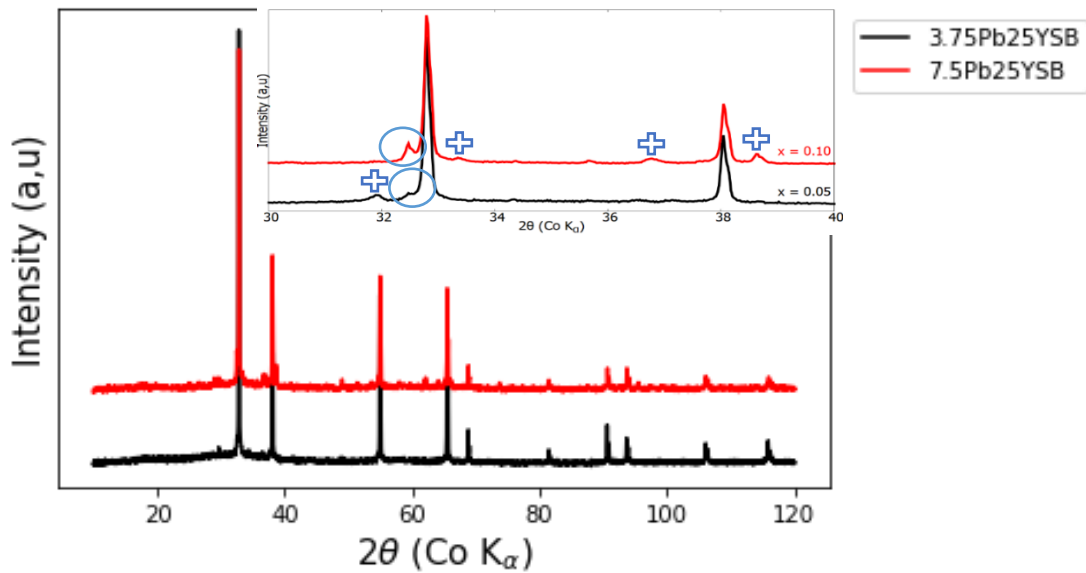


Fig. 3.3 X-ray diffraction patterns for 3.75Pb25YSB and 7.5Pb25YSB annealed at 800°C for 20 hours. Blue circles and (+) on the magnified inset between 30° to 40° (2θ) indicate shoulders on the side of peaks and some of the additional peaks that were observed, respectively.

The starting model (ICSD 98144) for refinements was based on the space group $Fm-3m$ derived for pure δ - Bi_2O_3 , with cations statistically distributed at the $4a$ (0, 0, 0) sites and oxygen atoms at the standard $8c$ ($\frac{1}{4}, \frac{1}{4}, \frac{1}{4}$) and $32f$ (x, x, x) interstitial sites as shown in Fig. 3.4.⁸ The isotropic temperature factors of the cation sites, and the occupancy, position and scale factors of the anion sites were refined to achieve a good fit between the measured and observed profiles as shown

in Fig. 3.5a and 3.5b. The high degree of disorder in this structure, shown by a decrease in peak intensity with 2θ , is verified by the high thermal parameters of the cations shown in the refined structural details provided in Table 3.1. However, compared to O-atoms in the structure, Bi-atoms scatter X-rays very strongly. As a result, using PXP techniques, very little data can be derived directly about the O-atoms. The oxygen positions and occupancies listed in Table 3.1 are therefore not very accurate.

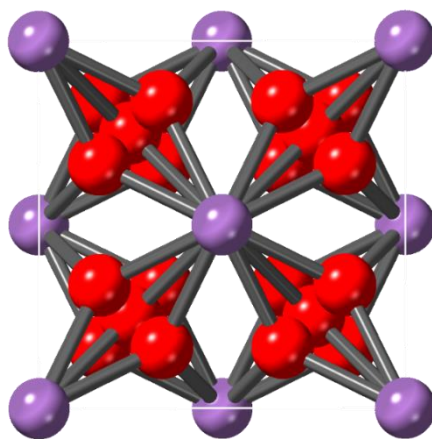
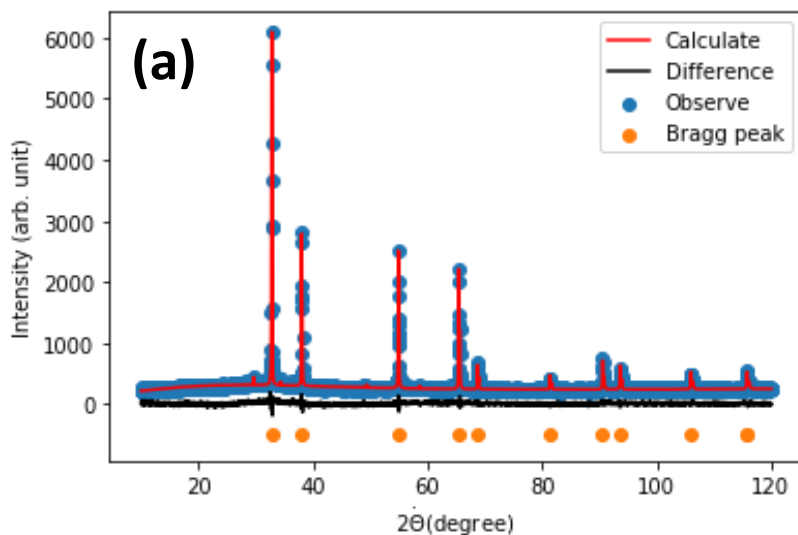


Fig. 3.4 The structure of 1.5Pb25YSB viewed along [100], where the red spheres represent O and the violet spheres represent Bi/Pb/Y. With oxygen atoms located at $8c$ ($\frac{1}{4}, \frac{1}{4}, \frac{1}{4}$) and $32f$ (x, x, x) interstitial sites.



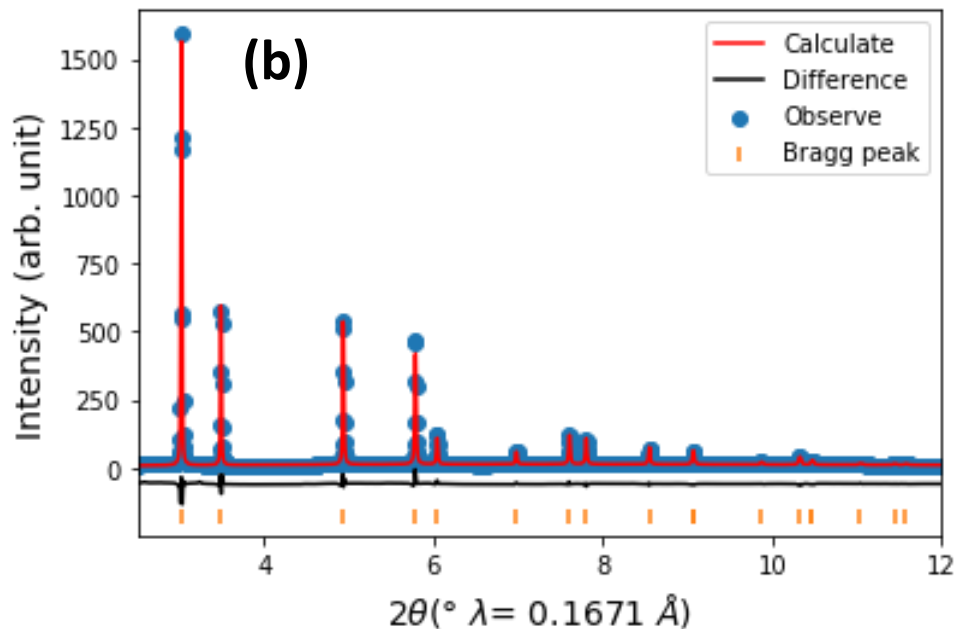


Fig. 3.5 Observed and calculated laboratory (a) and synchrotron(b) diffraction patterns for 1.5Pb25YSB composition. The blue circles in the figure indicate the experimental data while the red solid line is the Rietveld fit. The orange lines represent the positions of the predicted peaks. The lower plot (represented by a black line) is the difference curve between the observed and calculated diffraction profiles. The fitted background has been subtracted from both the observed and calculated intensities for clarity.

Table 3.1 Input values used during a Rietveld refinement analysis $\text{Bi}_{0.75(1-x)}\text{Pb}_{0.75x}\text{Y}_{0.25}\text{O}_{1.5-0.375x}$.

Atom	Site Symmetry	x	y	z	Thermal parameter	Fractional Occupancy
Bi	4a	0	0	0	1.588	0.735
Pb	4a	0	0	0	0.1473	0.015
Y	4a	0	0	0	0.3799	0.25
O1	8c	0.25	0.25	0.25	2.989	0.525
O2	32f	0.329	0.329	0.329	3.000	0.055

Fig. 3.5a exhibits the refined laboratory XRD pattern of composition 1.5Pb25YSB while Fig. 3.5b shows refined synchrotron XRD diffractogram of the same sample obtained from Rietveld analysis, using a whole profile fitting DIFFRAC.TOPAS suite. The crystallite size and strain broadening of the experimental profiles were both carried out individually using the pseudo-Voigt (pV) function. A polynomial function of degree five was used to match the background of each XRD profile. The reliability index parameters, such as expected error (R_{exp}) and weighted residual error (R_{wp}), were used to monitor the minimization.

The calculated lattice parameter (a) and the goodness of fit parameters from Rietveld analysis at room temperature for the range of compositions are listed in Table 3.2. This table shows that values of the lattice parameter for doped compositions are lower than that of δ -Bi₂O₃ ($a = 5.6525 \text{ \AA}$)⁹, which is due to the fact that the ionic radius of the major dopant, Y³⁺ (1.019 \AA)⁹ is less than the ionic radius of Bi³⁺ (1.17 \AA)⁹ regardless of the ionic radius of the minor dopant, Pb²⁺ (1.29 \AA)⁹ being greater than that of Bi³⁺ for the octahedral arrangement.¹⁰ The lattice parameters obtained from synchrotron data seems to be comparable to the ones obtained from the laboratory source but the values of goodness of fit for laboratory data are more than two times higher than the ones from synchrotron data highlighting the importance of high resolution data with less peak to noise ratio.

Table 3.2 Refined structural parameters for the (BiO_{1.5})_{0.75-x}(PbO)_x(YO_{1.5})_{0.25} system at room temperature using the cubic model with space group *Fm-3m*. R_{wp} is the weighted pattern residual and R_{exp} is the minimum achievable pattern residual, both of which are satisfactory values. Unfortunately, we could not measure the synchrotron data for 7.5Pb25YSB and 9Pb25YSB.

Sample	Laboratory data				Synchrotron data			
	$a(\text{\AA})$	R_{exp} (%)	R_{wp} (%)	GoF	$a(\text{\AA})$	R_{exp} (%)	R_{wp} (%)	GoF
1.5Pb25YSB	5.4877(8)	5.64	6.53	1.16	5.4939(3)	21.9	8.84	0.403
3.75Pb25YSB	5.4863(4)	5.96	7.55	1.27	5.4948(7)	21.0	10.0	0.478
7.5Pb25YSB	5.4835(8)	6.06	9.45	1.56				
9Pb25YSB	5.4807(9)	5.71	6.68	1.17				
15Pb25YSB	5.4750(2)	5.82	6.72	1.15	5.4854(5)	21.8	8.83	0.405

Vegard's law¹⁰ states that for a substitutional solid solution the unit cell parameters should vary linearly with composition (or extent of substitution) expressed in mol percentage. This linear relationship is seen in Fig. 3.6, but a decrease in lattice parameter was observed with an increase in Pb^{2+} content, for a fixed Y^{3+} dopant concentration. This was initially not anticipated due to the replacement of Bi^{3+} by the larger cation Pb^{2+} , but it is consistent with observations previously recorded by Omari *et al.*¹ which shows a similar compositional dependence of the cubic lattice parameter for the series $\text{Bi}_{0.75(1-x)}\text{Pb}_{0.75x}\text{Y}_{0.25}\text{O}_{1.5-0.375x}$ at room temperature. This contraction can be explained by the reduction in the amount of oxide ions associated with preserving electroneutrality. With an increase in Pb material, the highest intensity diffraction peak shifts to higher 2θ values (Fig 3.2a), suggesting changes in lattice parameters.

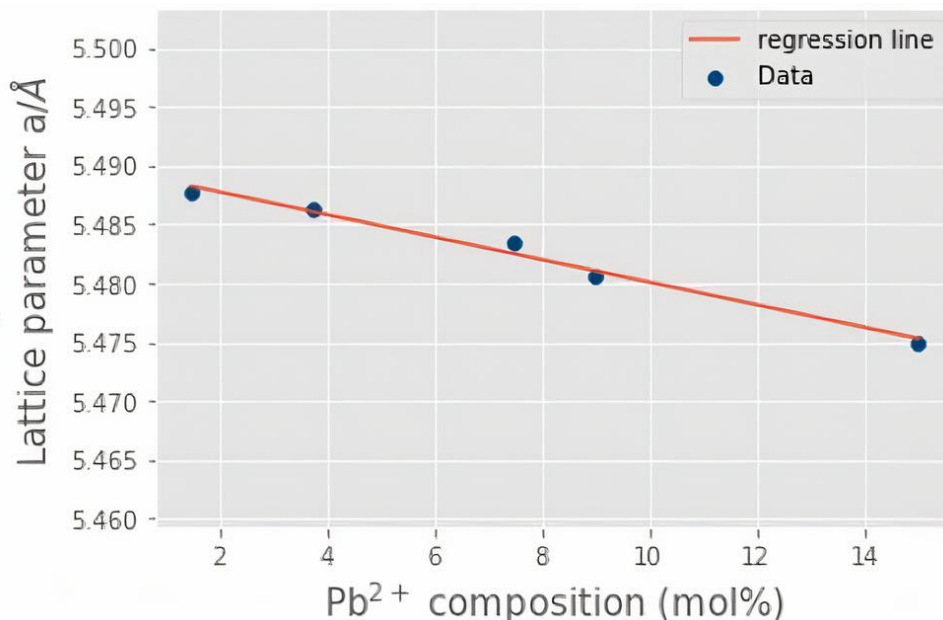


Fig. 3.6 Compositional modification of the $(\text{BiO}_{1.5})_{0.75-x}(\text{PbO})_x(\text{YO}_{1.5})_{0.25}$ cubic unit cell parameter at room temperature with Y^{3+} composition (25 mol%) kept constant.

The substitution of Pb on the Bi-site does not change the crystal structure itself but results in a shift in the relative atomic O_2-32f positions, which in turn affects the lattice parameters.

Furthermore, the change in oxygen occupancy, which could not be precisely determined via XRD, is another factor influencing the lattice parameters.

3.1.2. Lower total dopant concentration

To produce higher oxide conducting electrolytes, the dopant concentration should be decreased, but the total concentration still needs to be high enough to stabilise the pure fluorite $\delta\text{-Bi}_2\text{O}_3$ phase. To find the ideal PbYSB composition with lower total dopant concentration (concentrations from 10 – 20 mol% were considered) and the ratio of dopant content was varied, mainly looking at Pb:Y of 1:4, 1:2, 1:1 and 2:1.

Fig. 3.7 shows XRD patterns of different compositions of annealed PbYSB at 700°C. None of these compositions (with a total dopant concentration from 10 – 15 mol%) produced a pure cubic phase, instead a mixture $\delta\text{-}$ and $\beta\text{-Bi}_2\text{O}_3$ phases was obtained. This shows that the total dopant concentration and dopant ratio affect the purity of the phase of PbYSB compositions. The secondary phases of samples in Fig. 3.7 were analysed as mixtures of a cubic and tetragonal phase.

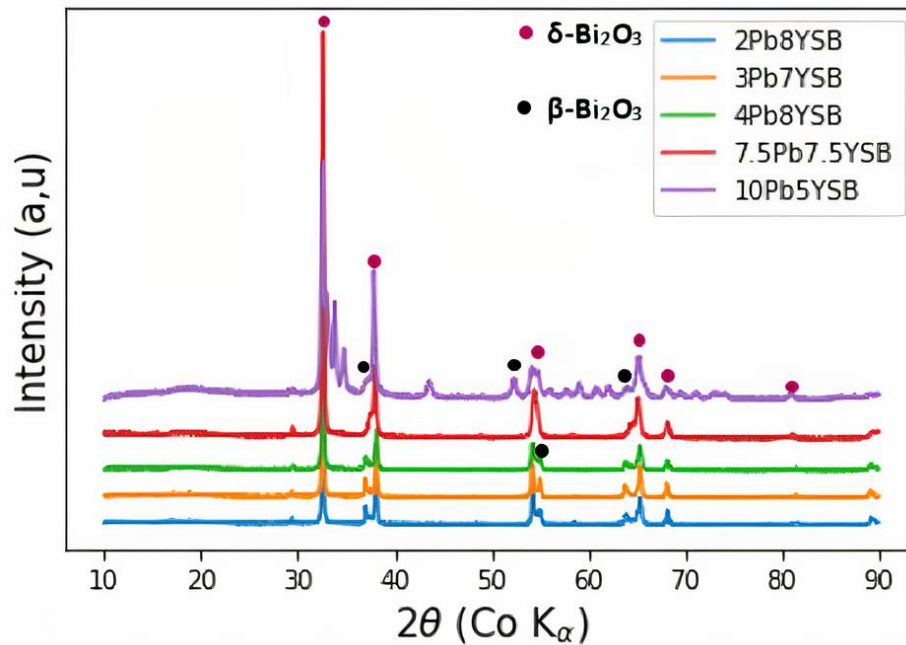


Fig. 3.7 The XRD patterns of samples of lower total dopant concentration, displaying a mixture of phases.

The indexed diffraction peaks represent the two phases that have been identified. The peak at ~ 30 2θ for all compositions corresponds to the $K_{\alpha 1}$ and $K_{\alpha 2}$ response. The $K_{\alpha 1}$ and $K_{\alpha 2}$ doublet will almost always be present; however, they overlap heavily at low angles resulting in one peak being observed but are more separated at high angles. The impurity peaks at ~ 36 , ~ 55 , ~ 64 2θ in Fig. 3.7 (black dots), corresponds to the tetragonal β -phase with the $P421c$ space group. The 10Pb5YSB sample in Fig. 3.7, the only sample with more Pb than Y dopant in it, had more unidentified impurities than the other samples, with the cubic phase being dominant.

To achieve a single cubic phase in a Bi_2O_3 double doped system, it appears that the Y content is thus required to be larger than the Pb content. Based on the above findings, PbYSB electrolytes with different Pb:Y dopant ratios were then prepared (3Pb9YSB, 5Pb10YSB, and 5Pb15YSB). The total concentration of dopants ranged from 12 – 20 mol%. The annealing temperature also played a role as it was observed that at lower dopant concentration, high annealing temperature (750°C) is required.

The XRD patterns of these PbYSB electrolytes are shown in Fig. 3.8. This indicates that for all compositions the cubic fluorite structure with space group $Fm-3m$ was stabilized. Looking at Fig. 3.8a, the width of the peaks increase as dopant concentration decreases due to different crystallite sizes, suggesting that 12% doped composition had more of the Tetragonal phase than the other two doped composition. Since literature indicates that lightly doped Bi_2O_3 based electrolytes possess greater ionic conductivity¹², the focus was turned to the 15% doped composition and with varied concentrations of Pb^{2+} and Y^{3+} keeping total dopant concentration fixed at 15%, to find out the best Pb:Y dopant ratio.

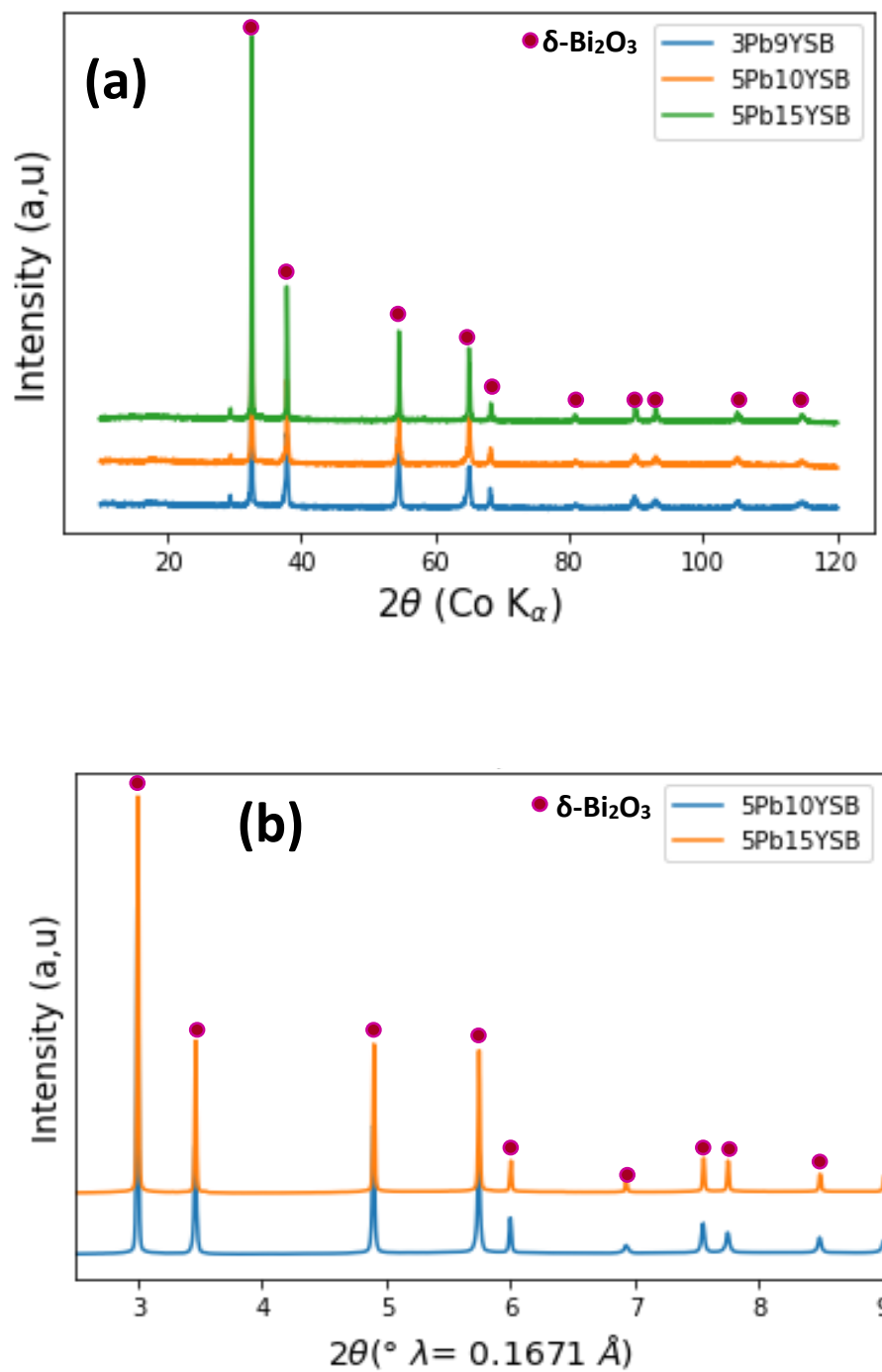


Fig. 3.8 Laboratory XRD diffractograms for 3Pb9YSB, 5Pb10YSB and 5Pb15YSB (a), synchrotron diffractograms for 5Pb10YSB and 5Pb15YSB (b), we could not measure the synchrotron data for 3Pb9YSB. All samples were annealed at 750°C for 16 hours.

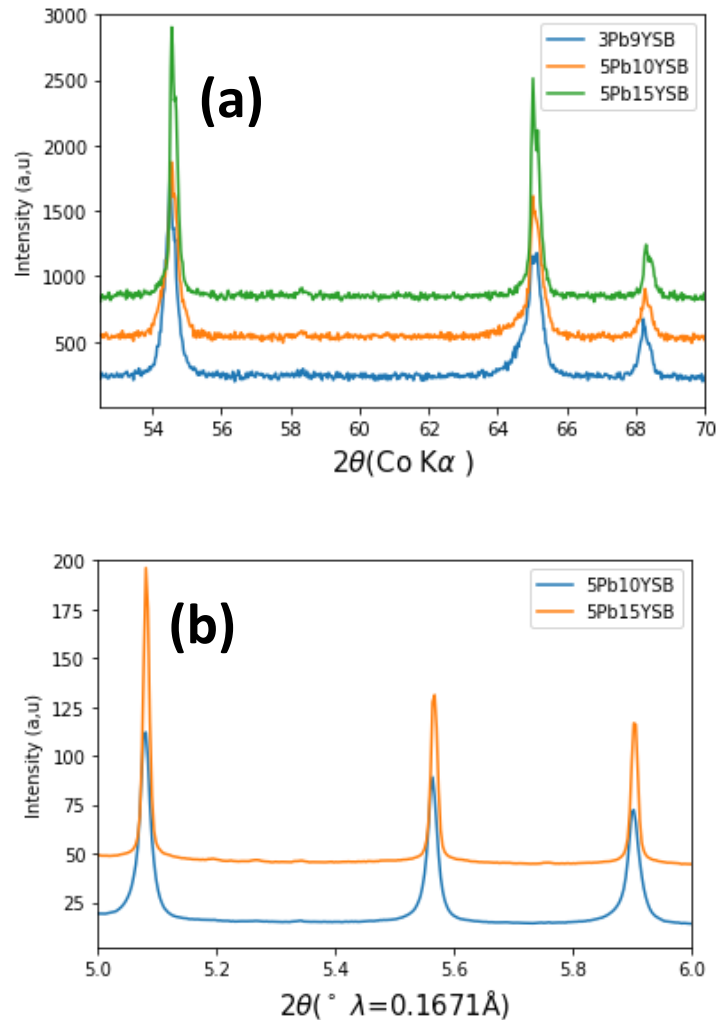


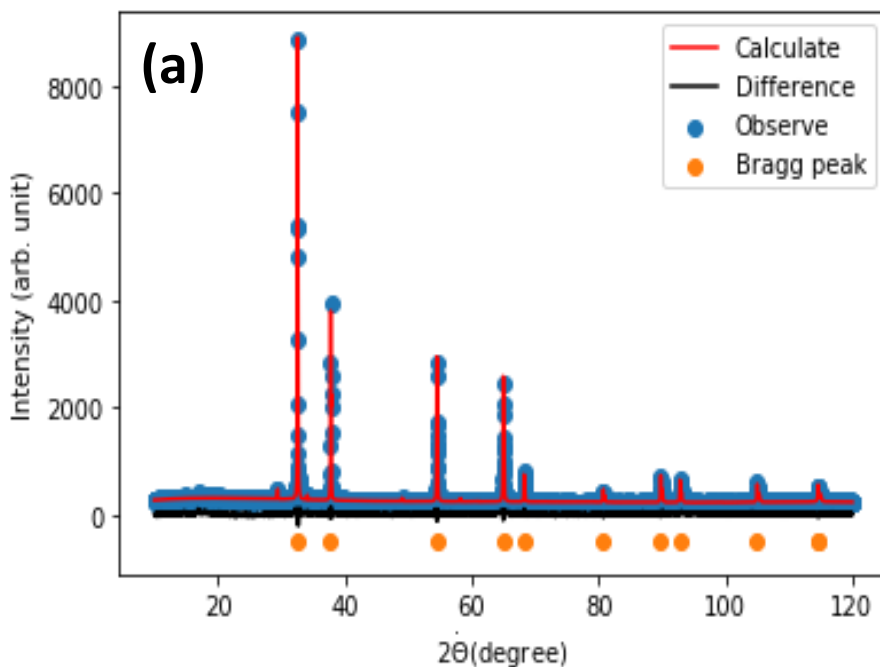
Fig. 3.9 Diffractograms showing (a) laboratory XRD patterns annealed (at 750 °C) for 3Pb9YSB, 5Pb10YSB and 5Pb15YSB material and (b) synchrotron XRD data all measured at 25 °C.

The peak below 60 in Fig. 3.9a is broader for low dopants, but still symmetrical. The peak above 60 is also broader for low dopants, but asymmetrical. The strength of having the synchrotron data is then to show that with high resolution the asymmetric peak did not resolve into two separate peaks, thus providing better evidence that there is probably only a single-phase present. Although here the peak is still broader for lower dopant concentration. This highlights the limitations of PXRD data collected at BNL as it is not a true high-resolution beamline, but it has a better resolution than the lab instrument.

The same Rietveld refinement analysis as before was also conducted on lower dopant samples. Rietveld refinement of the powder X-ray diffraction data for lower dopant samples converges to a satisfactory solution in space group $Fm-3m$ of the cubic system (Table 3.3). The goodness of fit values obtained are higher than the ones obtained in Table 3.2, highlighting the existence of mixture of phases at room temperature. 3Pb9YSB sample has a higher GoF value indicating that out of the three it is the least stable sample. The Rietveld refinement of XRD patterns was performed using a Bruker AXS TOPAS-Academic V.6 resulting in an agreement between the experimental and calculated patterns, which can be seen from their difference depicted in blue line, as shown in Fig. 3.10.

Table 3.3 Structural parameters for 5Pb10YSB obtained from Rietveld refinement of powder X-ray diffraction data at room temperature. Atomic positions (refer to table 3.1) space group $Fm-3m$ of the cubic system.

Sample	Laboratory data				Synchrotron data			
	a(Å)	R _{exp} (%)	R _{wp} (%)	GoF	a(Å)	R _{exp} (%)	R _{wp} (%)	GoF
3Pb9YSB	5.5236 (7)	5.95	9.32	1.57	5.5629 (3)	5.16	12.2	2.36
5Pb10YSB	5.5199 (2)	5.88	7.13	1.21	5.5326 (5)	5.29	9.27	1.75
5Pb15YSB	5.5223 (5)	5.63	7.15	1.18	5.5137 (6)	5.16	7.51	1.45



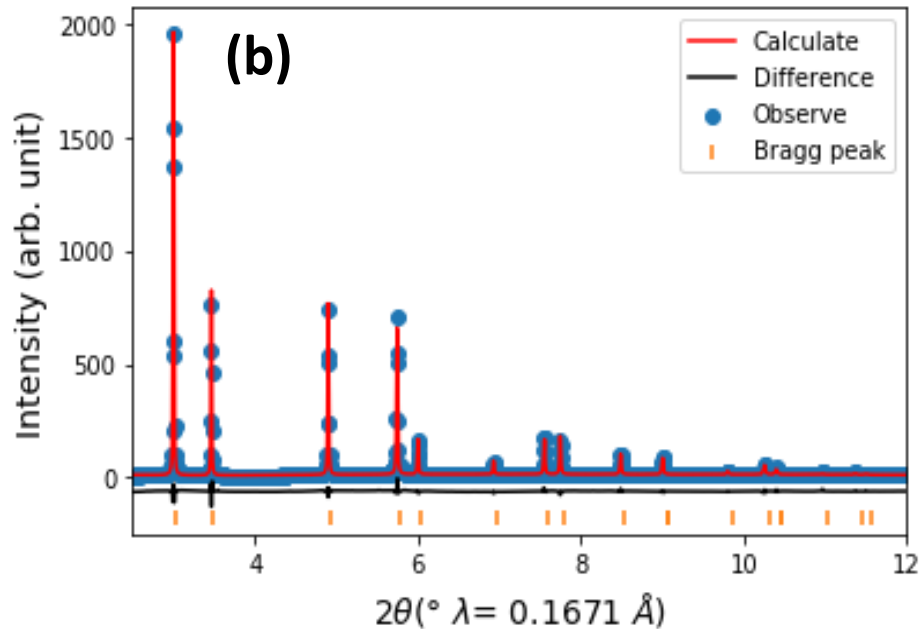


Fig. 3.10 Rietveld refinement plots for 5Pb10YSB at room temperature for laboratory (a) and synchrotron XRD (b) diffraction profiles. The observed (blue dots) and calculated (red solid line) data is given as well as the difference plots. The orange symbol shows the positions of the allowed Bragg reflections in space group $Fm\bar{3}m$.

3.2. Variable temperature-PXRD studies

In order to analyse the phase behaviour and stability of these materials as they are heated and cooled, two samples were looked at, namely, 5Pb10YSB and 1.5Pb25YSB, i.e. one in the low and one in the high dopant range, due to limitations in access to state-of-the-art techniques, such as, Synchrotron Powder X-ray Diffraction and Raman Spectroscopy (RS). This was undertaken using variable temperature (VT)-PXRD. Fig. 3.11 displays stacked diffraction patterns during the heating cycle for VT-PXRD measurements of 1.5Pb25YSB. The stacked diffractograms showed no peak asymmetry or peak broadening across the studied temperature range (30 -780 °C) with no major change (peak splitting or the appearance/disappearance of peaks) being observed, indicating that there are no structural phase transitions in this temperature range (Fig 3.12). This clearly demonstrated the stability of the highly doped sample up to 780 °C. The main reason for peak shift to lower angles as the sample is heated is due to increase/decrease in the crystal lattice that is reflected by the shift of diffraction peaks.

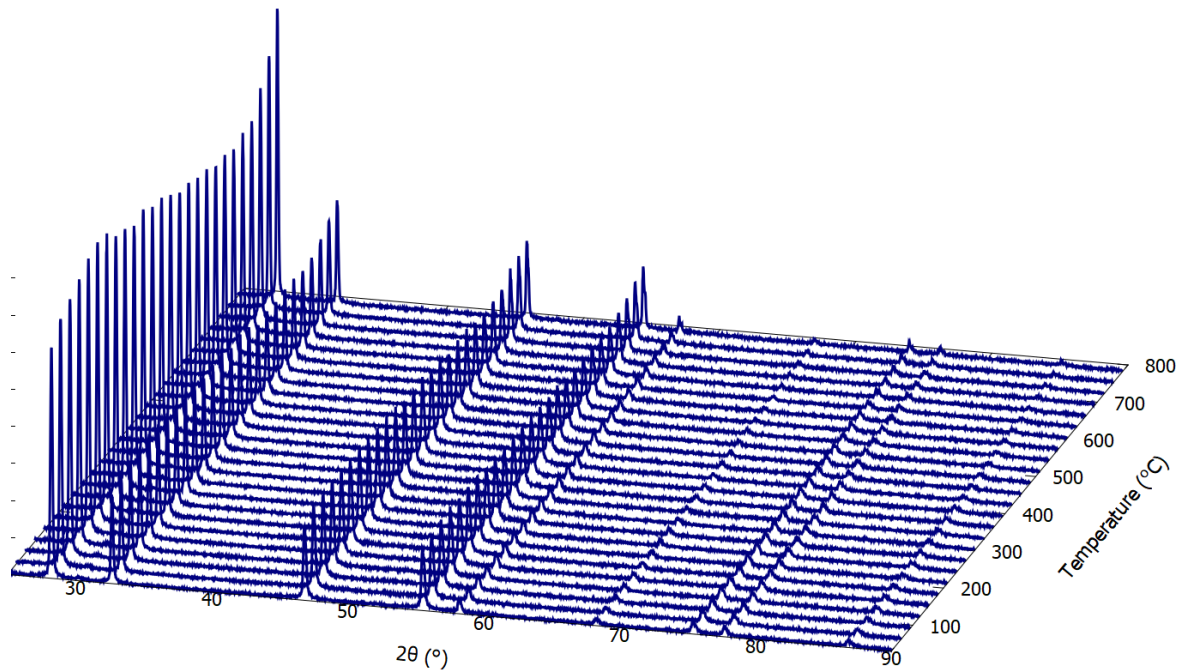


Fig. 3.11 Stacked diffraction patterns for VT-PXRD measurements of 1.5Pb25YSB during the heating cycle, with the top perspective focusing on the higher angle data.

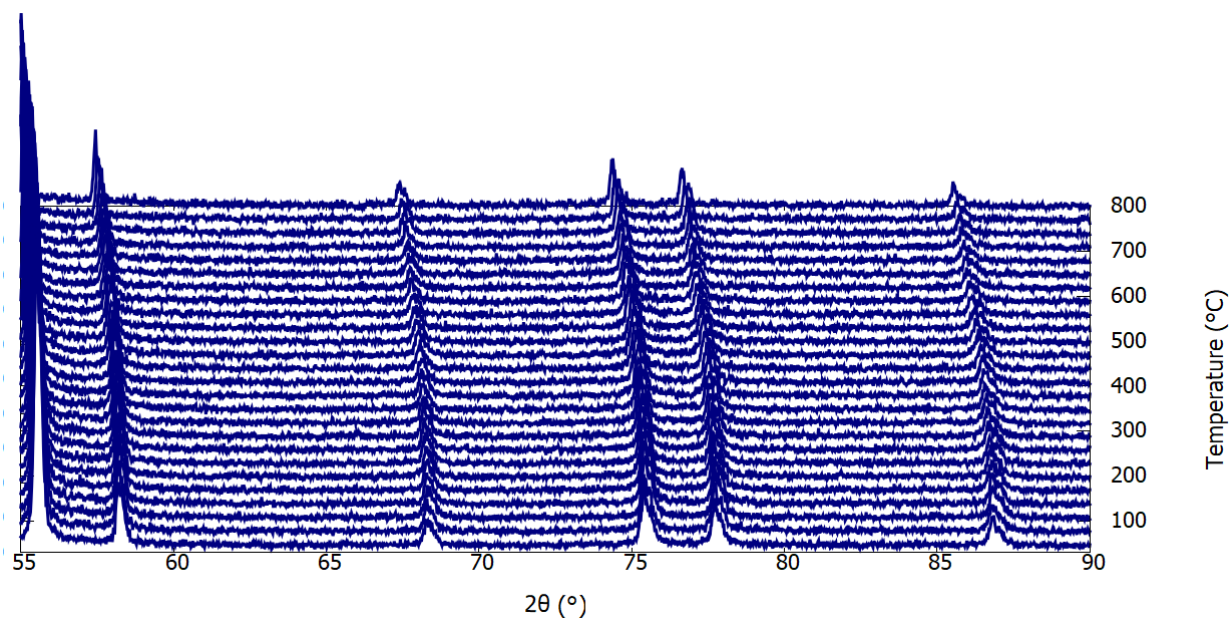


Fig. 3.12 Zoomed-in, *In situ* diffractograms collected for 1.5Pb25YSB material annealed at 750 °C over the temperature range of 30-780 °C.

The VT-PXRD measurements for the 5Pb10YSB sample were done at the synchrotron. The diffractograms during the heating cycle are shown in Fig. 3.13. It is clearly seen from the stacked diffraction patterns that phase shift occurs upon heating. The sample appears to have a mixture of phases from the start, hence the broader peaks, but the peaks cannot be resolved. Only around 500 °C where the δ -phase starts to dominate, there is some kind of resolution between the two. From around 600 °C narrow peaks of the δ -phase are observed (Fig 3.14).

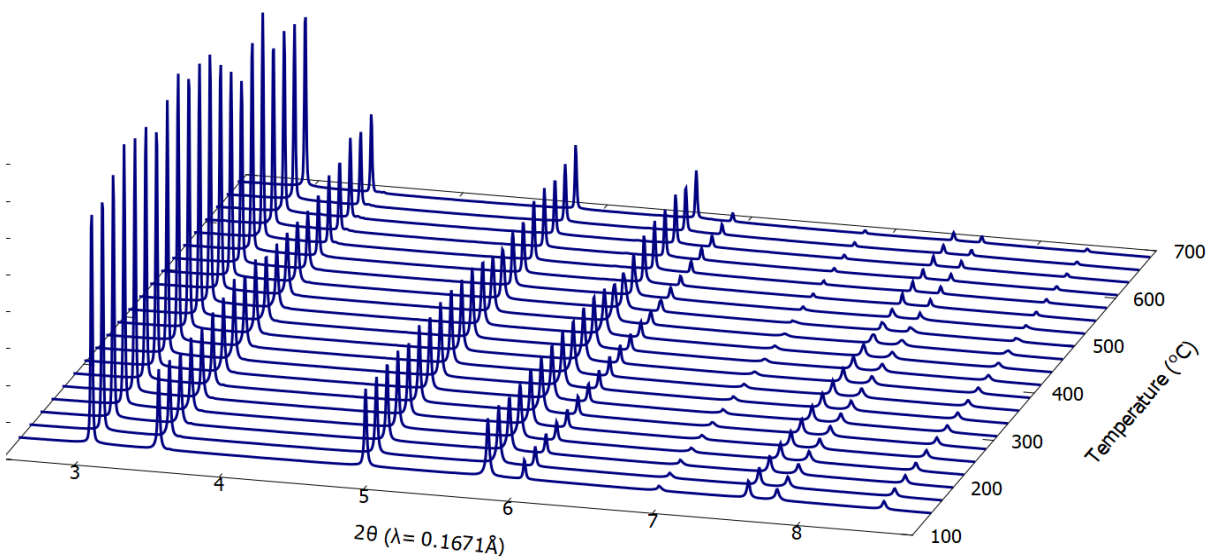


Fig. 3.13 Stacked diffraction patterns for VT-SCXRD diffractograms collected for the 5Pb10YSB material during the heating cycle in the temperature range of 25-683 °C.

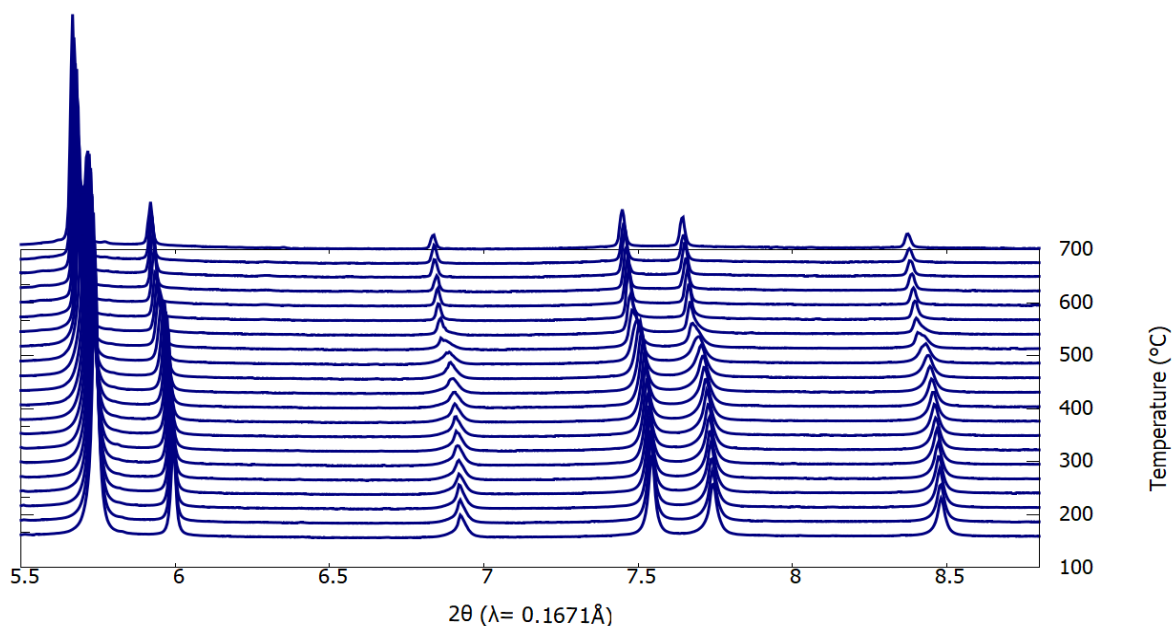


Fig. 3.14 Zoomed-in stacked diffractograms collected for annealed (at 750 °C) 5Pb10YSB material over the temperature range of 25-683 °C. The top perspective, again focusing on the higher angle data, clearly shows that there is some phase transformation occurring.

The existence of a secondary phase was confirmed with Rietveld refinement of the diffraction pattern for 5Pb10YSB at 468°C. A poorer fit ($R_{wp} = 11.44$, $GoF = 1.03$) was obtained when the defect fluorite-type δ -phase was used to fit the pattern at intermediate temperature (Fig. 3.15a). A much better overall fit ($R_{wp} = 10.31$, $GoF = 0.94$) was provided by the inclusion of the secondary β -phase for a multiphase Rietveld refinement (Fig. 3.15b), which also revealed that the β -phase consisted of around one percent of the crystalline material at 468°C. The value is not accurate enough as it is difficult to get an accurate value when the sample has one phase a lot lower than the other. The same problem was encountered when trying to refine the room temperature data using both β - and δ -phases.

The defect fluorite-type δ -phase alone was adequate to provide an excellent fit at high temperatures (Fig 3.15c). For some of the peaks, peak "reorientation" occurs where a shoulder becomes the main peak and the main peak becomes a shoulder, as illustrate in Fig. 3.15d in the temperature range of 468-548 °C where the phase change is more pronounced. Eventually, at high temperatures (548-683 °C), all shoulders disappear. This is highly likely due to the transition to the pure δ -phase, with no β -phase remaining at these high temperatures.

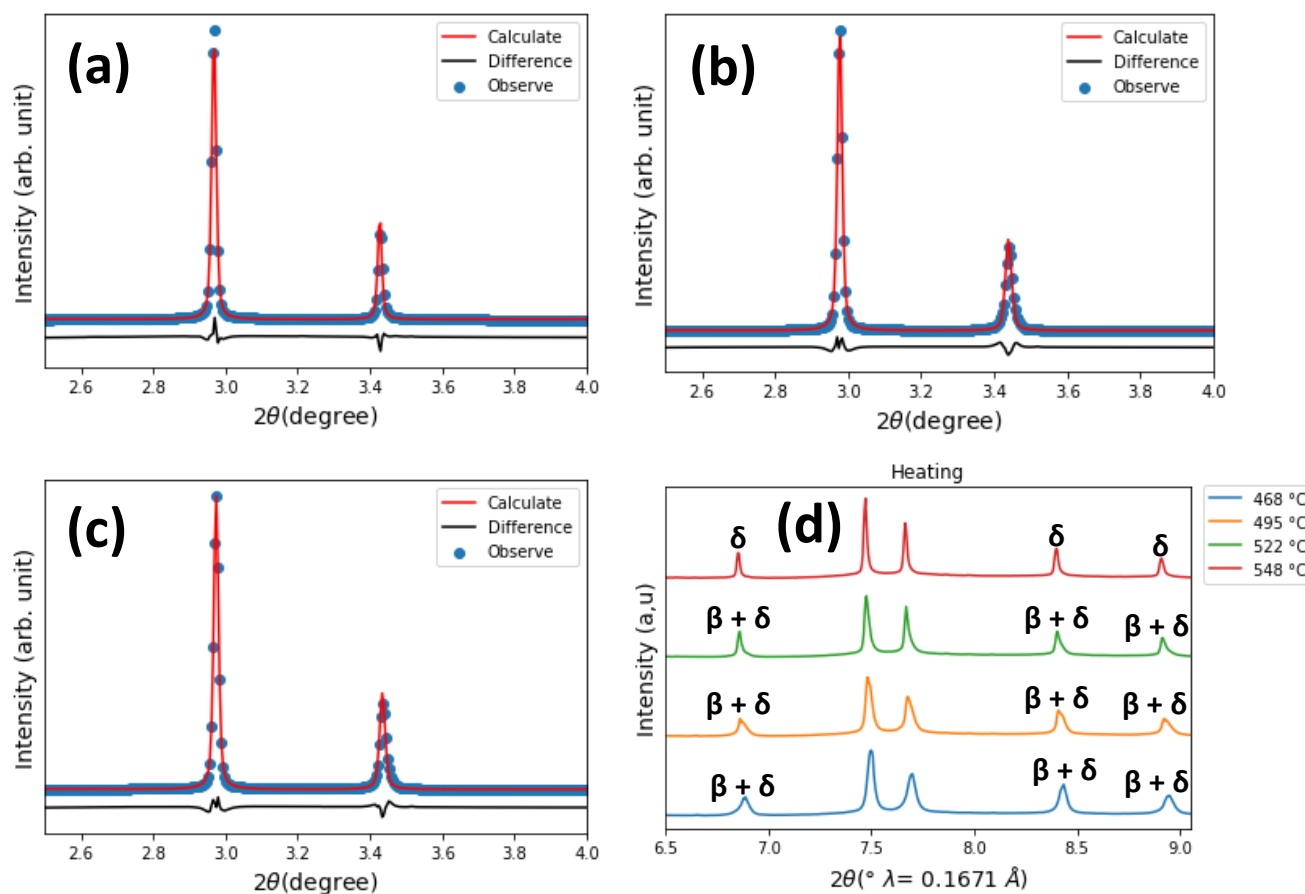


Fig. 3.15 Rietveld refinements of the diffraction patterns for 5Pb10YSB where the dots represent observed data, the red line shows the fit and black line is the difference curve. This was done by including (a) the δ -phase only at 468°C, (b) the mixture of δ - and β -phase at 468°C and (c) the single δ -phase at 683°C. (d) An enlarged view depicting how the shoulders transform to become the main peaks.

The observed change in diffraction patterns was less drastic during the VT-PXRD cooling run for 5Pb10YSB with only anisotropic peak broadening being apparent from around 468°C and an increase in intensity to varying extents for the different peaks (Fig. 3.16). This suggests an almost complete overlap of the peaks for the δ - and β -phase, as clearly seen in Fig. 3.15a and 3.15b respectively. Unfortunately, the resolution of these diffractograms did not allow for the peaks to be resolved even from measurements at the 28-ID-2 beamline at NSLSII, but it is evident from observing the overall stacked plot that a mixture of phases form again after cooling (Fig. 3.16 and Fig. 3.17).

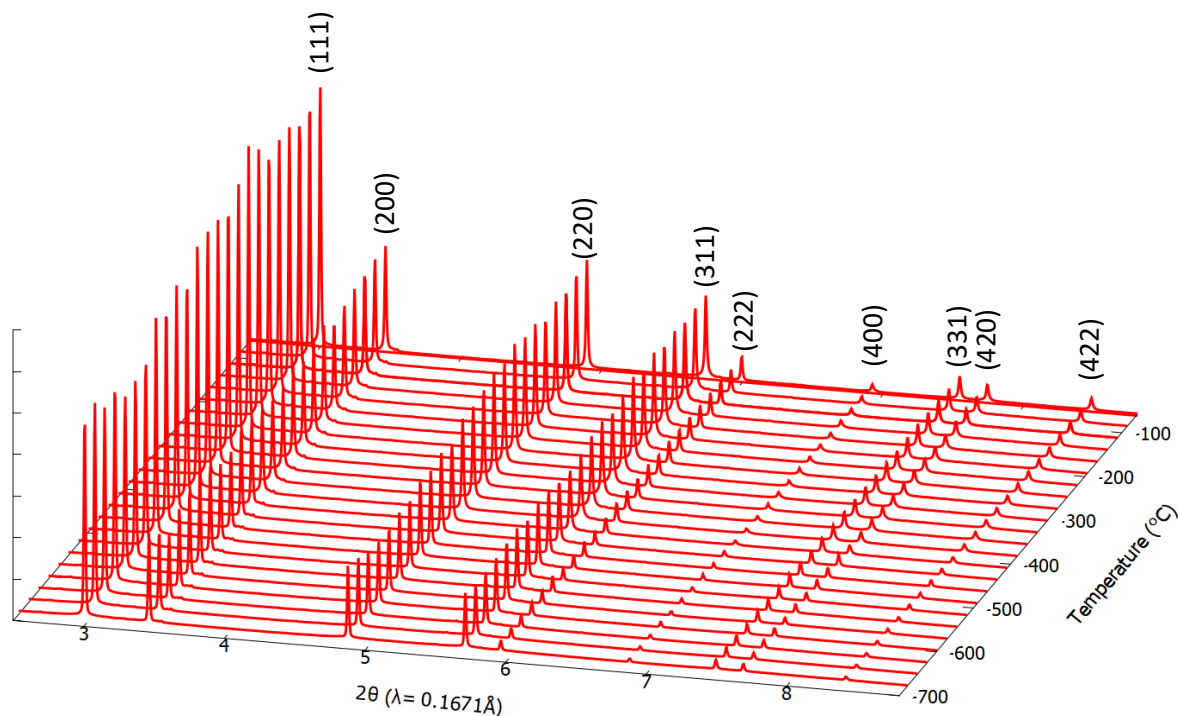


Fig. 3.16 Stacked diffraction patterns for VT-SCXRD measurements of 5Pb10YSB showing anisotropic peak broadening from about 468 °C during the cooling cycle. Indexing only applies to the pure δ -phase above 548 °C.

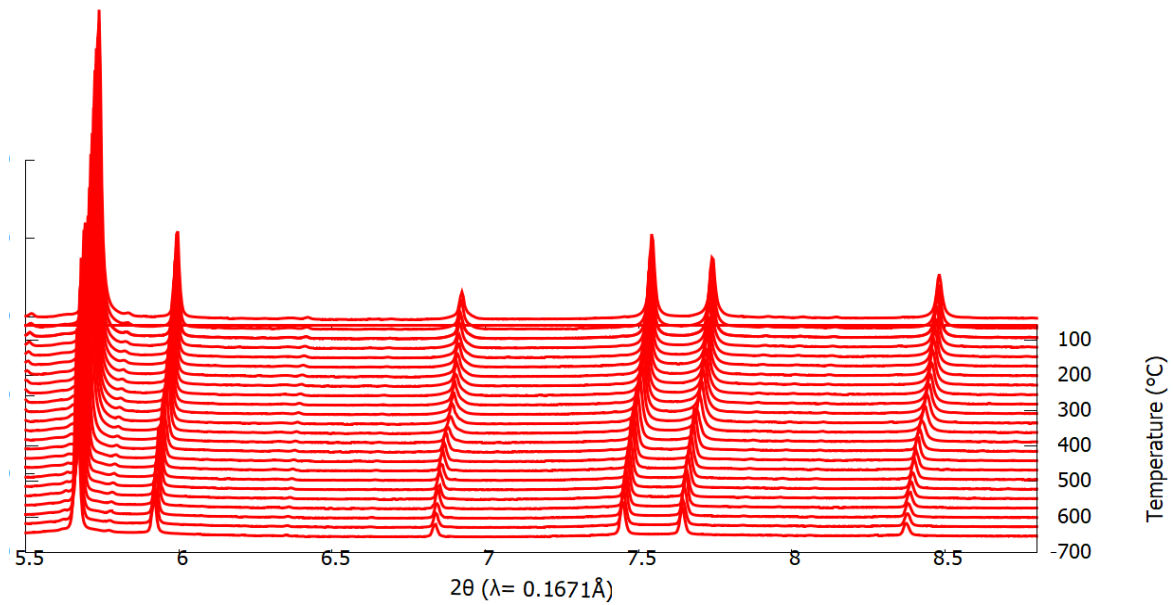


Fig. 3.17 Zoomed-in, *In situ* diffractograms collected for an annealed (at 750 °C) 5Pb10YSB material over the temperature range of 683-25 °C.

Fig. 3.18 shows the relationship between the lattice parameter and temperature for both samples that were analysed by VT-XRD. As expected, a temperature increase is shown to result in an increase in the a parameter, but the relationship is not linear throughout. The heating and cooling profiles can essentially be divided into three linear regions.

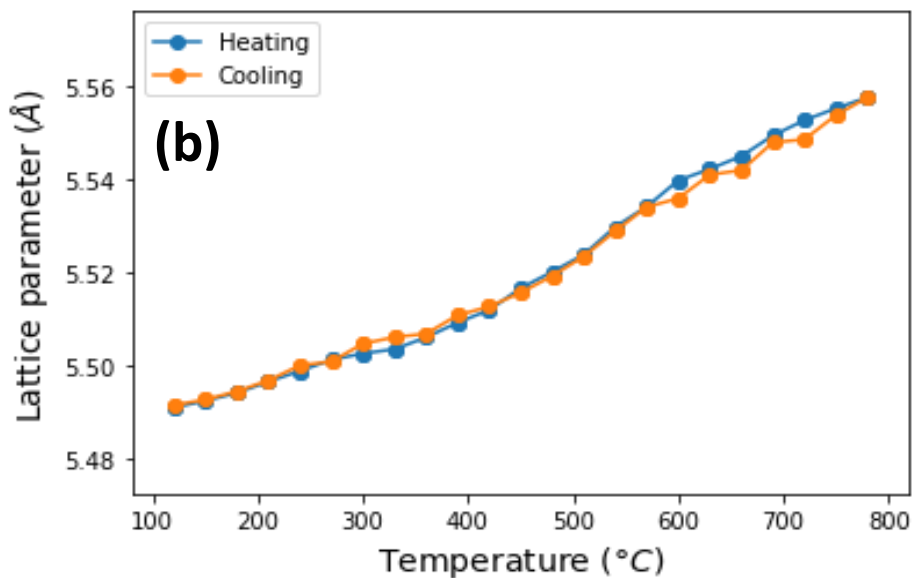
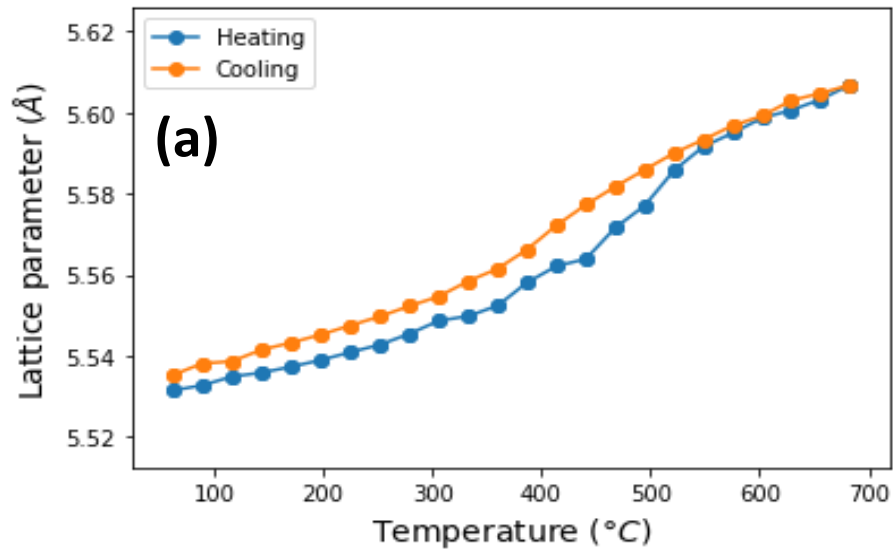


Fig. 3.18 Thermal variation of the cubic lattice parameter, a , from Rietveld analysis of (a) SCXRD for 5Pb10YSB and (b) laboratory XRD data for 1.5Pb25YSB on heating (blue line) and cooling (orange line).

Based on the observation from the XRD data, it is not surprising to see these three regions for the 5Pb10YSB sample. The linear region up to ca. 350 °C reflects a mixed phase although the data was refined as though it were a pure δ -phase, thus it is questionable what this lattice parameter

really represents. The second region extends up to ca. 550 °C, where the transition from a mixture to a single phase occurs. It is only above ca. 550 °C where the pure δ -phase exists. On cooling, the profile matches that on heating down to ca. 550 °C, but below this temperature the values for the lattice parameter are slightly larger than those observed on heating. This is not surprising since the diffraction patterns differ on the heating and cooling cycles and again, the data was refined using a pure δ -phase whereas we now know this is not the case.

It was surprising to see a similar curve which could be divided into the three regions for the 1.5Pb25YSB sample (Fig 3.18b), although the change was far less pronounced. The second steeper region is observed in the same temperature range (ca. 350 - 550 °C). This raises the question as to whether the 1.5Pb25YSB sample is truly a pure phase or if it contains a very small amount of the β -phase which is then totally converted to the pure δ -phase at higher temperatures. Alternatively, this could be an artefact of the data refinement process. The heating and cooling cycles give essentially the same results indicating that the process is reversible. This needs to be further investigated. In all samples, refinement involved the sequential variation (values of all the parameters from the Rietveld refinement of a preceding pattern are used as starting values for the next pattern) of scale factor, background coefficients, unit-cell parameters, specimen displacement correction, peak-width parameters, and pseudo-Voigt profile function coefficients.

Selected annealed samples were studied *in situ* to determine the phase stability and thermomechanical properties of the materials during a thermal cycle. For the 5Pb10YSB material (Fig 3.18a) interesting features are evident. Upon heating, the starting cubic phase expands linearly within the range of 62-360°C (Fig 3.18a and Table 3.4) however, over the range of 441-549°C the lattice expands rapidly (abrupt peak shift accentuated in Fig. 3.18a). Over the range of 549-683°C, the rate of thermal expansion is again uniform although significantly increased. On cooling a similar, reversed trend is observed; between 683-495 °C the thermal expansion is linear, over the range of 495-306 °C the lattice contracts rapidly (Fig. 3.17) and between 306-27 °C the thermal expansion is again linear and significantly reduced in magnitude (Fig. 3.18a and Table

3.4). For the 1.5Pb25YSB material (Fig. 3.12), the rate of thermal expansion is linear for both the heating and cooling cycles (Fig. 3.18b and Table 3.4) and there exists no abrupt changes in the unit cell volume (Fig. 3.18b). This indicates that higher dopant percentages promote the retention of a pure cubic sample after a thermal cycle and enable significantly more controlled thermal expansion behavior.

Table 3.4 Thermal expansion behavior of the annealed (at 750 °C) 5Pb10YSB and 1.5Pb25YSB materials over the temperature range of 27-706-27 °C. Values below indicate a steeper slope.

5Pb10YSB		1.5Pb25YSB	
Temperature (°C)	CTE (10^{-6} K^{-1})	Temperature (°C)	CTE (10^{-6} K^{-1})
62-360	70.0 ± 3.1		
441-549	303.2 ± 1.2	360-780	100.3 ± 3.5
549-683	101 ± 7.5		
683-495	105 ± 2.7		
495-306	200.3 ± 1.4	780-360	102.5 ± 2.9
306-27	80.7 ± 1.8		

3.3. DTA/TG analysis

DTA was employed to trace any phase changes in the low dopant sample, 5Pb10YSB and the high dopant sample, 1.5Pb25YSB. Heating and cooling cycles were followed in a temperature range between 30°C and 750°C or 800°C in nitrogen atmosphere. Fig. 3.19 shows a DTA scan for both the empty crucible and 1.5Pb25YSB sample measured from room temperature to 800°C. The difference between the two scans is shown in Fig 3.20a indicating a sloping baseline. On the DTA curve for 1.5Pb25YSB, any endothermic or exothermic peak was not observed in the range of between 30 and 800 °C as shown in Fig. 3.20a. This observation illustrated that the formed δ -phase sample is thermally stable up to 800 °C. This result was in agreement with the measured TG curves (Fig. 3.20b) as the mass change detected was insignificant until the heating temperature of 800 °C. A total mass loss of only about 1.2% (Fig. 3.20b) was recorded on heating while on cooling there is less than 0.2% change observed in the mass.

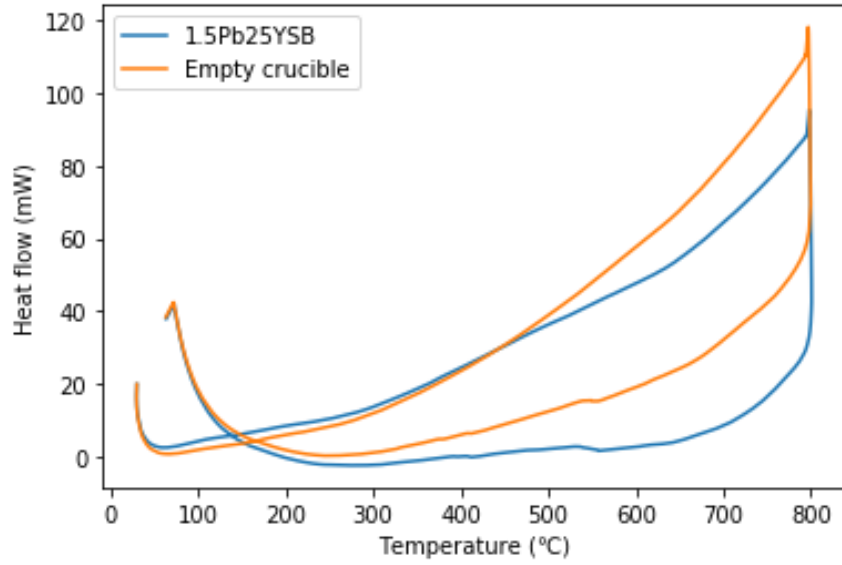
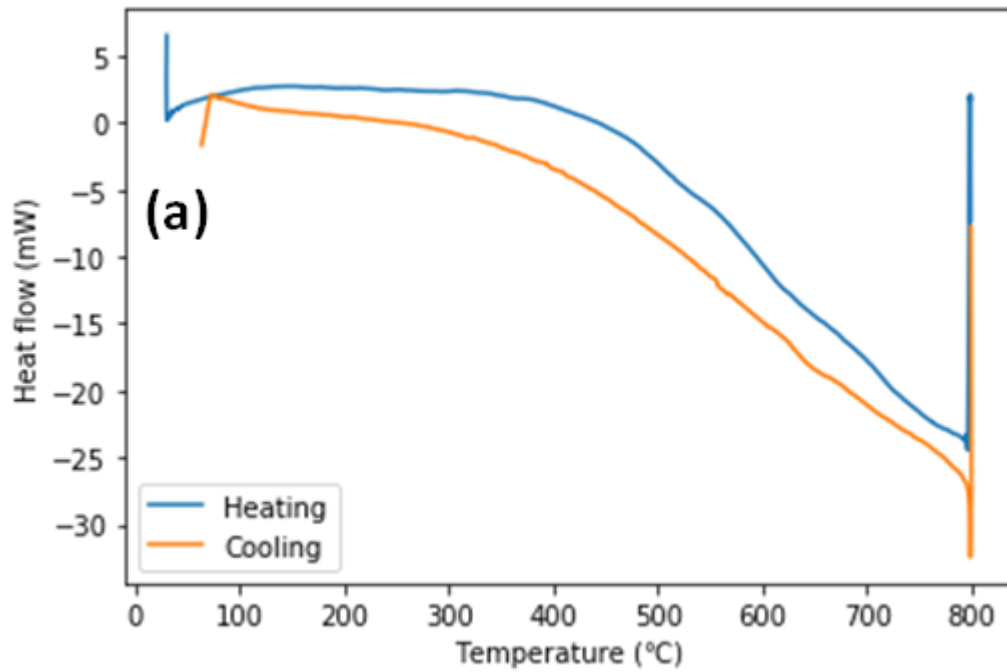


Fig. 3.19 DTA scans for an empty crucible and 1.5Pb25YSB material (annealed at 750°C) over the temperature 30-800°C.



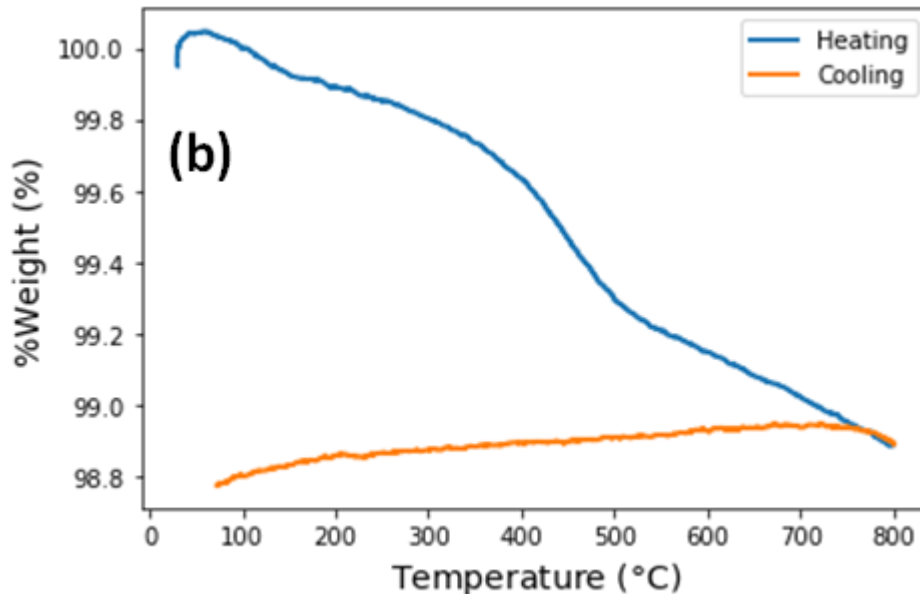


Fig. 3.20 DTA (a) and TGA (b) plots for 1.5Pb25YSB. Blue and orange solid lines show heating and cooling runs, respectively.

DTA and TGA diagrams of 5Pb10YSB are shown in Fig. 3.21 and show no gross thermal events. Nonetheless, a close examination of the thermograms in the region 450 to 650 °C (inset Fig. 3.21a), reveals two broad endothermic events upon heating. From the 5Pb10YSB DTA study, the temperatures for endothermic event maxima are ~480 °C and ~660°C, which tend to correspond to the transition temperatures between the three regions shown in the cubic lattice parameter thermal expansion. The endothermic peak at ~480 °C is caused by a phase transition from a mixture of $\delta + \beta$ -phase to δ -phase (in line with VT-XRD) whereas a second endothermic effect at ~590 °C or 660 °C is associated with order-disorder transition according to the references data.¹⁶⁻¹⁹ DTA thermograms were featureless upon cooling. The TGA reveals that on heating the samples begin to lose mass at ca. 350 °C, reaching ca. 530°C and then lose mass up to ca. 750 °C, with a total mass loss of only about 1.4% (Fig. 3.21b). On cooling there is less than 0.2% change observed in the mass.

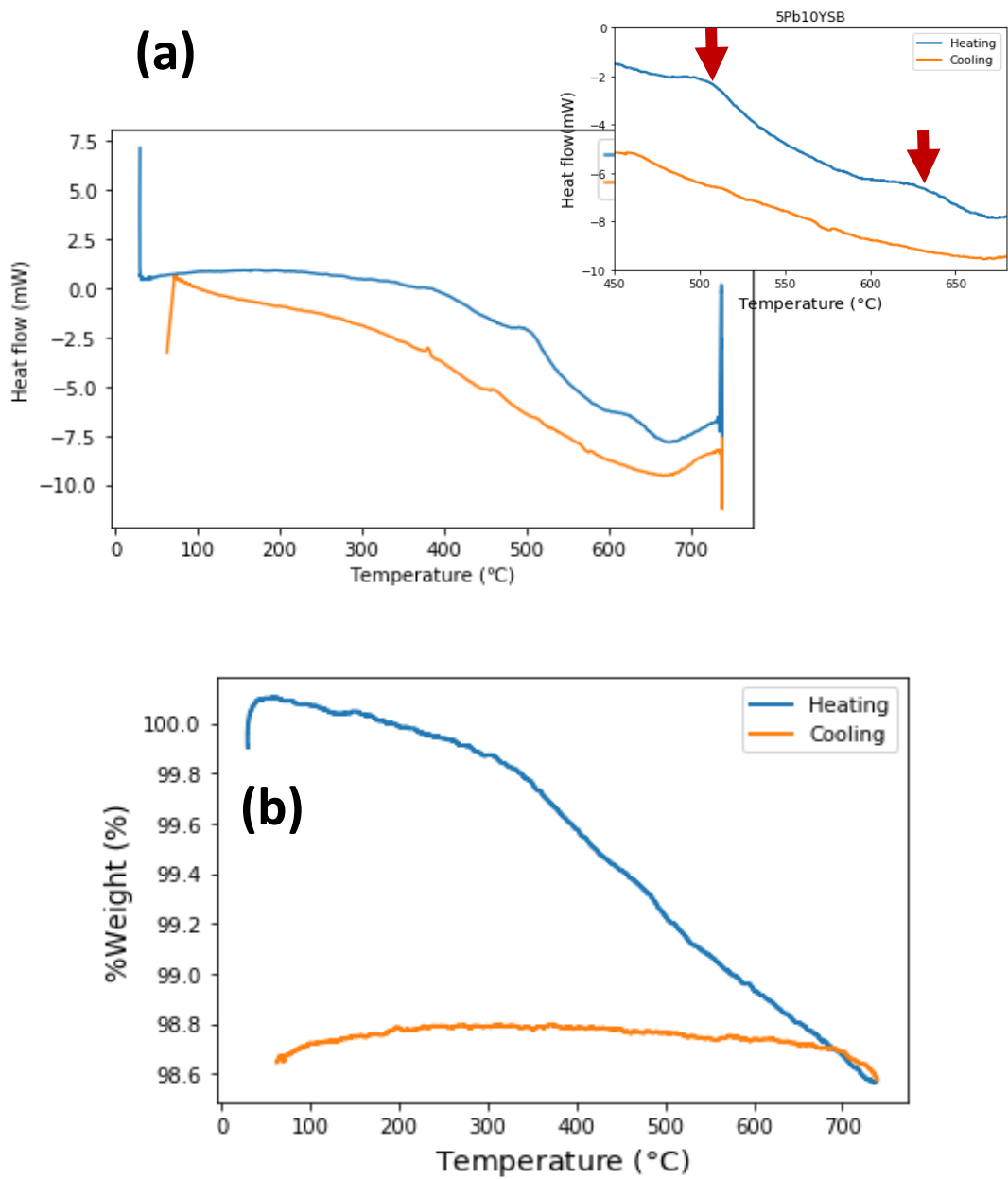


Fig. 3.21 Results for 5Pb10YSB showing the DTA thermogram (with enlarged detail of the profiles in the inset) (a) and TGA curves (b). Blue and orange solid lines show heating and cooling runs, respectively. The two arrows represent the two endothermic events, one at ~ 480 °C and ~ 60 °C.

3.4. Raman Spectroscopy analysis

To further investigate the structure and cause for the temperature dependant behaviour observed for both the 1.5Pb25YSB and 5Pb10YSB samples (by VT-PXRD and DTA), variable temperature-Raman spectroscopy (VT-RS) was used. Unlike conventional XRD which looks at the average structure, RS probes the local structure and is very sensitive to a mixture of phases.

Factor group theory predicts one Raman active band for a fluorite structure, the F_{2g} band from the oxygen sublattice. Indeed, one Raman band for a defect fluorite-type structure of doped and undoped bismuth oxide has been reported before. For example, Lee *et al.*¹⁸ observed a single peak at 600 cm^{-1} for erbium doped bismuth oxide (with $\text{Bi}_2\text{O}_3:\text{Er}_2\text{O}_3 = 4:1$) for the defect fluorite-type δ -phase when using an excitation line of 532 nm. The stacked Raman spectra of 1.5Pb25YSB at various temperatures (27-800°C) is shown in Fig. 3.22. All the spectra have similar features to that of δ - Bi_2O_3 , they show sharp bands below 200 cm^{-1} wavenumber attributed to external lattice vibrations¹⁸ and broad peaks at 600 cm^{-1} assigned to disorder in the structure as a result of the number of oxygen vacancies. This suggests that the δ -phase of the 1.5Pb25YSB sample was fully stabilized. Additionally, no change in the phase behaviour was observed upon heating. Note that the decrease in intensity of the peaks above is correlated to the variation in the lattice parameters. Therefore, as the number of oxygen vacancies change, the lattice expansion is affected as a consequence of the increased temperature.

It could be that since the sampling area in Raman spectroscopy is so small, the region chosen in the analysis was phase pure. All the other spots we looked at gave the same results but with less intensity of the peaks.

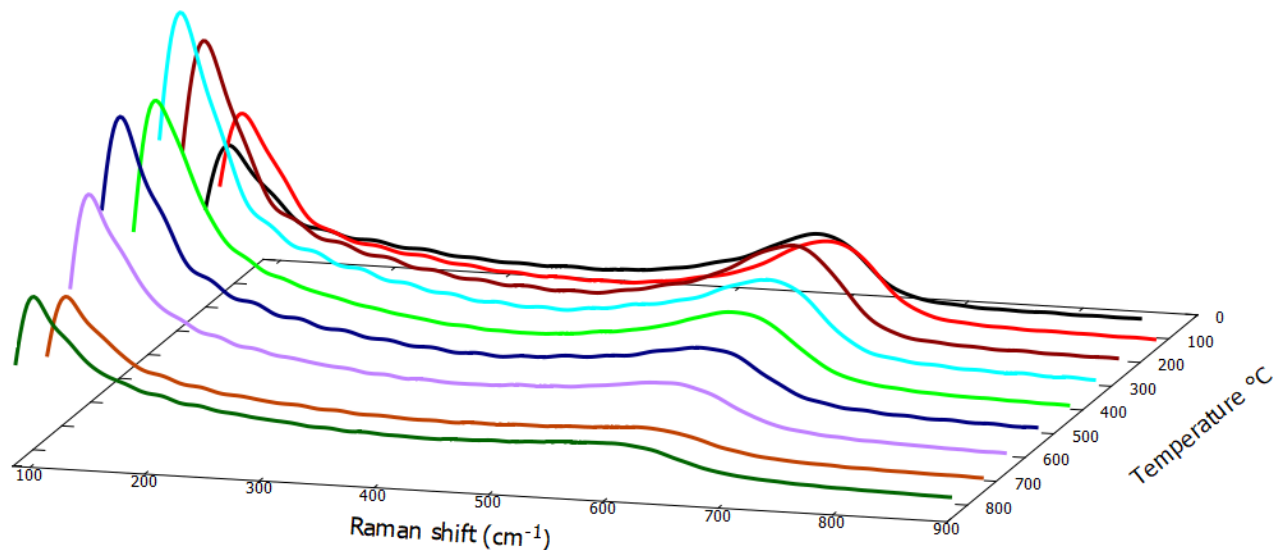


Fig. 3.22 Stacked Raman spectra of the 1.5Pb25YSB sample taken during the heating cycle.

The spectra for the 5Pb10YSB exhibited Raman bands additional to that for the defect fluorite-type δ -phase at lower temperatures as shown in Fig. 3.23. This clearly reinforces the idea that there is a mixture of phases and that the cubic phase was not truly stabilised at intermediate temperature. The proposed deduction that the broader peaks observed at the lower temperatures in the XRD patterns for this sample was due to an unresolved mixed phase is thus supported.

Hardcastle and Wachs¹⁹ observed peaks at 124 cm^{-1} , 311 cm^{-1} and 462 cm^{-1} for the β -phase using the same excitation line of 514.5 nm as is used in this work. Thus, the peak at 305 cm^{-1} for 5Pb10YSB (Fig. 3.23) seems to indicate that the β -phase is present. There is a slight shoulder on the band below 200 cm^{-1} , most obvious on the spectra measured around $100 - 200^\circ\text{C}$ which could correspond to the low intensity peaks at $\sim 124\text{ cm}^{-1}$. The peak at $\sim 462\text{ cm}^{-1}$ for the β -phase overlaps with the very broad F_{2g} band and could not be resolved here. For 5Pb10YSB spectrum measured at 600°C (inset on Fig. 3.23), the bands reflecting the tetragonal phase had disappeared indicating a conversion to the cubic defect fluorite phase. On cooling back to 25°C (inset on Fig. 3.23), the reappearance of the most prominent peak for the tetragonal β -phase (at 305 cm^{-1})

indicated that the cubic δ -phase was not fully stabilised. This fully confirms the observation from the DTA data. The peaks obtained relate to a phase change rather than oxide ion disordering.

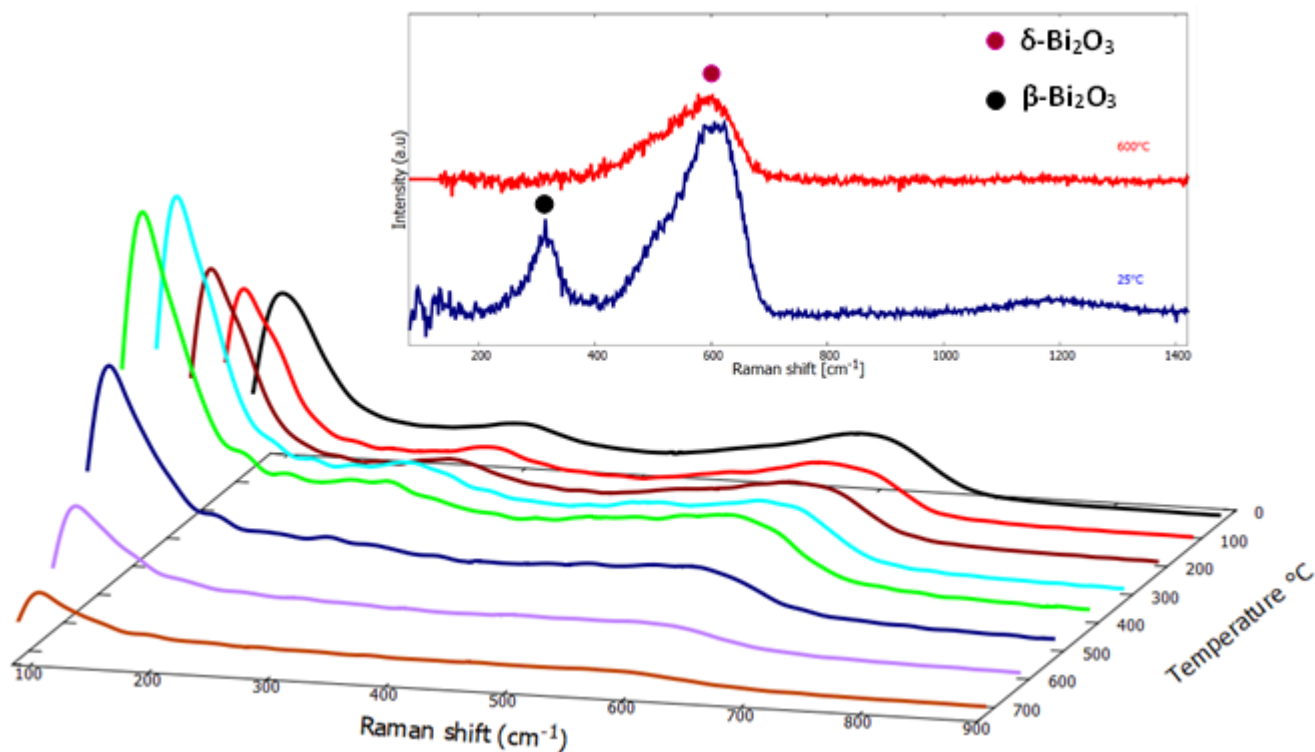


Fig. 3.23 VT-Raman spectra of 5Pb10YSB. The inset (related to cooling back to room temperature) shows an enlarged view depicting how the band at 305 cm⁻¹ disappears at 600°C and reappears at room temperature.

3.5. Analysing PDFs

3.5.1. Peak fitting

The structure of the 1.5Pb25YSB and 5Pb10YSB materials at room temperature was investigated qualitatively by analysing the PDF. A PDF can be thought of as a histogram of all the atoms-atom pair distances in a material. A given atom-atom distance corresponds to the peak positions. Each PDF peak has a Gaussian-like shape due to atomic disorder, which results from a distribution of

atom-atom distances. Basic information can be revealed by fitting the individual PDF peaks.²⁰ A simple cubic bismuth oxide (δ -Bi₂O₃) is used as an example here in order to explain the general understanding of PDFs. The atomic structure of the bismuth oxide is shown in Fig. 3.24a.

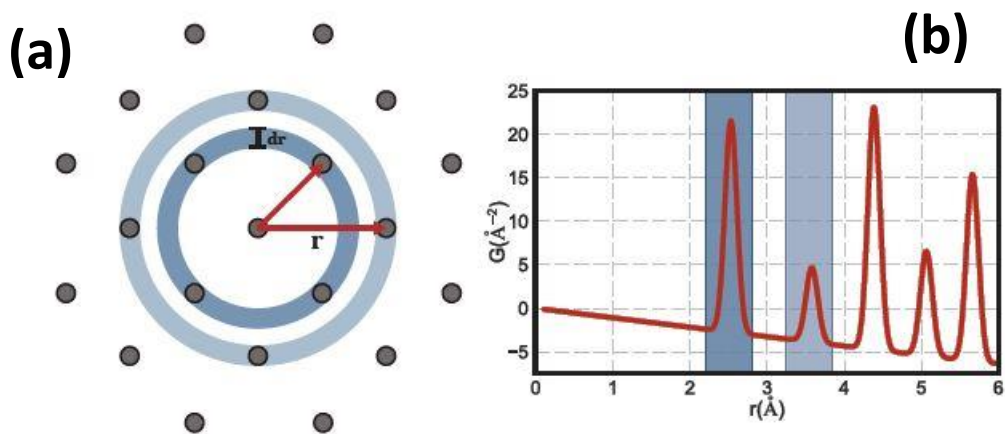


Fig. 3.24 (a) PDF construction of spherical shells of thickness dr at a distance r away from the origin. (b) A face centred cubic (fcc) structure, used in this example, contains 12 nearest neighbours and 6 next-nearest neighbours (not visible due to the viewing angle).²⁰

The low r range in the PDF of bismuth oxide is shown in Fig. 3.24b. δ -Bi₂O₃ has a lattice parameter of about 5.6 \AA . In a PDF plot, the peak positions give the interatomic spacing. The peak at ~ 2.5 \AA , for instance, corresponds to the Bi-Bi pairs, which have an interatomic distance of ~ 2.5 \AA . In the same way, the peaks at ~ 3.5 \AA , 4.4 \AA , 5 \AA and 5.6 \AA refer respectively to the pairs Bi-O, Bi-Bi, Bi-O and Bi-Bi. The height of the peak in Fig. 3.24b, is proportional to the multiplication of the scattering factors for the two elements of the corresponding pair of atoms. Atom-atom pairs produce higher peaks for greater scattering factors than atoms with smaller scattering factors. The area of each peak in Fig. 3.24b is proportional to the coordination number for the corresponding atom-atom pair.²¹ The width of the peak, is correlated with the disorder in the arrangement of atoms. Because of thermal motion at elevated temperatures or because of inherent structural disorder, the peak widths will increase. For atom-atom pairs, wider peaks suggest a broader distribution of interatomic distances.

The raw PDF data for 5Pb10YSB and 1.5Pb25YSB are displayed in Fig. 3.25a and 3.25b, respectively, in the 2.5–9.5 Å selected range. No major differences are observed between the samples in this low r region of the measured PDF curves compared to that for δ -Bi₂O₃ in Fig. 3.24b. The PDF patterns for both 5Pb10YSB and 1.5Pb25YSB were quantitatively studied using the PDFgui software. The main objective of this study was to determine which crystal structure better represents the PDF signal measured.

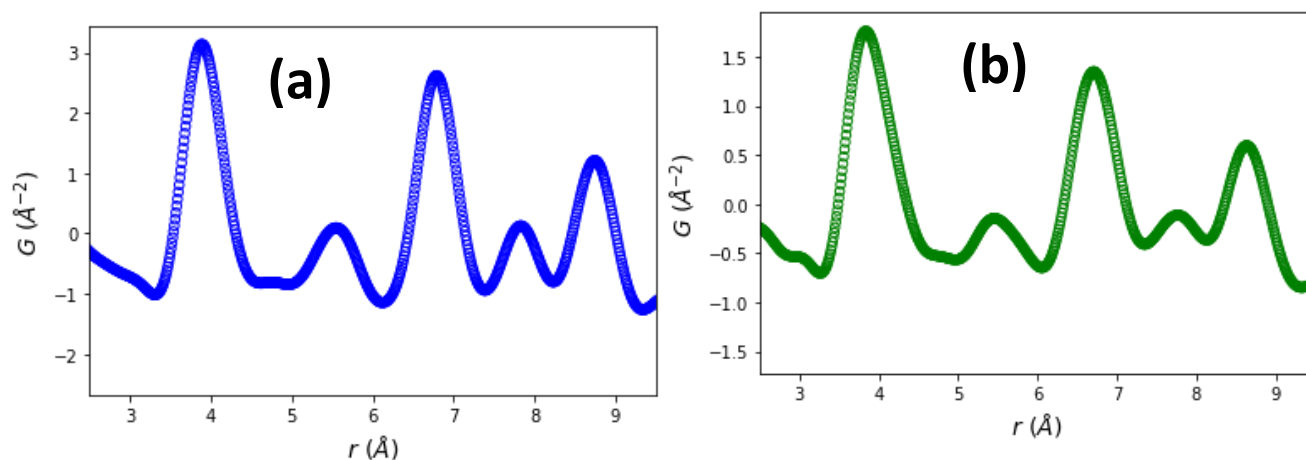


Fig. 3.25 The PDF, $G(r)$ vs r , of 5Pb10YSB (a) and 1.5Pb25YSB (b) data.

3.1.1. PDFgui

There are many methods to obtain structural details once the PDFs have been measured. A "down-hill least squares" refinement is one such methodology, which is applied by the PDFfit program.²² Like the Rietveld method implemented in the GSAS (Generalized Structure Analysis System) software,²² the structural parameters of a proposed model are all modified to achieve the best fit to the experimental data. More recently, a program named PDFfit2 based on the original PDFfit program was developed.²³ The original PDFfit2 engine was rewritten by the developers, and it includes a wide range of enhancements over the original version, such as eliminating bugs and introducing several new features.²³

PDFgui is a graphical user interface based on the PDFfit2 engine, which includes all PDFfit2 features, but simplifies the various user's tasks.²⁴ Using experimental PDF data, it allows users to

customize different parameters. If required, it can also fit PDFs using multiple phases and can easily generate partial PDFs from the models fitted. With the addition of a number of variables, as seen in Fig. 3.26, the Phase Configuration method allows users to input a theoretical structural model. The input into the phase configuration method can be set to certain values or set to be refined by PDFgui as variables. A hypothetical fit to the experimental data will then be produced, generating a R_w value that corresponds to how well the theoretical model matches the data observed. The weighted R-value is calculated as follows:

$$R_w = \sqrt{\frac{\sum_{i=1}^N w(r_i) - [G_{obs}(r_i) - G_{calc}(r_i)]^2}{\sum_{i=1}^N w(r_i) G_{obs}^2(r_i)}} \quad 3.1$$

where N is the number of points, each data point is weighted by $w(r_i)$.

	elem	x	y	z	u11	u22	u33	u12	u13	u23	occ
1	Bi	0.0	0.0	0.0	0.0287738	0.0287738	0.0287738	0.0	0.0	0.0	1.0
2	Pb	0.0	0.0	0.0	0.0287738	0.0287738	0.0287738	0.0	0.0	0.0	1.0
3	Y	0.0	0.0	0.0	0.0287738	0.0287738	0.0287738	0.0	0.0	0.0	1.0
4	O	0.0	0.5	0.5	0.0371703	0.0371703	0.0371703	0.0	0.0	0.0	1.0
5	O	0.5	0.0	0.5	0.0371703	0.0371703	0.0371703	0.0	0.0	0.0	1.0
6	O	0.5	0.5	0.0	0.0371703	0.0371703	0.0371703	0.0	0.0	0.0	1.0

Fig. 3.26 PDFgui phase configuration screen.

A variety of parameters are also included in the software that account for correlated atomic motion. The motion of atoms can be closely correlated at shorter distances, which contributes to sharpening in the experimental PDF at the first few peaks.²⁴ Similarly, the motion of two atoms is uncorrelated at longer distances. Overall, the width of peaks is given by:

$$\sigma_{ij} = \sigma'_{ij} \sqrt{1 - \frac{\delta_1}{r_{ij}} - \frac{\delta_2}{r_{ij}^2}} Q^2_{broad} r^2_{ij} \quad 3.2$$

where σ'_{ij} is the width of a peak without correlated motion, $\frac{\delta_1}{r_{ij}}$ and $\frac{\delta_2}{r_{ij}^2}$ are terms that are appropriate for the correlated motion effect. The expression $\frac{\delta_2}{r_{ij}^2}$ determines the behaviour at low temperatures and $\frac{\delta_1}{r_{ij}}$ describes the behaviour at high temperatures. These terms are strongly correlated, so only one of these terms needs to be refined. The parameters *rcut* and *sratio* (in Fig. 3.26) are used in a refinement as an alternate approach to compensate for the effects of associated motion. Low-to-high-*r* PDF peak ratios are defined by the *sratio* parameter and *rcut* determines to what *r*-range *sratio* is applied (for example, if *rcut* = 3.1, then *sratio* up to 3.1 Å is applied). The user should determine which method should be used for correlated motion correction, and both methods should not be used at the same time.

As a consequence of the *Q*-resolution of the diffractometer, the final part in Eqn. 3.2, $Q^2_{broad} r^2_{ij}$, deals with the effects of peak widening and is only relevant at larger *r*-ranges in the PDF. This *Q* resolution also results in the PDF peaks being exponentially dampened, which is modelled by the *qdamp* parameter in PDFgui. As *Q*-resolution is the same for all data sets gathered at any given time, *qdamp* should not be refined when running refinements. It was obtained in PDFgui by refining a known baseline (LaB₆ was used as the reference in this work). This parameter is one example of instances where, despite giving lower R_w values if refined, it does not make physical sense to refine it for each PDF. Since it is highly correlated with other parameters, such as correlated motion and thermal parameters, refining it does not provide precise refinement results for each model. When refining models at different length scales and in different settings, determining what to refine and what to improve is an important consideration.

The final parameters dealing with peak width in PDFgui are *spdiameter* and *stepcut*. The *spdiameter* parameter refers to the nanoparticle diameter when dealing with nanomaterials, and *stepcut* truncates the PDF to zero at r values above the value set as *stepcut*. Although these various parameters deal with the modelling of peak widths, the relative peak intensities are indicated by the *scalefactor*. It holds the ratio between the peak intensities the same, compared to the overall intensity of the pattern.²⁴

If the parameter flag is set to zero, the refinement does not include it. Parameters may either be fixed to set values or refined by PDFgui as an alternative. If a user has reached the necessary step and variables, the theoretical structure can be refined to the observed data by PDFgui. The values of the refined parameters are provided, and the refined PDF can be plotted on top of the experimental PDF by the software (as seen in Fig 3.27). At the beginning, it was always important to keep refinements simple and then raise the complexity as the model begins to explain the experimental data more accurately. For instance, the scale factor and lattice parameters should only initially be refined over a shorter range than would ultimately be used. This keeps refinements fast and PDFGui may not be able to handle refining all the parameters at once initially. It is also important to take care to verify the effects of refinements beyond the R_w values alone and the difference plots are extremely useful in this respect. Additionally, PDFGui may produce a very good fit for experimental data ($R_w < 10\%$), but it has accomplished this by altering one parameter beyond anything that is physically rational.

The same starting model used during Rietveld refinement was used to refine the PDF data. The model (from inorganic crystal structure database) was based on the space group *Fm-3m* derived for pure δ -Bi₂O₃, as it is difficult to get an accurate refinement when the sample has one phase (β -phase) a lot lower than the other (δ -phase) with the two phases overlapping. Parameters (as shown in Fig. 3.27) such as scale factor, lattice parameters, delta1(or delta2), atomic displacement parameters, Qdamp (or Qbroad) were refined until a good agreement between the refined and measured PDF data were obtained for both 5Pb10YSB and 1.5Pb25YSB samples. Ultimately, a lot of time was spent on designing appropriate approaches to the calculated PDFs

for refinement. Model agreements score R_w , for 1.5Pb25YSB was 14.7% while for 5Pb10YSB was 11.2%. Both of which results with better fit.

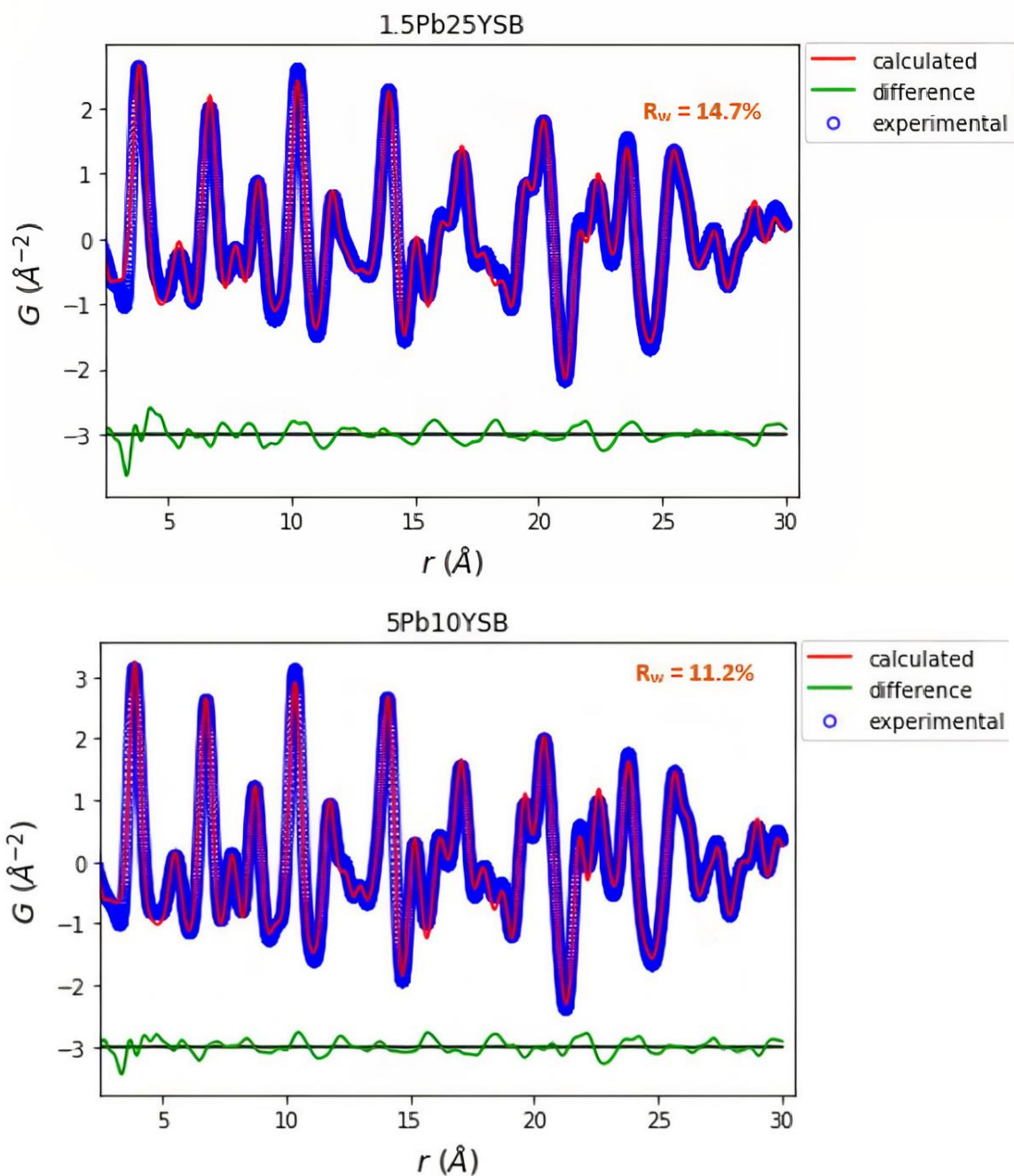


Fig. 3. 27 A calculated fit for the experimental PDFs at room temperature of 5Pb10YSB (a) and 1.5Pb25YSB (b) using PDFgui. The red line represents the theoretical PDF, the experimental data is represented by the blue circles, and the green line at the bottom of the plot represents the difference between the two.

3.2. References

1. Omari, M., Drache, M., Conflant, P. and Boivin, J.C., 1990. Anionic conduction properties of the fluorite-type phase in the $\text{Bi}_2\text{O}_3\text{-Y}_2\text{O}_3\text{-PbO}$ system. *Solid State Ionics*, 40, pp.929-933.
2. Jung, D.W., Duncan, K.L. and Wachsman, E.D., 2010. Effect of total dopant concentration and dopant ratio on conductivity of $(\text{DyO}_{1.5})_x\text{-(WO}_3)_y\text{-(BiO}_{1.5})_{1-x-y}$. *Acta Materialia*, 58(2), pp.355-363.
3. Jung, D.W., Nino, J.C., Duncan, K.L., Bishop, S.R. and Wachsman, E.D., 2010. Enhanced long-term stability of bismuth oxide-based electrolytes for operation at 500 C. *Ionics*, 16(2), pp.97-103.
4. Jung, D.W., Duncan, K.L., Camaratta, M.A., Lee, K.T., Nino, J.C. and Wachsman, E.D., 2010. Effect of Annealing Temperature and Dopant Concentration on the Conductivity Behavior in $(\text{DyO}_{1.5})_x\text{-(WO}_3)_y\text{-(BiO}_{1.5})_{1-x-y}$. *Journal of the American Ceramic Society*, 93(5), pp.1384-1391.
5. Jung, D.W., Lee, K.T. and Wachsman, E.D., 2016. Dysprosium and gadolinium double doped bismuth oxide electrolytes for low temperature solid oxide fuel cells. *Journal of The Electrochemical Society*, 163(5), pp.F411.
6. Durmuş, S., Çorumlu, V., Çifci, T., Ermis, I. and Arı, M., 2013. Electrical, structural and thermal properties of nanoceramic $(\text{Bi}_2\text{O}_3)_{1-x-y}(\text{Ho}_2\text{O}_3)_x(\text{Tm}_2\text{O}_3)_y$ ternary system. *Ceramics International*, 39(5), pp.5241-5246.
7. Battle, P.D., Catlow, C.R.A., Drennan, J. and Murray, A.D., 1983. The structural properties of the oxygen conducting δ phase of Bi_2O_3 . *Journal of Physics C: Solid State Physics*, 16(17), p.L561.
8. Bandyopadhyay, S. and Dutta, A., 2018. A structural insight into the electrical properties of Dy-Ho co-doped phase stabilized Bismuth Oxide based electrolytes. *Journal of Electroanalytical Chemistry*, 817, pp.55-64.
9. Yashima, M., Ishimura, D. and Ohoyama, K., 2005. Temperature Dependence of Lattice Parameters and Anisotropic Thermal Expansion of Bismuth Oxide. *Journal of the American Ceramic Society*, 88(8), pp.2332-2335.
10. Shannon, R., 1976. Revised effective ionic radii and systematic studies of interatomic distances in halides and chalcogenides. *Acta Crystallographica Section A*, 32(5), pp.751-767.
11. Jiang, N., 2002. A higher conductivity Bi_2O_3 -based electrolyte. *Solid State Ionics*, 150(3-4), pp.347-353.
12. Jung, D., Lee, K. and Wachsman, E., 2016. Dysprosium and Gadolinium Double Doped Bismuth Oxide Electrolytes for Low Temperature Solid Oxide Fuel Cells. *Journal of The Electrochemical Society*, 163(5), pp.F411-F415.
13. Verkerk, M.J., Keizer, K. and Burggraaf, A.J., 1980. High oxygen ion conduction in sintered oxides of the $\text{Bi}_2\text{O}_3\text{-Er}_2\text{O}_3$ system. *Journal of Applied Electrochemistry*, 10(1), pp.81-90.
14. Jiang, N., Buchanan, R.M., Stevenson, D.A., Nix, W.D., Li, J.Z. and Yang, J.L., 1995. Anion ordering in aged stabilized bismuth oxide. *Materials Letters*, 22(5-6), pp.215-219.
15. Kruidhof, H., De Vries, K.J. and Burggraaf, A.J., 1990. Thermochemical stability and nonstoichiometry of yttria-stabilized bismuth oxide solid solutions. *Solid State Ionics*, 37(2-3), pp.213-215.
16. Watanabe, A., 1989. Phase relations of hexagonal and cubic phases in holmia-doped bismuth sesquioxide, $\text{Bi}_{2-2x}\text{Ho}_{2x}\text{O}_3$ ($x=0.205\text{-}0.245$). *Solid State Ionics*, 34(1-2), pp.35-39.
17. Yashima, M. and Ishimura, D., 2003. Crystal structure and disorder of the fast oxide-ion conductor cubic Bi_2O_3 . *Chemical Physics Letters*, 378(3-4), pp.395-399.
18. Lee, S.Y., Zhang, D., McCamant, D.W., Kukura, P. and Mathies, R.A., 2004. Theory of femtosecond stimulated Raman spectroscopy. *The Journal of Chemical Physics*, 121(8), pp.3632-3642.
19. Hardcastle, F.D. and Wachs, I.E., 1991. Molecular structure of molybdenum oxide in bismuth molybdates by Raman spectroscopy. *The Journal of Physical Chemistry*, 95(26), pp.10763-10772.

20. Hou, D., Zhao, C., Paterson, A.R., Li, S. and Jones, J.L., 2018. Local structures of perovskite dielectrics and ferroelectrics via pair distribution function analyses. *Journal of the European Ceramic Society*, 38(4), pp.971-987.
21. Proffen, T. and Billinge, S.J.L., 1999. PDFFIT, a program for full profile structural refinement of the atomic pair distribution function. *Journal of Applied Crystallography*, 32(3), pp.572-575.
22. Farrow, C.L., Juhas, P., Liu, J.W., Bryndin, D., Božin, E.S., Bloch, J., Proffen, T. and Billinge, S.J.L., 2007. PDFfit2 and PDFgui: computer programs for studying nanostructure in crystals. *Journal of Physics: Condensed Matter*, 19(33), pp.335219.
23. Jeong, I.K., Proffen, T., Mohiuddin-Jacobs, F. and Billinge, S.J., 1999. Measuring correlated atomic motion using X-ray diffraction. *The Journal of Physical Chemistry A*, 103(7), pp.921-924.
24. Olaj, O., 1976. Pair distribution function and pair potential of lattice model chains under theta conditions, 2. Theoretical approach. *Die Makromolekulare Chemie*, 177(11), pp.3427-3435.

4.1. Variable Temperature EIS

Using impedance spectroscopy, the ionic transport properties of the samples were studied. The complex impedance (Z^*), a frequency dependent electrical property of the materials, can be expressed as:¹

$$Z^*(\omega) = Z'(\omega) - jZ''(\omega) \quad 4.1$$

where, Z' and Z'' are the real and imaginary parts of impedance, respectively. In order to investigate the influence of Pb:Y content on electrical properties of the $\text{Bi}_2\text{O}_3\text{-PbO-Y}_2\text{O}_3$ composite electrolytes, samples containing both high concentrations (3.75Pb25YSB and 6Pb25YSB sample) and low concentrations (5Pb10YSB sample) were studied to determine whether the δ -phase obtained from XRD patterns is stable from room temperature to higher temperature.

Electrical impedance spectroscopy (EIS) was carried out, at open circuit voltage, in the temperature range of 300–750 °C in air atmosphere. The impedance spectra recorded changed as the temperature is increased and required different analysis strategies for different temperature regions and these will be discussed in turn.

4.2. Analysis of impedance spectra measured in low temperature range

The complex impedance spectra measured at 300 °C consist of two semicircular arcs and a small ray arc as shown in the schematic representation in Fig. 4.1(a) and 4.1(b). An example showing the experimental data with the fitted curve is shown in Fig. 4.2(a). To be brief, only one set of fitting results are shown here, but all the other fittings were to the same level of precision. The equivalent circuit needed to describe the various charge migrations and polarization phenomena occurring in different frequency ranges in the sample is depicted in Fig. 4.2 (b) as a visual

representation. This circuit consists of $R1/Q1+(R2+W2)/Q2$, where “/” represents circuit elements in parallel and “+” represents elements in series. The $R1/Q1$ portion models processes occurring in the bulk of the grains, and $R2/Q2$ represents the conduction through the grain boundaries or the electrode/electrolyte interfacial polarization resistance (R_{el}).

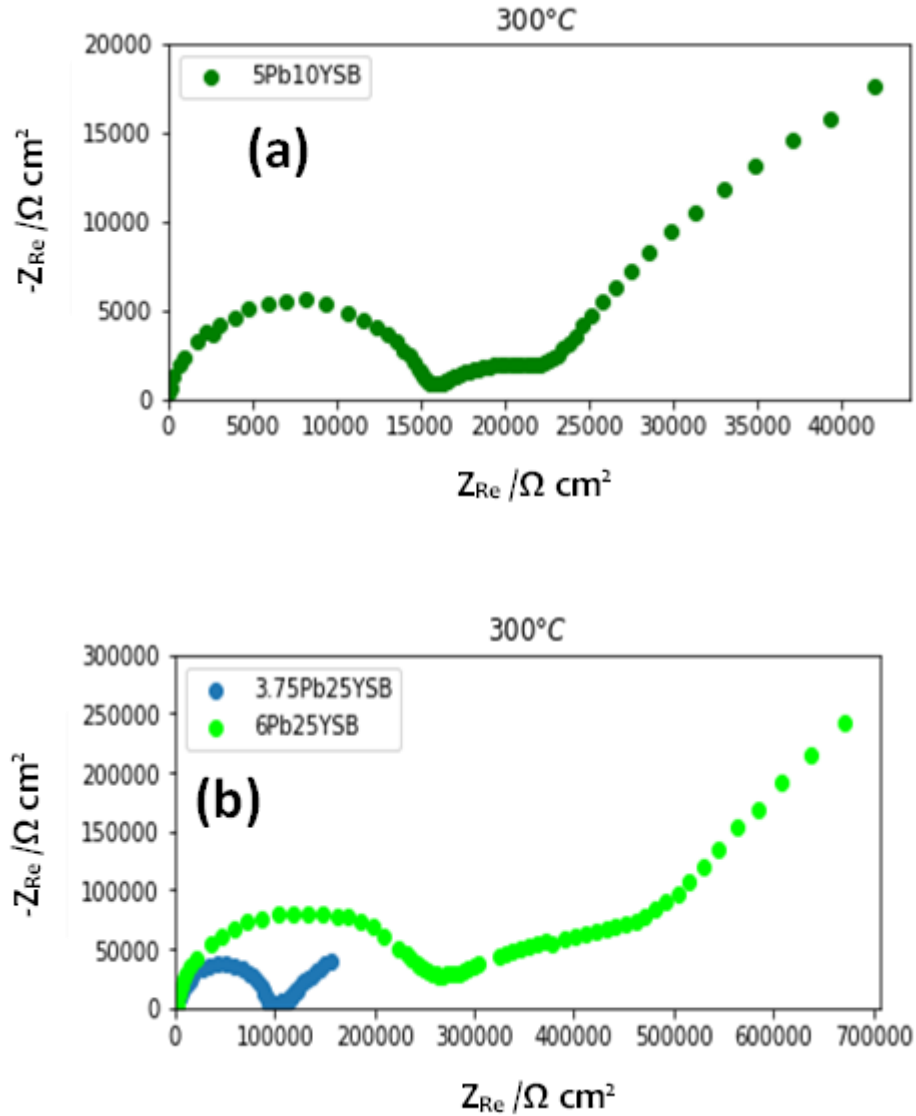


Fig. 4.1 Typical impedance spectra of 5Pb10YSB (a), (b) 3.75Pb25YSB and 6Pb25YSB compositions in air at 300 °C.

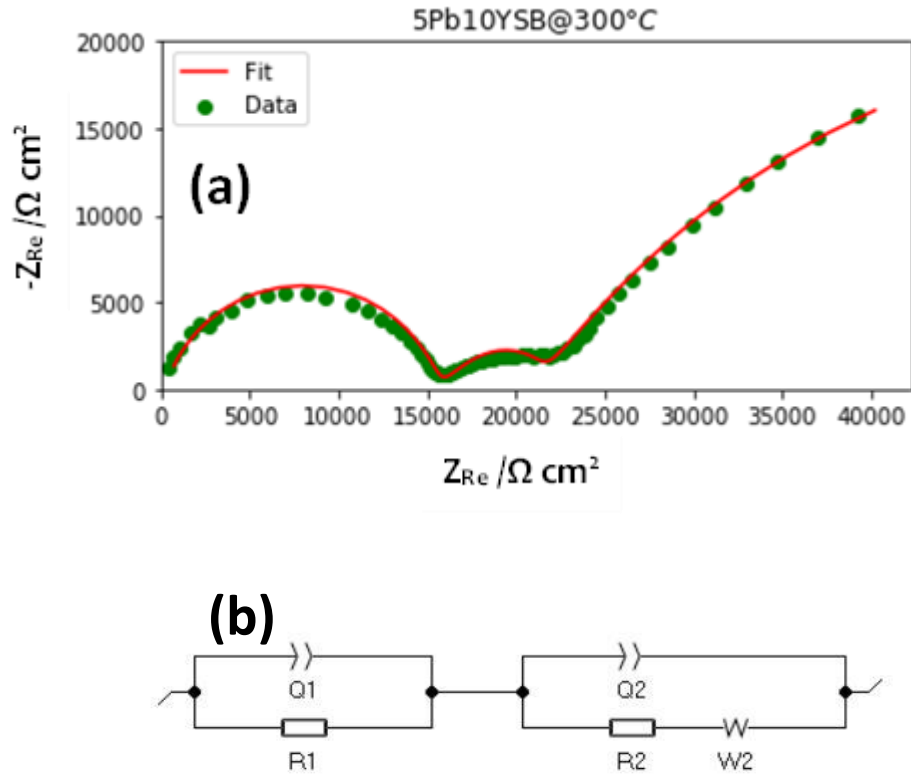


Fig. 4.2 EIS analysis of 5Pb10YSB measured at 300 °C with (a) Nyquist plots of experimental (symbols) and fitted results (lines) and (b) the equivalent circuit model used.

The lower frequency intercept of the semicircle representing the grain (R_1/Q_1) with the real axis (Z') gives the grain's bulk resistance (R_b) while the interception of lower frequency semicircle (R_2/Q_2) provides an indicating of the grain boundaries resistance (R_{gb}) or the electrolyte/electrode interfacial polarization resistance (R_{el}). The disparity in the intercepts of the second semicircle on the real axis (i.e. in the high and low frequency range) corresponds to the grain boundary resistance or electrode/electrolyte interfacial polarization resistance (R_{gb} or R_{el}), so the total resistance, $R_t = R_b + R_{gb}$ (or R_{el}). Both R_{gb} (or R_{el}) and R_b values decrease as temperature increases, indicating a negative temperature coefficient of resistance. This can be explained by an increase in charge carrier mobility and/or a decrease in the average potential barrier energies observed by charge carriers.¹

In the low-frequency region, the sloping line refers to oxide diffusion in the electrolyte and depends on the frequency of the perturbation. This is represented by the Warburg element because diffusion occurs from the bulk of the electrolyte to the electrode interface.^{2,3} The Warburg element (W) is used to fit semi-infinite diffusion of species through the diffusion layer. The diffusion is semi-infinite when at the lowest frequency there is not enough time at each perturbation for the charge carrier to cross the entire diffusion layer. The Warburg impedance is small at high frequencies as diffusing reactants do not have time to travel very far. The ions diffuse further at low frequencies, thereby increasing the Warburg impedance.

The Nyquist diagram plot depicts a semi-circle with its center below the real axis. This characteristic occurs due to the polycrystalline nature of the electrolyte sample.² An R/Q circuit, rather than an R/C circuit, can be used to simulate this "depressed" semicircle where the latter is more applicable to a perfect semicircle, and Q represents a constant phase element (CPE). When using a Q element instead of a C element, it is useful to calculate an equivalent capacitance known as a pseudo capacitance. This calculation is only applicable for a (R/Q) circuit and not applicable to (R+W)/Q circuits. It refers to finding a capacitance value C at an angular frequency ($\omega_c = 2\pi f_c$) that corresponds to the maximum imaginary component on the Nyquist plot obtained by fitting the circuit (R/Q). The following equation then applies:⁴

$$\frac{1}{2\pi(RQ)^{1/a}} = \frac{1}{2\pi RC} \Rightarrow C = Q^{1/a} R^{(1/a)-1} \quad 4.2$$

with a being a value between 0 and 1. Eqn 4.2 only applies if a is not too small (typically $a > 0.7$). The values Q, a and bulk grain resistance (R_b) as determined by fitting the high frequency semi-circle for spectra measured at several temperatures, are summarised in Table 4.1, with the standard deviations of fitting for R_b given as it was used in further calculations.

Table 4.1 Values of the resistance (R_b), frequency exponent (a), constant phase element (Q_b) and pseudo capacitance (C_b) for the bulk contribution of all the samples at different temperatures.

	T/°C	R_g / Ω	a	$Q_b / F.s^{(a-1)}$	C_b / nF
5Pb10YSB	300	$15\,617 \pm 2$	0.814	0.306×10^{-9}	18.6
	350	$2\,128 \pm 1$	0.859	0.290×10^{-9}	27.7
	400	325 ± 4	0.908	0.170×10^{-9}	31.6
	450	33 ± 7	0.766	2.82×10^{-6}	66.3
3.75Pb25YSB	300	$91\,880 \pm 1$	0.911	41.5×10^{-12}	12.2
	350	$13\,047 \pm 3$	0.913	59.8×10^{-12}	15.5
	400	$2\,355 \pm 1$	0.980	36.5×10^{-12}	26.3
	450	530 ± 1	0.939	0.117×10^{-9}	39.6
6Pb25YSB	300	$243\,755 \pm 3$	0.802	0.142×10^{-9}	11.3
	350	$39\,535 \pm 3$	0.780	0.315×10^{-9}	13.0
	400	$5\,486 \pm 1$	0.952	42.3×10^{-12}	19.4
	450	$1\,062 \pm 1$	0.733	3.51×10^{-9}	36.5

4.3. Analysis of impedance spectra measured in IT- and HT- range

The data measured at 500°C (see Fig. 4.3) results with the disappearance of the high frequency semi-circle as it is not measured to high enough frequency to obtain information on bulk, but the bulk resistance can still be established. The shape of the impedance plots changed essentially to one small ray arc with a long tail, where the intersection with the real axis represents the bulk resistance (R_t). The EIS response seems to consist of an intermediate frequency (R/Q) arc followed by the diffusion impedance response which overlap in the complex impedance plane due to their relaxation frequencies being similar.

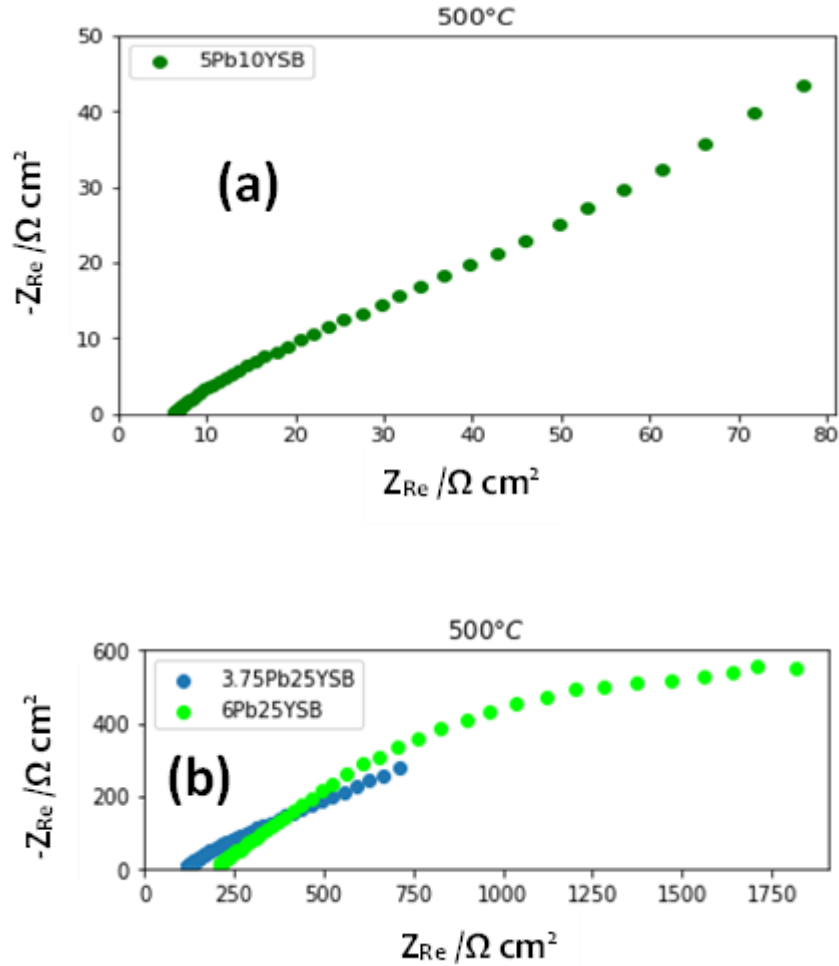


Fig. 4.3 Typical impedance spectra of (a) 5Pb10YSB, (b) 3.75Pb25YSB and 6Pb25YSB compositions in air at 500 °C.

Mobile charge diffusion in the electrolyte is often represented using the equivalent circuit as shown in Fig. 4.4(b). This circuit is a modification to the Randles circuit where the charge transfer resistance involves a Warburg diffusion (W) in series with resistance. W2 is the Warburg impedance associated with the mass transport (by diffusion) of the oxide species; R2 and Q2 represent the grain boundaries or the electrolyte/electrode interfacial polarization resistance and depressed capacitance, respectively; R1 is the electrolyte resistance.

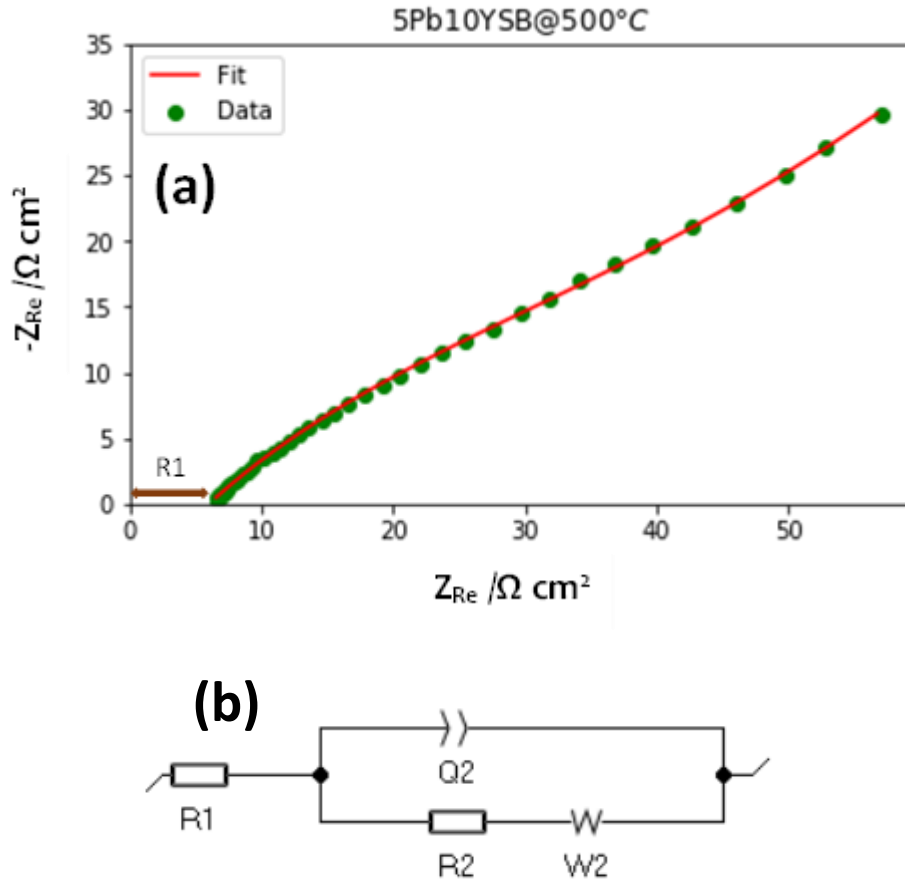


Fig. 4.4 EIS analysis of 5Pb10YSB measured at 500 °C with (a) Nyquist plots of experimental (symbols) and fitted results (lines) and (b) the equivalent circuit model used.

At high temperatures the oxide ions are far more mobile, and it is possible that at low frequencies the charge carriers have sufficient time to move across the entire sample thus reaching the end of the diffusion path before the alternating signal is switched to the other direction (in the typical sine wave fashion).³ As a result, the Warburg semi-infinite diffusion model, and the representative Warburg circuit element (W), are no longer applicable. Now the Warburg diffusion element of finite-length type (W_δ) is used instead. This is the case for the impedance data measured at 700°C (Fig. 4.5). This form of the Warburg impedance is only valid if the diffusion layer has an infinite thickness. Quite often this is not true. If the diffusion layer is bounded, the

impedance at lower frequencies no longer obeys Eqn. 2.13.⁴ Instead, it obeys Eqn.2.14. This more general equation is called the porous bounded Warburg.⁴

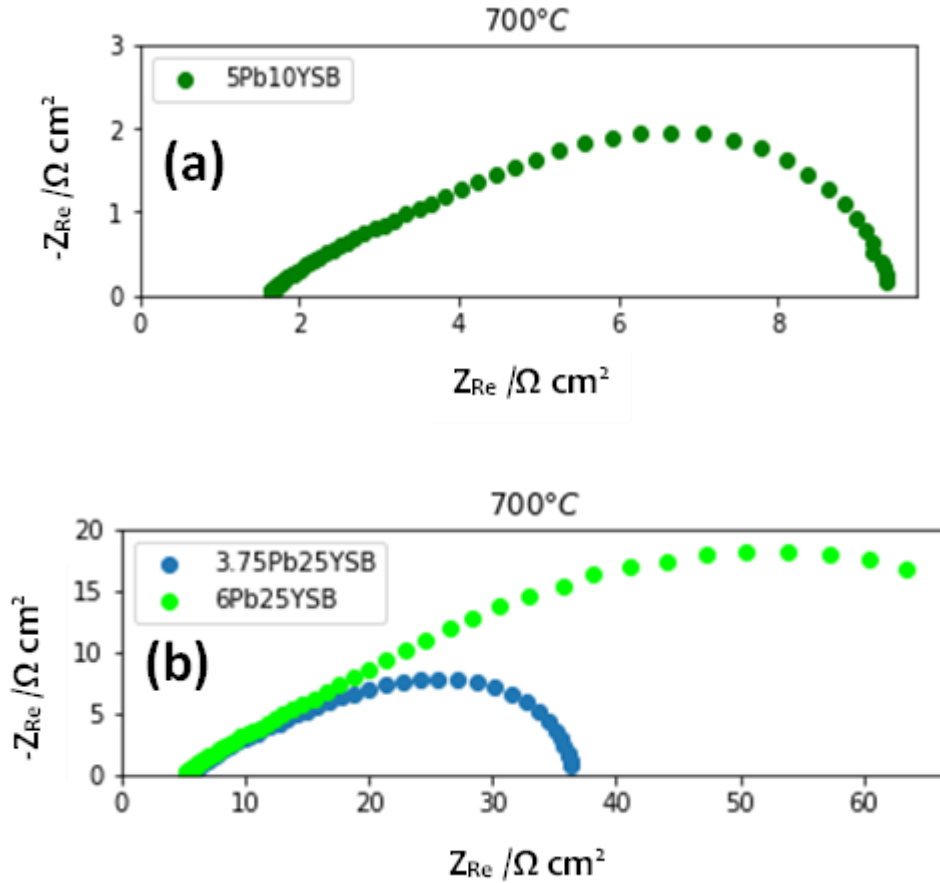


Fig. 4.5 Impedance spectra for (a) 5Pb10YSB, (b) 3.75Pb25YSB and 6Pb25YSB compositions in air at 700 °C.

To fit the impedance data shown in Fig. 4.5, the Randles circuit was used but with a finite length Warburg (FLW) element due to a bounded diffusion layer. The expression (Eqn. 2.14) of the impedance of the W_δ is based on the Nernst model approximation: the concentration variations of the species due to the electrochemical reaction only occurs within the diffusion layer. Outside of the diffusion layer (i.e. in the bulk), the concentration is constant.⁵ The corresponding Randles circuit is shown in Fig. 4.6(b). Common examples of a Porous Bounded Warburg are diffusion to

a rotated disk electrode or the diffusion of oxygen through a thin coating. The FLW element can also be used where mass transport mechanism involve both diffusion and convection.

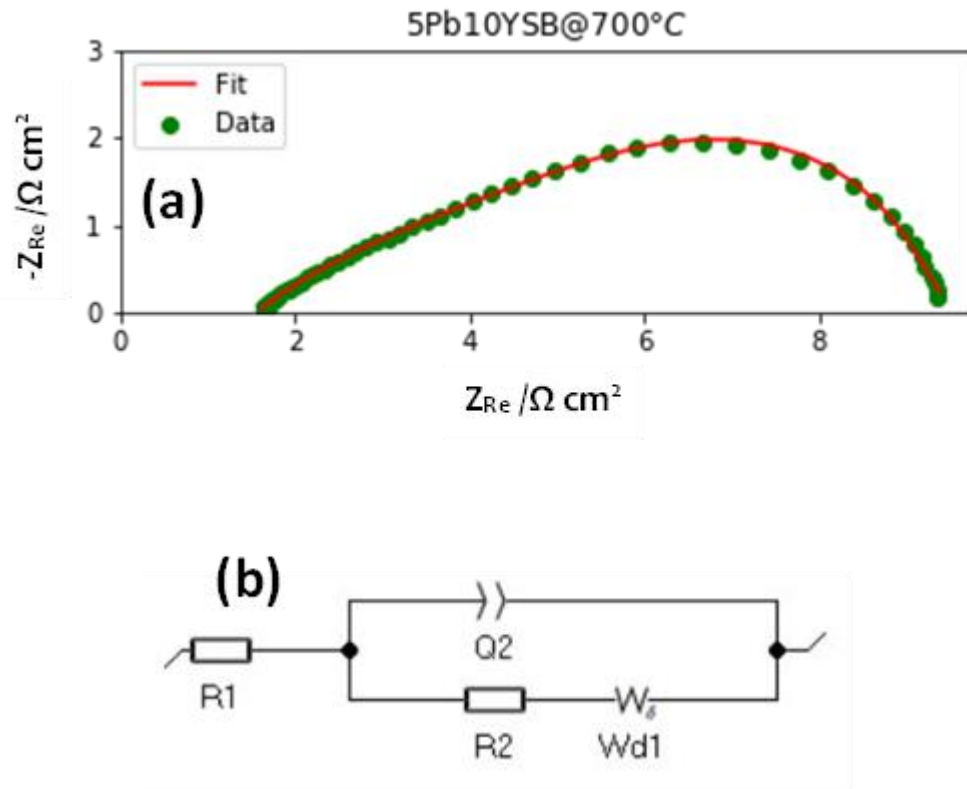


Fig. 4.6 Impedance spectrum of 5Pb10YSB measured at 700 °C with a) Nyquist plots of experimental (symbols) and fitted results (lines) and (b) the equivalent circuit model used.

The typical system where both diffusion and convection play a role and where this W_{δ} element is often used is for a rotating disc electrode (RDE).⁵ When rotated the solution flows to the surface of the electrode in a direction perpendicular to the surface and then across the surface of the electrode. This results in the diffusion layer being significantly smaller than if no rotation were being performed. This is generally true for more ordered convection. Since we are dealing with a solid sample where no convection can take place, the pellets that are being analysed are fairly thin (an average 1 mm thick). At low temperatures the O^{2-} ions can only diffuse slowly through the lattice. As the temperature increases, mobility increases and the O^{2-} ions diffuse more rapidly

through the lattice. At high temperatures the mobility is significantly faster and the O^{2-} ions can traverse the entire thickness of the pellet for the low frequency measurements. This is analogous to having a thinner diffusion layer for RDE's thus at high temperature the diffusion is bounded by the O^{2-} ions traversing the thickness of the pellet and reaching the electrode boundary where diffusion can no longer proceed.

ZFit, the software by BioLogic used to analyze the impedance plots, exploits a nonlinear least squares regression to fit the data with the function from the equivalent circuit, using the Levenberg–Marquardt algorithm. The fitting procedure will change the values of the parameters until the mathematical function matches the experimental data within a certain error margin. The goodness of the fit is represented by the χ^2 (chi-squared) value. The better the fit, the closer to 0 will be the χ^2 value. The formula is the following:

$$\chi^2 = \sum_{i=1}^N \left| \frac{Z_i(f_i) - Z(f_i)}{E} \right|^2 \quad (4.3)$$

with $Z_i(f_i)$ denoting the measured impedance and $Z(f_i)$ denoting the calculated impedance at f_i for a given set of parameter values, and N denoting the number of points. The values of χ^2 for the data fitted with different elements are shown in Table 4.2. The χ^2 values seem to be high for measurements taken at low temperature due to a poor fit obtained between the real data and the simulated data. This is mainly due to the poorer fit around the second semicircle represented by R_2/Q_2 as well as the much higher overall impedance values. At high temperature, better fits were obtained resulting with low χ^2 values. χ^2/\sqrt{N} is a normalized expression of χ^2 whose value is independent of the number of points (N).

Table 4.2 Chi-square values obtained while fitting real data and the simulated data at several temperatures.

Temperature (°C)	5Pb10YSB		3.75Pb25YSB		6Pb25YSB	
	χ^2	χ^2/\sqrt{N}	χ^2	χ^2/\sqrt{N}	χ^2	χ^2/\sqrt{N}
300	16.5×10^6	467.1	0.805×10^9	3343	4.31×10^9	7960
350	1.36×10^6	135.5	76.3×10^6	1002	0.590×10^9	2843
400	7.93×10^3	10.21	3.16×10^6	203.7	37.4×10^6	688.3
450	109	1.197	62.3×10^3	28.26	9.30×10^5	108.5
500	14.1	0.4425	688	3.157	14.3×10^3	13.47
550	36.9	0.7424	77.5	1.101	1.93×10^3	4.969
600	4.41	0.2584	270	1.936	215	1.672
650	3.19	0.2216	85.6	1.090	74.2	1.008
700	0.621	0.09629	17.6	0.4941	2.67	0.1982
750	4.16	0.2549	1.69	0.1691	1.900	0.1658

4.4. Ionic conductivities and activation energies

To calculate the activation energy (in terms of eV) of the conduction process, the bulk electrical conductivity (σ_b) is first calculated using the equation:⁶

$$\sigma_b = \frac{4e}{\pi d^2 R_b} \quad (4.4)$$

where e is the sample thickness, $\pi d^2/4$ is the section area of the sample (as the pellet is round disk) with d being sample diameter and R_b is the bulk resistance of the sample. The conductivity values of the bulk (σ_b) are summarized in Table 4.3, determined at several temperatures. When the temperature increases, measuring to a maximum frequency of 1 MHz did not give data for the bulk impedance as a semi-circle. The values of bulk resistance were then taken from intercept at high frequency and determined from the equivalent circuit modelling (ECM) as the series R1 value (Fig. 4.5 and 4.6). The conductivity of the electrolyte of each composition was obtained from measured bulk resistance and sample dimensions.

Table 4.3 Bulk conductivity and resistance values obtained using different equivalent circuits at different temperatures, 300-450°C values were obtained using Fig. 4.2b, Fig. 4.4b for 500-600°C and Fig. 4.6b for 650-750°C.

T/°C	5Pb10YSB		3.75Pb25YSB		6Pb25YSB	
	R _b / Ω	σ _b / Ω ⁻¹ cm ⁻¹	R _b / Ω	σ _b / Ω ⁻¹ cm ⁻¹	R _b / Ω	σ _b / Ω ⁻¹ cm ⁻¹
300	15 617 ± 2	2.77 × 10 ⁻⁵	91 880 ± 1	0.5626 × 10 ⁻⁵	243 755 ± 3	1.764 × 10 ⁻⁶
350	2 128 ± 1	2.04 × 10 ⁻⁴	13 047 ± 3	3.962 × 10 ⁻⁴	39 535 ± 3	1.088 × 10 ⁻⁶
400	325 ± 4	1.34 × 10 ⁻³	2 355 ± 1	2.195 × 10 ⁻⁴	5 486 ± 1	7.838 × 10 ⁻⁵
450	33 ± 7	1.3 × 10 ⁻²	530.0 ± 0.4	9.753 × 10 ⁻⁴	1 062 ± 0.4	4.049 × 10 ⁻⁵
500	6.1 ± 0.4	0.12	114.8 ± 0.3	5.227 × 10 ⁻³	199.3 ± 0.6	2.882 × 10 ⁻³
550	3.2 ± 0.3	0.23	34 ± 2	0.017	51 ± 4	0.011
600	2.2 ± 0.2	0.33	15 ± 1	0.040	18 ± 0.2	0.031
650	1.6 ± 0.3	0.45	8.1 ± 0.3	0.074	7.5 ± 1.0	0.074
700	1.3 ± 0.3	0.55	4.8 ± 0.3	0.12	4.8 ± 0.3	0.12
750	1.2 ± 0.3	0.65	3.2 ± 0.4	0.19	3.2 ± 0.3	0.18

The Arrhenius equation given by,⁷

$$\sigma = \sigma_0 \exp\left(-\frac{E_a}{K_b T}\right) \quad (4.5)$$

where σ is the conductivity, σ_0 is the pre-exponential factor, E_a is the activation energy for electrical conduction, K_b is the Boltzmann's constant and T is the absolute temperature. This equation can be used to determine the activation energy (E_a) through the slope obtained from a plot of $\ln \sigma$ (where σ refers to the values of σ_b) versus $(1/T)$.

The Arrhenius plots of the bulk conductivity of three PbYSB electrolytes (5Pb10YSB, 3.75Pb25YSB, and 6Pb25YSB) are shown in Fig. 4.7(a). As is expected from a thermally activated conductivity mechanism that is inherent to ionic conducting ceramics,⁷ the conductivities were found to increase on heating and conversely, decrease on cooling. It was noted that particularly for the low dopant samples (5Pb10YSB in Fig. 4.7(a)), there is a 'step function' type behavior on both the heating and cooling cycles, within the temperature range of 450–550 °C. This step is largely attributed to the conversion of the initial phase mixture into a pure cubic phase and the temperature range in which this happens corresponds to the *in-situ* phase transitions observed in both Raman spectroscopy and high resolution PXRD.

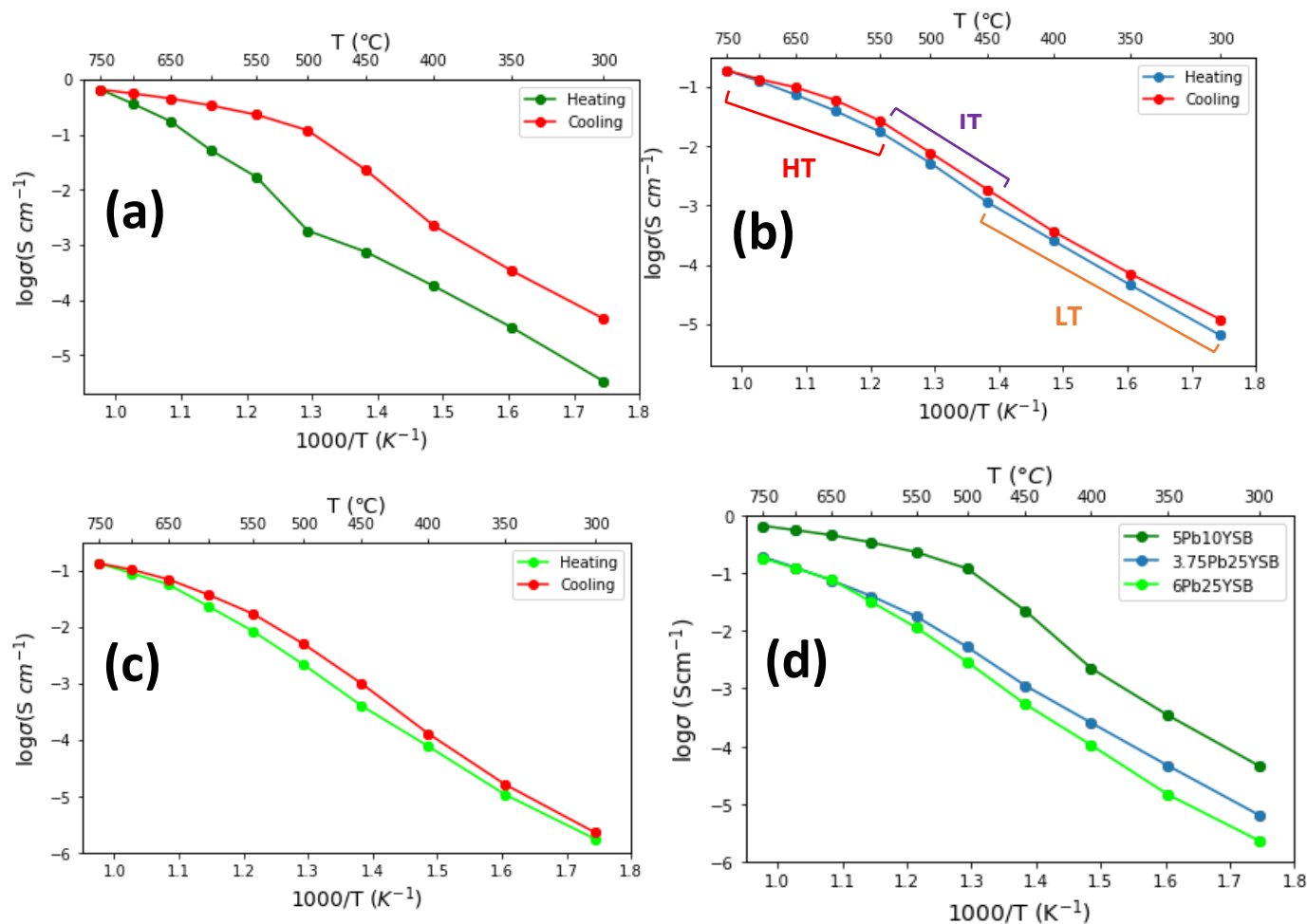


Fig. 4.7 Arrhenius plots of the bulk conductivity for 5Pb10YSB (a), 3.75Pb25YSB (b) and 6Pb25YSB (c) showing results from both the heating (blue/green lines) and the cooling cycles (red lines). Data for the first cycle is plotted in (a) and the second cycle in (b) and (c). A comparison of the cooling cycles of the three results is shown in (d).

For the purer samples with higher total dopant content (3.75Pb25YSB and 6Pb25YSB in Fig. 4.7(b) and 4.7(c), respectively), this feature is essentially absent. The “knee” or bend in the curve at around 550-600°C for 5Pb10YSB sample is attributed to the order-disorder transition as will be discussed in detail shortly.

It should be noted that in this work no electrodes were coated directly onto the pellet for the conductivity measurements. The pellet was simply placed between two solid platinum disc electrodes (with similar diameter to the pellet) on the cell holder which was spring-loaded to apply some pressure. This appears to provide less intimate contact especially on the first heating cycle. Better contact is established once the samples have been heated and this resulted in a significant difference (in terms of conductivity) between heating and cooling on the first cycle, Fig 4.7(a). On the second cycle, performed directly after the first, better contact has already been made and the difference is minimal between heating and cooling as shown in Fig 4.7(b) and 4.7(c). So, the best way to deal with data where the second cycle was not measured (Fig 4.7(a)) is to use the cooling cycle for actual conductivities.

Of these compositions, 5Pb10YSB exhibited the highest conductivity throughout the temperature range. The conductivity of 5Pb10YSB at 300, 500 and 700 °C, was 2.0×10^{-5} , 0.071, 0.33 S/cm. Linear regions are seen below 450°C for both 3.75Pb25YSB and 6Pb25YSB, above 550 °C for 3.75Pb25YSB and 650 °C for 6Pb25YSB. In general, a lower total dopant concentration results in higher conductivity as expected and is clearly shown in the Arrhenius plot of conductivity, Fig. 4.7(d).

The Arrhenius plots reveal that the compositions 3.75Pb25YSB and 6Pb25YSB show relatively good conductivity at about 500°C (~0.002 S/cm), but this is lower than for the 25YSB parent composition reported as 0.013 S/cm at 500 °C by Takahashi et al.⁹ The variations in the electrical conductivity of the studied PbYSB materials can be considered in three temperature regions as indicated in Fig. 4.7b. The plots for all samples below ~450°C are essentially linear and above ~550-600°C another fairly linear region exists. The transition between the two regions can also be considered as linear and therefore the system exhibit three linear regions (HT: high temperature, IT: intermediate temperature and LT: low temperature) each with a different slope. Clearly the increase in the conductivities with an increase in temperature is due to an increase in mobility of the interstitial O²⁻ ions with the increased temperature. At higher temperatures, the

thermal vibration energy of the ions increases, resulting in increased oxygen ionic mobility. Furthermore, the theoretical concept of oxide anionic conductivity is as follows:¹⁰⁻¹⁴

$$\sigma_b = 2ne\mu \quad (4.6)$$

where n , μ and e are the carrier density, oxide ion mobility and elementary electric charge, respectively. The mobility and the number of charge carriers result in an improvement for the bulk conduction. At low temperatures (such as room temperature), the thermal energy of the O^{2-} anions is insufficient to hop to the nearest neighbouring tetrahedral vacancy point, despite the presence of interstitial O^{2-} vacancies in the crystal structure. The fcc-type materials, therefore, display only very poor ionic conductivity dominantly at low temperatures. Additionally, the ordered structure of the O^{2-} vacancy sublattice tends to be dominant at low temperatures, and there is little total random distribution of vacancies.¹³

The transformation from the ordered arrangements of O^{2-} ions to the disordered positions of O^{2-} ions at the tetrahedral lattice points (i.e. the O^{2-} sublattice) is expected to cause a variation in the conduction. This transformation can be represented as $\delta\text{-Bi}_2\text{O}_3(\text{ordered}) \rightarrow \delta\text{-Bi}_2\text{O}_3(\text{disordered})$. This ordered structure has lower O^{2-} mobility and hence lower conductivity. At high temperatures (HT-region), charge carrier thermal vibrations can also briefly assist the hopping process by either shortening the hopping distances or extending the hopping conduction paths through the crystal lattice. It is reported that cubic stabilized bismuth oxides undergo an order-disorder transition, illustrated by a change in the conductivity and activation energy, at temperatures in the neighbourhood of 600 °C.¹⁵

The “knee” or slight bend (when there is no phase change) indicates that moving from ordered to disordered O^{2-} vacancies is accompanied by a decrease in E_a for O^{2-} conduction. This is somewhat obscured when there is a phase change taking place (as in the case of the 5Pb10YSB sample), but there is a definite decrease in slope (i.e. a decrease in E_a) when this transition occurs at higher temperatures. On cooling, the oxygen sublattice becomes more ordered again below the transition temperature because of the weak scattering of X-rays by oxygen ions.

A decrease in conductivity is caused by an increase in dopant concentration, and this could be partly due to stronger association of O^{2-} with the dopant ions (stronger bonds) reducing mobility. A decrease in polarizability also plays a role, as well as the ionic radius of the dopant ion. The single dopant system of $(Y_2O_3)-(Bi_2O_3)$ was studied by Takahashi et al.⁹ and reported that for cubic structure stabilization, the highest conductivity was obtained with the lowest dopant concentration. In principle, the ionic conductivity of most oxide ion conductors should increase as the concentration of oxygen vacancy increases. Many other factors also play important roles in the ionic conductivity, such as properties of crystallography and microstructure, in particular porosities and grain sizes.⁹

To calculate E_a in terms of eV from the slope of the $\log(\sigma_b)$ versus $(1/T)$ graph:¹⁶

$$E_a = \frac{-slope \times \ln 10 \times R}{\left(1.602177 \times 10^{-19} J/eV\right) N_A} \quad (4.7)$$

The values of the activation energy (E_a) obtained from the slopes in the Arrhenius plots in Fig 4.7, for each linear region as described, are listed in Table 4.4. The activation energies differed slightly in the LT and HT regions for the various concentrations of the doping material, PbO and Y_2O_3 . The difference in activation energies indicates that charge carriers have to overcome different energy barriers while conduction and relaxing. This variation in the activation energies also emphasizes that the relaxation process are of the non-Debye type. During both the heating and cooling cycles, the change in E_a when moving from the LT region to the IT region was far bigger for the 5Pb10YSB ceramic material as compared to other composition, indicating a big change in the mechanism of conduction which indicates the temperature range where the phase change is occurring and a move to a more conductive phase. Interestingly, there is a small step change in E_a for both the highly doped samples which is unexpected for a pure phased sample as indicated by the VT-Raman spectroscopy data for 1.5Pb25YSB (Fig 3.21). However, from the VT-PXRD data for this sample a step increase in the lattice parameter on heating (and the reverse on cooling) was also noted in the same temperature range (Fig 3.11). The crystal structure clearly had an impact on the ionic conductivity of the pure phased sample. The very low E_a values in the

HT region is due to a combination of factors, namely, the presence of the pure fcc phase, the disordered oxygen sublattice and the more sharply expanding unit cell (as indicated by the higher slope in Fig 4.7 in the HT range compared to the LT range).

Table 4.4 Derived electrical parameters for PbYSB compositions. 5Pb10YSB sample applies to the first cycle and the rest to the second cycle data.

Heating	E_a (eV)		
	LT	IT	HT
5Pb10YSB	1.21	1.52	1.07
3.75Pb25YSB	1.22	1.41	0.86
6Pb25YSB	1.30	1.42	0.69
Cooling			
5Pb10YSB	1.29	1.78	0.49
3.75Pb25YSB	1.19	1.28	0.58
6Pb25YSB	1.45	1.33	0.65

Theoretically, the total activation energy for ionic conductivity is expressed by the following formula:^{16,17}

$$E_a = E_m + E_d \quad (4.8)$$

where E_m is the migration activation energy for interstitial O^{2-} ions jumping to the appropriate O^{2-} vacancy points in the lattice and E_d is the additional energy needed to break the metal-oxygen ionic bonds in the lattice. The activation energy (E_a) for the interstitial oxide anions through the cubic Bi_2O_3 lattice depends on the conductive pathway through which O^{2-} ions migrate and the oxygen-binding energy; E_d is thus the amount of energy required to break a lattice cation-oxygen bond, as well as an energy term dependent on the mobility of oxide ions between interstitial filled and empty O^{2-} lattice points.¹⁷

The conductivities of 5Pb10YSB and 3.75Pb25YSB were further investigated by comparing to related materials, namely 10YSB and 27.5YSB, which were both prepared in our laboratory by a similar sol-gel synthesis route and the conductivities were measured in a similar way therefore making direct comparison feasible. For the YSB samples, only a single heating and cooling cycle

was measured, thus data using the same conditions for the PBYSB samples was used in the comparison. This was done to see if any light could be shed on whether the lone pair of electrons for Pb^{2+} plays a role in enhancing the mobility of the oxide ions through the lattice. We believe that all these conductivities are primarily ionic, while further investigation is really needed to confirm this.

Fig 4.8a shows a comparison of the cooling cycles for 5Pb10YSB and 10YSB (phase pure material). 5Pb10YSB is more highly doped than 10YSB but with same amount of Y content, therefore it is expected to be less conducting due to higher total dopant concentration. From Fig 4.8a, 5Pb10YSB is seen to be more conductive than 10YSB despite being highly doped, suggesting a possible indication of Pb^{2+} enhancing conductivity. However, more highly doped could also mean low amount of impurity phase at lower temperature and thus higher conductivity.

Fig 4.8b shows a comparison of the cooling cycles for 3.75Pb25YSB and 27.5YSB which have a very similar total dopant concentration and should both consist of pure δ -phase. 3.75Pb25YSB sample has a total dopant concentration slightly higher than 27.5YSB sample but it is more conductive. Again, this is not expected, and it highlights the possible indication of Pb^{2+} enhancing conductivity or a low amount of impurity phase at lower temperature and thus higher conductivity. Due to the complex interplay of various factors affecting the conductivities in these materials, it is difficult to come to a conclusion regarding the role of the lone pairs of Pb^{2+} .

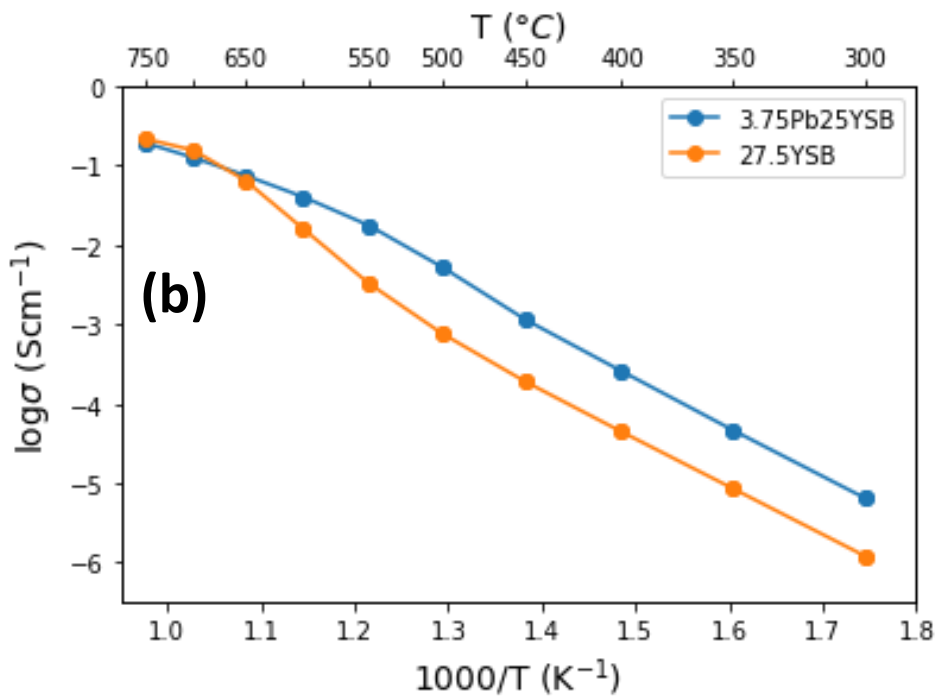
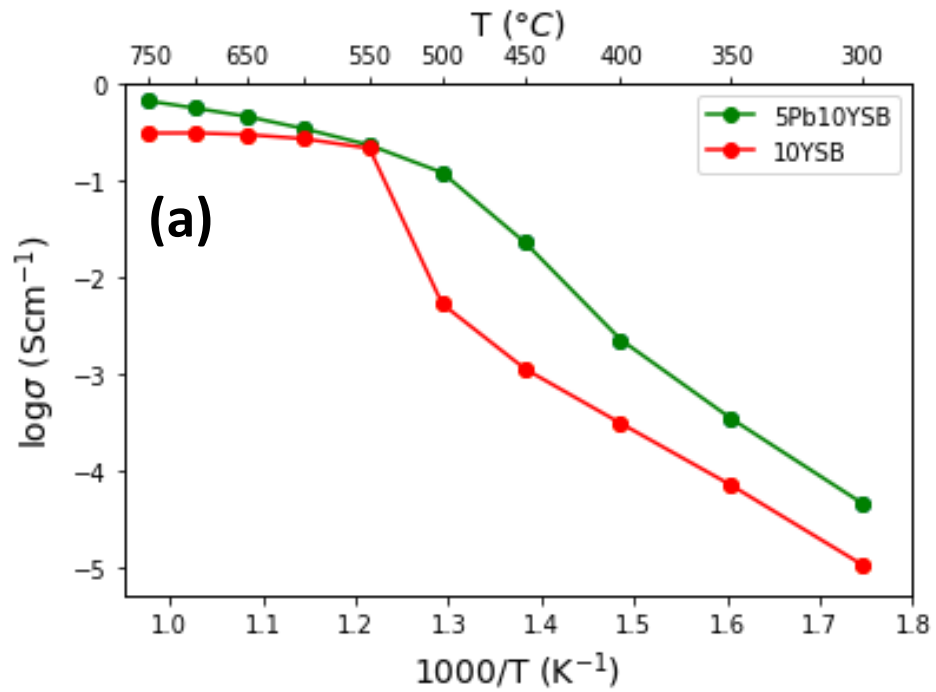


Fig. 4.8 Arrhenius plot of conductivities both cooling cycles for 5Pb10YSB, 10YSB (a) and 3.75Pb10YSB, 27.5YSB (b).

As seen in the high conductivities observed at 700 and 750°C for 5Pb10YSB (and even at lower), this provides a positive aspect when considering the solid electrolyte character for solid oxide fuel cells (SOFCs). Typically, the solid electrolyte's high level of ionic conductivity will lead to an improvement in the SOFC system's electrochemical energy production efficiency. The problem with the 5Pb10YSB sample is that it undergoes a phase change (tetragonal to cubic phase) which is accompanied by a large expansion in the lattice which is not ideal for an electrolyte. The conductivity at lower temperatures, before the phase change occurs (~450 - 500°C) are still relatively high meaning it could possibly be used at lower temperatures. Of course, other properties such as ageing at the temperatures also have to be looked at.

4.5. References

1. Aziz, S.B., Al-Zangana, S., Brza, M.A., Saeed, S.R., Abdulwahid, R.T. and Kadir, M.F.Z., 2019. Study of dielectric properties and ion transport parameters in chitosan-barium nitrate based solid polymer electrolytes. *International Journal of Electrochemical Sciences*, 14, pp.11580-11595.
2. Wilson, J., Schwartz, D. and Adler, S., 2006. Nonlinear electrochemical impedance spectroscopy for solid oxide fuel cell cathode materials. *Electrochimica Acta*, 51(8-9), pp.1389-1402.
3. Bard, A.J. and Faulkner, L.R., 2001. Fundamentals and applications. *Electrochemical Methods*, 2(482), pp.580-632.
4. Gerischer, H., 1951. Wechselstrompolarisation von Elektroden mit einem potentialbestimmenden Schritt beim Gleichgewichtspotential I. *Zeitschrift für Physikalische Chemie*, 198(1), pp.286-313.
5. Michel, R. and Montella, C., 2015. Diffusion–convection impedance using an efficient analytical approximation of the mass transfer function for a rotating disk. *Journal of Electroanalytical Chemistry*, 736, pp.139-146.
6. Kilner, J.A., 2008. Feel the strain. *Nature Materials*, 7(11), pp.838-839.
7. Ormerod, R.M., 2003. Solid oxide fuel cells. *Chemical Society Reviews*, 32(1), pp.17-28.
8. Tran, T.B. and Navrotsky, A., 2012. Energetics of dysprosia-stabilized bismuth oxide electrolytes. *Chemistry of Materials*, 24(21), pp.4185-4191.
9. Takahashi, T., Iwahara, H. and Arao, T., 1975. High oxide ion conduction in sintered oxides of the system $\text{Bi}_2\text{O}_3\text{-Y}_2\text{O}_3$. *Journal of Applied Electrochemistry*, 5(3), pp.187-195.
10. Ekhekar, S. and Bichile, G.K., 2004. Synthesis and structural characterization of $(\text{Bi}_2\text{O}_3)_{1-x}(\text{Y}_2\text{O}_3)_x$ and $(\text{Bi}_2\text{O}_3)_{1-x}(\text{Gd}_2\text{O}_3)_x$ solid solutions. *Bulletin of Materials Science*, 27(1), pp.19-22.
11. Gil, V., Tartaj, J., Moure, C. and Durán, P., 2006. Sintering, microstructural development, and electrical properties of gadolinia-doped ceria electrolyte with bismuth oxide as a sintering aid. *Journal of the European Ceramic Society*, 26(15), pp.3161-3171.
12. Steil, M.C., Fouletier, J., Kleitz, M. and Labrune, P., 1999. BICOVOX: Sintering and grain size dependence of the electrical properties. *Journal of the European Ceramic Society*, 19(6-7), pp.815-818.
13. Torun, H.O., Cakar, S., Ersoy, E. and Turkoglu, O., 2015. The bulk electrical conductivity properties of $\delta\text{-Bi}_2\text{O}_3$ solid electrolyte system doped with Yb_2O_3 . *Journal of Thermal Analysis and Calorimetry*, 122(2), pp.525-536.
14. Kilner, J.A., 2000. Fast oxygen transport in acceptor doped oxides. *Solid State Ionics*, 129(1-4), pp.13-23.
15. Wachsmann, E., Boyapati, S., Kaufman, M. and Jiang, N., 2004. Modeling of Ordered Structures of Phase-Stabilized Cubic Bismuth Oxides. *Journal of the American Ceramic Society*, 83(8), pp.1964-1968.
16. Whittingham, M., 1989. Basic solid state chemistry Anthony R. West, John Wiley & Sons, New York (1988), 415 pages £13.95 (\$32.95). *Solid State Ionics*, 34(3), p.213.
17. Walker, C., 1967. Solid State Physics over 13 Years: Introduction to Solid State Physics. Charles Kittel. Wiley, New York, ed. 3, 1966. 662 pp., illus. \$12.50. *Science*, 155(3765), pp.991-991.

In this study, double-doped (with Pb^{2+} and Y^{3+}) stabilized bismuth oxides were synthesized and investigated. High total dopant concentrations (ranging from 26.5-40 mol%) samples, according to XRD analysis stabilised δ -phase. But when further annealed at 800°C for 20 hours phase degradation took place. This was confirmed by doing further VT studies (XRD and Raman spectroscopy) on the 1.5Pb25YSB sample which is the lowest dopant concentration in this range. For the low total dopant concentration (ranging from 10-20 mol%), samples with 10-12 mol% total did not stabilise the δ -phase, irrespective of ratio of Pb:Y used. It appeared as if samples with Pb^{2+} did stabilize δ -phase only if the dopant concentration of Pb^{2+} was way less than that of Y^{3+} . Further VT XRD studies of 5Pb10YSB pointed to possible phase impurity, confirmed by VT-Raman spectroscopy. The phases found were the β and δ -phases. Initial PDF analysis of the same samples showed only the δ -phase, but this data may need more careful scrutinization.

The material with a high total dopant concentration (3.75Pb25YSB) is expected to result with the “knee” or bend in the Arrhenius curve at high temperature due to a change from ordered to disordered O-sublattice. But a slight step was observed which indicates a possible phase impurity which ties in with the change in the lattice parameters observed from VT-XRD. The material with a low total dopant concentration (5Pb10YSB) showed a clear phase change indicated by a change in slope in the Arrhenius plot (a “knee” or bend in the curve at around $550\text{-}600^\circ\text{C}$) as expected. XRD diffractograms did not reveal any changes in the oxygen sublattice, need to use neutron diffraction to investigate this more carefully. The changes in the oxygen sublattice were not picked up by XRD – need to use nWhat was evident from this work was the wealth of information revealed by the variable temperature studies of the materials, be it PXRD, DTA/TGA, RS or EIS, and further with the combination of these techniques, each different in the physics they employ, complementing each other. It also highlighted that simply confirming phases by peak positions in XRD is far from adequate. The phase evolution, as initially hinted by VT-PXRD, was then only made it obvious with the DTA

and VT-EIS data, which resulted in more rigorous analysis of the lower temperature data using Rietveld refinement and with phase confirmation coming from RS. This just shows some of the issues with some techniques and why it is essential to adopt a multi-technique approach.